NORTHWESTERN UNIVERSITY

Impact of Solar Cell Processing Conditions on Active Layer Morphology and Charge Generation Dynamics in Organic Solar Cells

A DISSERTATION

SUBMITTED TO THE GRADUATE SCHOOL
IN PARTIAL FULFILLMENT OF THE REQUIREMENTS

for the degree

DOCTOR OF PHILOSOPHY

Field of Chemistry

By
Sylvia Jen-Ming Lou

EVANSTON, ILLINOIS

November 2018

Abstract

Increasing industrialization and the resulting negative environmental impacts highlight the need to develop alternative renewable energy sources. The Sun is a massive source and organic solar cells are a growing field of study. As new materials are synthesized, the efficiencies of organic solar cells continue to grow, but without an understanding of the fundamental processes of current generation, improvements in solar cells are limited to high throughput screening of new materials and *ad hoc* use of a variety of processing conditions. In this thesis, we demonstrate the effects of processing conditions and molecular structure on the photoactive layer morphology and charge carrier generation in organic solar cells based on small molecule and polymeric materials.

Chapters 2 and 3 address the effects of solvent additives on polymer and small molecule aggregation in solution and the effect on thin film morphology. We demonstrate in two active layer solutions, (1) PTB7 and $PC_{61}BM$ and (2) PBTIBDT and $PC_{71}BM$, that the additive, 1,8 diiodooctane, completely dissolves the fullerene component of the active layer solution allowing for interpenetration into the polymer matrix and a large mixed fullerene-polymer domain in the thin film. This results in improved charge generation, but also increased bimolecular recombination demonstrating that the active layer morphology must be delicately balanced between pure domains and mixed domains to achieve the highest solar cell efficiency.

The focus of Chapter 4 is the structure of small molecule donors in organic solar cells. In solar cells based on small molecule donors, the crystal structure and the resulting charge transport abilities of the crystal have a large impact on the final solar cell efficiency. In this study, we present a series of small molecule donors with an acenedithiophene core unit of varying lengths and find that longer and more planar molecules create more tightly packed crystals that create small, but highly crystalline domains in thin film. We further demonstrate that the longer molecules show increased mobility in both neat thin films and in films blended with the fullerene $PC_{61}BM$.

Acknowledgements

This thesis would not have been possible without the continued support of friends, family, collaborators and mentors.

Thank you to my mentors, Professors Tobin Marks and Lin Chen, who provided scientific expertise, encouragement, and resources to let me independently guide myself through this process. Their flexibility, patience, and persistent belief that I would complete the doctorate program has made it a reality.

Many thanks to numerous committee members throughout the years including Professor Bob Chang, Professor Mike Wasielewski, Professor Emily Weiss, and Dr. Dick Co for their helpful feedback and interest.

I am grateful to the ANSER center for funding my research and particularly, to Subtask 2 members for providing endless ideas and inspiration.

Without any samples I would not have been able to do any experiments, so I am indebted to many synthetic chemists including Xugang Guo, Carson Bruns, Matthew Leonardi, Amod Timalsina, and all of Luping Yu's group.

I am grateful to Nanjia Zhou and Kyle Luck who overcame their instincts to make the highest efficiency solar cells and helped me fabricate solar cells that we knew would have low performance time and again.

To Joe Strzalka and the Beamline 5 and 8ID scientists, for whose generosity and x-ray scattering knowledge I am incredibly grateful.

Without the support of the Chen and Marks groups, I would not have considered my work with such scrutiny. Many thanks to Jodi Szarko who started me on the x-ray scattering path, to Brian Rolczynski and Mike Mara, who always had the time to teach me something new, to Dugan Hayes and Kelly Fransted, who let a laser novice mess with their system and helped put it back together again, and to Eric Manley and Nick Jackson, who always provided a fresh perspective.

Thanks to Brett Savoie for his amazing ability to grasp and explain a vast amount of literature and for our scientific and philosophical discussions.

Thanks to my parents who always encouraged me to finish what I start, to KC who knew when I needed a good meal, and to my family who always asked about my work, always listened, and never pried.

I am eternally grateful to my husband, Stephen Loser, who taught me how to make my first solar cell and how to cook. I would not have been able to take the first or last step of this journey without his help.

And finally, I would like to thank my children, who showed me the value of time and the importance of claiming my own identity as a scientist.

Table of Contents

Abstract **2**

Acknowledgements **4**

Table of Figures **11**

Table of Tables **18**

Table of Schemes **21**

Chapter 1 . Introduction to Organic Solar Cells and Characterization Techniques **22**

1.1 Solar energy **22**

1.2 History of solar cells **22**

1.2.1 Bilayer solar cells 23

1.2.2 Bulk heterojunction solar cells 26

1.3 Solar cell performance metrics **34**

1.4 Characterizing morphology in organic solar cells **37**

1.4.1 Grazing incidence x-ray scattering 38

1.4.2 Scanning probe microscopy 45

1.5 Characterization of photophysical processes **45**

1.6 Solar cell processing conditions **48**

Chapter 2 . Effects of Additives on the Morphology of Solution Phase Aggregates Formed by Active Layer Components of High-Efficiency Organic Solar Cells **50**

2.1 Introduction **50**

2.2 Experimental 53

2.2.1 Solution sample preparation 53

2.2.2 Small angle x-ray scattering 53

2.2.3 X-ray scattering fitting procedures 54

2.3 Results and Discussion 61

2.4 Conclusion 68

Chapter 3 . Effects of 1,8-Diiodooctane on Domain Nanostructure and Charge Separation Dynamics in $PC_{71}BM$-Based Bulk Heterojunction Solar Cells 71

3.1 Introduction 71

3.2 Methods 76

3.2.1 Materials synthesis 76

3.2.2 Device characterization 77

3.2.3 Solution structural characterization 77

3.2.4 Film morphology measurements 78

3.2.5 Transient optical absorption spectroscopy 79

3.3 Results 80

3.3.1 Solar cell performance 81

3.3.2 Aggregate dimensions in solution 84

3.3.3 Crystal structure and domain size in thin films 88

3.3.4 Exciton and charge generation/transport dynamics by optical transient absorption spectroscopy 97

3.4 Discussion 109

3.4.1 Influence of DIO on active layer morphology 109

3.4.2 Morphology-dependent dynamics of intermediate species 112

3.5 Conclusion 116

Chapter 4 . Systematic Evaluation of Structure-Property Relationships in Heteroacene-Diketopyrrolopyrrole Molecular Donors for Organic Solar Cells 118

4.1 Introduction 118

4.2 Methods 124

4.2.1 Synthesis 124

4.2.2 Optical absorption spectroscopy 125

4.2.3 Cyclic voltammetry (CV) 126

4.2.4 Differential scanning calorimetry (DSC) 126

4.2.5 Single crystal growth and characterization 126

4.2.6 Film grazing incidence X-ray scattering 127

4.2.7 Transmission electron microscopy (TEM) and atomic force microscopy (AFM) 128

4.2.8 Electronic structure calculations 128

4.2.9 Organic field effect transistor fabrication 129

4.2.10 Space charge limited current (SCLC) single carrier diode fabrication 130

4.2.11 Organic photovoltaic (OPV) cell fabrication and characterization 131

4.3 Results 132

4.3.1 Solution and film optical absorption properties 132

4.3.2 Electronic properties from cyclic voltammetry 135

4.3.3 Differential scanning calorimetry 139

4.3.4 Crystal structures 141

4.3.5 Active layer domain sizes and molecular orientations 146

4.3.6 Internal reorganization energies and co-facial electronic coupling 156

4.3.7 OFET and SCLC transport properties 161

4.3.8 OPV response 162

4.4 Discussion 166

4.4.1 Single crystal and neat film crystal structures 166

4.4.2 Blend film morphology 167

4.4.3 *J-V* OPV characteristics 168

4.5 Conclusion 171

Appendix A. Supplemental Materials for Effects of 1,8 Diiodooctane on Domain Nanostructure and Charge Separation Dynamics in $PC_{71}BM$-Based Bulk Heterojunction Solar Cells 173

A.1. Solar cell external quantum efficiency data 173

A.2. Small angle x-ray scattering component fits for PBTIBDT+PCBM solutions with 0-5 vol% DIO 174

A.3. GIWAXS data analysis procedures and 2D images 176

A.4. Optical transient absorption within 3 ns delay time window, and fitting parameters for exciton absorption and ground state bleach 179

A.5. Nanosecond transient absorption spectroscopy 183

Appendix B. Supplemental Materials for Systematic Evaluation of Structure-Property Relationships in Heteroacene-Diketopyrrolopyrrole Molecular Donors for Organic Solar Cells 184

B.1. Single crystal x-ray diffraction 184

B.2. Comparison of single crystal structure and film crystal structure 186

B.3. OFET and SCLC mobility measurements..... 190

References..... 193

Table of Figures

Figure 1.1. Organic solar cell architectures: A) single material solar cell, B) bilayer solar cell, and C) bulk heterojunction solar cell 24

Figure 1.2. Mechanism of current generation in organic solar cells depicted through schematics of the active layer morphology and energetics. p-type domains are depicted in red while n-type, or acceptor, domains are depicted in blue. The anode is shown in white while the cathode is gray. Dashed lines indicate that the electron and hole are still within the Coulombic radius of each other. 25

Figure 1.3. Commonly used building blocks for push-pull alternating copolymers and small molecules 28

Figure 1.4. Selected high efficiency push-pull polymers 29

Figure 1.5. p-type donor small molecules with A – D – A building blocks 31

Figure 1.6. Commonly used n-type acceptor small molecules 33

Figure 1.7. Illuminated *J-V* curve with figures of merit 35

Figure 1.8. Schematic of grazing incidence x-ray scattering experimental setup 39

Figure 1.9. Grazing incidence x-ray scattering of poly-3-hexylthiophene (P3HT) including linecuts along the q_z and q_{xy} axis and corresponding lamellar and π-stacking crystal planes in P3HT crystal schematic 41

Figure 1.10. Grazing incidence small angle x-ray scattering trace showing the Guinier region which indicates the size of the domain and the Porod region, the slope of which indicates the surface structure. 44

Figure 1.11. Schematic of transient absorption experimental setup where τ is a variable time delay 47

Figure 2.1. Structures of active layer components 52

Figure 2.2. a) Scattering signal from CB solvent without DIO. b) The accompanying figure shows the difference in the subtracted signals using a background with or without DIO 55

Figure 2.3. Level 1 distribution of peak in high *Q* regime (*Q* ~0.4 $Å^{-1}$): a) fit and residual, and b) log normal distribution 57

Figure 2.4. Level 2 distribution of peak in middle *Q* regime (*Q* ~0.15 $Å^{-1}$): a) fit and residual, and b) log normal distribution 58

Figure 2.5 Level 3 distribution of peak in the low *Q* regime (*Q* <0.1 $Å^{-1}$): a) fit and residual, and b) log normal distribution (pink) 59

Figure 2.6. a) Total fit of PTB7 curve using all three distributions. b) Total distribution of scatterer diameter sizes. Distributions are color coded so that distribution 1 (green) corresponds to the Level 1 fit (high *Q*), distribution 2 (blue) corresponds to the Level 2 fit (mid *Q*), and distribution 3 (pink) corresponds to the Level 3 fit (low *Q*). The total distribution is shown in red 60

Figure 2.7. Experimental scattering profiles of active layer solutions (solid lines) and fits (dotted lines), comparing aggregation in CB and CB:DIO solutions of: (a) PTB7 (offset) and (b) $PC_{71}BM$, and two-component fits of PTB7:$PC_{71}BM$ in: (c) CB and (d) CB:DIO. 62

Figure 2.8. Fits of $PC_{71}BM$ traces obtained by subtracting PTB7 component fit from the blend traces. 65

Figure 2.9. Standard Modeling I fit for PTB7:$PC_{71}BM$ blend solutions assuming three Gaussian distributions of aggregates. PTB7:$PC_{71}BM$/CB:DIO is offset by a factor of 0.5. 67

Figure 2.10. Schematic of PTB7 and $PC_{71}BM$ aggregation in: (a) CB and (b) CB:DIO and the resulting film morphology 69

Figure 3.1. Chemical structures of the electron donor polymers A) PBTIBDT and B) PTB7..... 75

Figure 3.2. *J-V* response of PBTIBDT: $PC_{71}BM$ solar cells with varying concentrations of DIO in the *o*-dichlorobenzene film casting solution..... 82

Figure 3.3. Solution phase small angle X-ray scattering traces of, (A) PBTIBDT and (B) $PC_{71}BM$ in *o*-dichlorobenzene solution with 0.0 – 5.0% DIO used to estimate aggregate size. Straight gray dotted lines provide visual guidance to peak locations and traces are offset for clarity..... 86

Figure 3.4. TEM images of PBTIBDT: $PC_{71}BM$ blend films cast from *o*-dichlorobenzene with 0.0-5.0 vol% DIO. The darker regions have higher $PC_{71}BM$ concentrations..... 89

Figure 3.5. Morphology and crystal structures of neat and blend PBTIBDT films cast from *o*-dichlorobenzene with 0.0 and 3.0 vol% DIO as described by GIWAXS line-cuts in the, (A) out-of-plane orientation and (B) in-plane orientation describing the crystal structure and crystalline correlation lengths..... 91

Figure 3.6. GISAXS linecuts of PBTIBDT:PCBM blend films with 0-5 vol% DIO describing the domain sizes out of plane..... 96

Figure 3.7. Optical absorption spectra of neat PBTIBDT films with no DIO and 1-5 vol% DIO 98

Figure 3.8. Spectroelectrochemisty spectra of PBTIBDT solutions in *o*-dichlorobenzene and neat film showing cation signals at 750-800 nm with a broad feature extending from 1000 nm to longer wavelengths 99

Figure 3.9. Transient absorption spectra of (A) PBTIBDT solution in *o*-dichlorobenzene, PBTIBDT neat film with 0.0 vol% DIO, and PBTIBDT: $PC_{71}BM$ film with 3.0 vol% DIO at 1 ps after excitation, showing the underlying exciton and cation peaks at $\lambda = 1000-1040$ nm and 1180 nm, respectively, (B) initial cation population and decay normalized to the ground state bleach signal amplitudes, (C) decay of the cation peak at 1180 nm with different DIO concentrations 101

Figure 3.10. Long-lived cation populations in PBTIBDT and PBTIBDT: $PC_{71}BM$ thin films as measured by ns TA 108

Figure 3.11. Schematic of the packing morphology of the *interfacial region* of PBTIBDT: $PC_{71}BM$ blend films processed with, A) no DIO, B) 3.0 vol% DIO, and C) 5.0 vol% DIO. PBTIBDT polymer chains are shown in blue and $PC_{71}BM$ molecules are shown in orange. As vol% DIO is increased, PBTIBDT domains become more loosely packed and $PC_{71}BM$ aggregate size decreases, allowing increased $PC_{71}BM$ intermixing. 111

Figure 3.12. Increase in J_{sc} and *FF* as $PC_{71}BM$ solution aggregate size decreases with increasing vol% DIO 115

Figure 4.1. Optical absorption spectra of (A) small-molecule solutions in $CHCl_3$ showing calculated molar extinction coefficients and (B) neat, annealed small-molecule thin films cast from $CHCl_3$ showing absorption coefficients 133

Figure 4.2. Cyclic voltammetry plots of the indicated small molecules as CH_2Cl_2 solutions 137

Figure 4.3. Differential scanning calorimetry scans showing the endothermic melting temperature (negative peak) and the exothermic crystallization temperature (positive peak) of the indicated small molecules 140

Figure 4.4. Relevant solid state geometries and distances, exemplified by the crystal structure of NDT. Lateral and longitudinal offsets describe the relative locations of neighboring π–π stacked molecules where lateral offset is along the *y*-axis and the longitudinal offset is along the *x*-axis. The π–π stacking *d*-spacing is the shortest distance perpendicular to the backbones parallel to the *z*-axis. The symbol φ denotes torsional angle about the indicated bond 142

Figure 4.5. Single crystal unit cell packing diagrams (left) and π-stacking viewed along the stacking direction of the molecules (right) of (A) aBDT, (B) BDT, (C) BDF, and (D) NDT 144

Figure 4.6. Grazing incidence X-ray scattering detector images of annealed thin films of neat small-molecule (top) and small-molecule:PCBM (1.5:1.0 w/w, bottom) materials; (A) aBDT, (B) BDT, (C) BDF, (D) NDT, (E) zNDT. Insets show lamellar stacking peak in the small *q* regime (q = 0-0.5 Å^{-1}) 147

Figure 4.7. Comparison of powder diffraction calculated from the single crystal structure and data showing in-plane and out-of-plane structure from GIWAXS 148

Figure 4.8. Transmission electron and atomic force micrographs (insets) of blend annealed SM:PCBM films, (A) aBDT, (B) BDT, (C) BDF, (D) NDT, (E) zNDT, showing varied domain sizes and roughnesses 151

Figure 4.9. (A) Schematic of small-molecule domains in which the molecules are aligned edge-on at 0° tilt of the domain and face-on at 90° tilt of the domain. (B) Sample fits for circular linecuts of the π-π stacking peak in neat films to determine degree of preferential orientation. Angular dependence of the π–π stacking peak in (C) neat small-molecule films and (D) SM:PCBM blend films. The decrease in intensity of the π–π stacking feature vs the baseline is indicated by a dotted line and indicates the degree of orientational preference in each small-molecule system. The increase in intensity in BDT at 30–60° is due to an overlapping reflection. 155

Figure 4.10. Frontier molecular orbitals calculated by TD-DFT. 160

Figure 4.11. (A) *J-V* and (B) external quantum efficiency (EQE) response of optimized small-molecule:PCBM OPV devices..... 165

Figure A.1. External quantum efficiencies of PBTIBDT:PCBM solar cells with 0-5 vol% DIO added to the active layer solution..... 173

Figure A.2. Representative fits of PBTIBDT+PCBM solution data with 0 vol% DIO..... 174

Figure A.3 2D GIWAXS images of neat films of a) PBTIBDT 0% DIO and b) PCBM and blend PBTIBDT:PCBM films with: c) 0 vol % DIO, d) 3 vol% DIO, e) 5 vol% DIO 176

Figure A.4. GIWAXS linecuts along the horizontal and vertical axes of the 2D images showing the crystal structure of A) neat PBTIBDT films with 0-5 vol % DIO in-plane and B) neat PBTIBDT films with 0-5 vol% DIO out of plane and C) PBTIBDT:PCBM films with 0-5 vol % DIO in-plane and PBTIBDT:PCBM films with 0-5vol % DIO out of plane. 177

Figure A.5. Time delays of A) neat PBTIBDT film with 0 vol% DIO and B) PBTIBDT:PCBM blend film with 0 vol% DIO and C) 5 vol% DIO and D) PBTIBDT:PCBM blend film with 3 vol% DIO illustrating the entire visible and near IR spectra. 179

Figure A.6. Decay of cation species at 1070 nm in PBTIBDT:PCBM films as a function of vol % DIO normalized at the highest intensity 183

Figure B.1. Typical transfer plots of neat films of (A) BDTTDPP, (B) $BDT(TDPP)_2$, (C) $BDF(TDPP)_2$, (D) $NDT(TDPP)_2$, and (E) $zNDT(TDPP)_2$ 190

Figure B.2. Typical output plots of neat films of (A) $BDT(TDPP)_2$, (B) $BDF(TDPP)_2$, (C) $NDT(TDPP)_2$, and (D) $zNDT(TDPP)_2$ 191

Figure B.3. J-E response data and fits describing the SCLC mobilities in small molecule donor neat films. 192

Table of Tables

Table 3.1. Performance metrics of PBTIBDT:$PC_{71}BM$ solar cells fabricated with varying concentrations of DIO in the *o*-dichlorobenzene film casting solution 83

Table 3.2. Solution phase radii of gyration (R_g) of neat PBTIBDT and $PC_{71}BM$ aggregates in *o*-dichlorobenzene with 0.0 – 5.0 % DIO obtained from SAXS measurements. Quantities in parentheses denote estimated uncertainties form the Unified fitting procedure. 87

Table 3.3. Thin film domain sizes calculated by a Guinier fit to the GISAXS data, and crystalline correlation lengths calculated by Scherrer analysis of GIWAXS data. Errors in fit given in parentheses. 93

Table 3.4. Fitting parameters of PBTIBDT: $PC_{71}BM$ cation signal at 1180 nm showing decay rates (τ) and relative fractions (p^*) from the population remaining after 1 ps. The relative fractions (p) of the total and τ_1 are presented in the SI. τ_2 is only associated with the EX feature. 104

Table 3.5. Fitting parameters for cation decay at 1070 nm for long time delays (5 ns – 20 μs).[a]Numbers in parentheses are estimated fitting uncertainties. 107

Table 4.1. Optical properties and energetics of pristine small-molecule compounds in solution and as thin films 134

Table 4.2. Calculated HOMO energies 138

Table 4.3. Single crystal *d*-spacings, torsional angles, and longitudinal offsets by X-ray diffraction 145

Table 4.4. GIXS thin film molecular *d*-spacing data and crystalline domain sizes calculated by Scherrer analysis 150

Table 4.5. Computed reorganization energies, co-facial coupling, and experimental charge transport parameters for the indicated molecular donors..... 158

Table 4.6. Solar Cell *J-V* device metrics..... 163

Table A.1. Table of small angle x-ray scattering component fit percentages..... 175

Table A.2. GIWAXS d-spacings of PBTIBDT and PCBM domains in neat and blend thin films as a function of vol% DIO. 178

Table A.3. Exciton dynamics of PBTIBDT:PCBM blend films 180

Table A.4. Ground state bleach dynamics of PBTIBDT:PCBM blend films..... 181

Table A.5. Dynamics of neat PBTIBDT films 182

Table B.1. Unit cell parameters and structure solution details 185

Table B.2. Comparison of peaks from calculated powder diffraction and fitting of GIWAXS scattering traces for BDTTDPP. [a]Denotes peaks used to measure the lamellar *d*-spacing in thin film and [b]denotes peaks used to measure the π-π *d*-spacing in thin film. Peaks along the q_z axis are noted in bold. 186

Table B.3. Comparison of peaks from calculated powder diffraction and fitting of GIWAXS scattering traces for BDT(TDPP)$_2$. [a]Denotes peaks used to measure the lamellar *d*-spacing in thin film and [b]denotes peaks used to measure the π-π *d*-spacing in thin film. Peaks along the q_z axis are noted in bold. 187

Table B.4. Comparison of peaks from calculated powder diffraction and fitting of GIWAXS scattering traces for BDF(TDPP)$_2$. [a]Denotes peaks used to measure the lamellar *d*-spacing

in thin film and [b]denotes peaks used to measure the π-π *d*-spacing in thin film. Peaks along the q_z axis are noted in bold. 188

Table B.5. Comparison of peaks from calculated powder diffraction and fitting of GIWAXS scattering traces for NDT(TDPP)$_2$. [a]Denotes peaks used to measure the lamellar *d*-spacing in thin film and [b]denotes peaks used to measure the π-π *d*-spacing in thin film. Peaks along the q_z axis are noted in bold. 189

Table of Schemes

Scheme 4.1. Synthetic scheme and molecular structures of the series of heterocyclic acenes (in color) flanked by thiophene-capped DPP units where R = 2-ethylhexyl 122

Chapter 1. Introduction to Organic Solar Cells and Characterization Techniques

1.1 Solar energy

Within the past forty years, the average temperature of the Earth has increased 0.9°C.[1, 2] Recent studies link this temperature shift to rising ocean levels,[3, 4] increased atmospheric disturbances and extreme weather events.[5, 6] While the extent of human impact on the climate is under continued debate, our energy production has no doubt contributed in part to these drastic climatic shifts.[7] Furthermore, as the world becomes increasingly industrialized, more countries will be contributing to the release of greenhouse gases, particularly CO_2, into the atmosphere, since 60% of the greenhouse gases globally are released through burning of fossil fuels for transportation, electricity production, and industry.[8, 9] Therefore, it is necessary to develop alternative energy sources to reduce to reduce the human impact on the environment.

1.2 History of solar cells

Solar energy offers a promising alternative since the Sun delivers an average power density of 188 W/m^2 on Earth[10, 11] which is 100 times greater than the predicted annual global energy consumption of 43 TW in 2100.[10] While solar energy may be utilized in a variety of devices, the most common is the solar cell. Currently, commercially available solar cells are composed of polycrystalline silicon which has an efficiency of 12-13%.[11] However, silicon solar

cells are also heavy, difficult to transport and install, and require expensive cleanroom manufacturing facilities.[12] Other materials, such as cadmium telluride and copper indium gallium selenide (CIGS),[13] have been utilized to create highly efficient solar cells, but are prohibitively expensive to manufacture for commercial use and insufficient for large scale energy production due to the scarcity of the raw materials.[14]

1.2.1 Bilayer solar cells

In 1986, C. W. Tang demonstrated the first organic photovoltaic system with appreciable efficiency approaching 1%.[15] While previous OPVs consisted of a single organic material sandwiched between two electrodes of different work function (Figure 1.1A),[16] Tang's system was unique because he create a bilayer of two photoactive materials which create a *p*-*n* junction to facilitate charge generation (Figure 1.1B). The fundamental processes involved in current production in the *p*-*n* bilayer solar cell are detailed in Figure 1.2. When sunlight is incident on the solar cell, the active layer *p*-type material (or electron donor) absorbs a photon creating a Coulombically bound hole-electron pair, an exciton. The exciton diffuses to the *p*-*n* interface where due to energetic differences between the lowest unoccupied molecular orbitals (LUMOs), the electron is transferred from the donor to the *n*-type electron acceptor creating a charge transfer state. As the charges separate further, the charge transfer state becomes a charge separated state in which the hole is localized on the donor and the electron is on the acceptor and they are no longer Coulombically bound. The free charges then migrate likely via a hopping or tunneling mechanism to the appropriate electrodes where they are collected.[17, 18] The detailed mechanism of this process is highly dependent on the materials and solar cell architecture and will be discussed in further detail below.

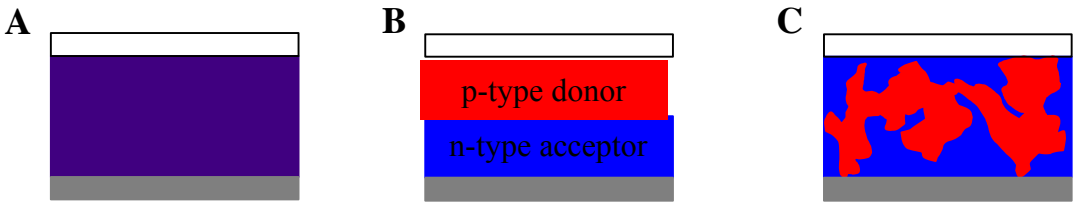

Figure 0.1. Organic solar cell architectures: A) single material solar cell, B) bilayer solar cell, and C) bulk heterojunction solar cell

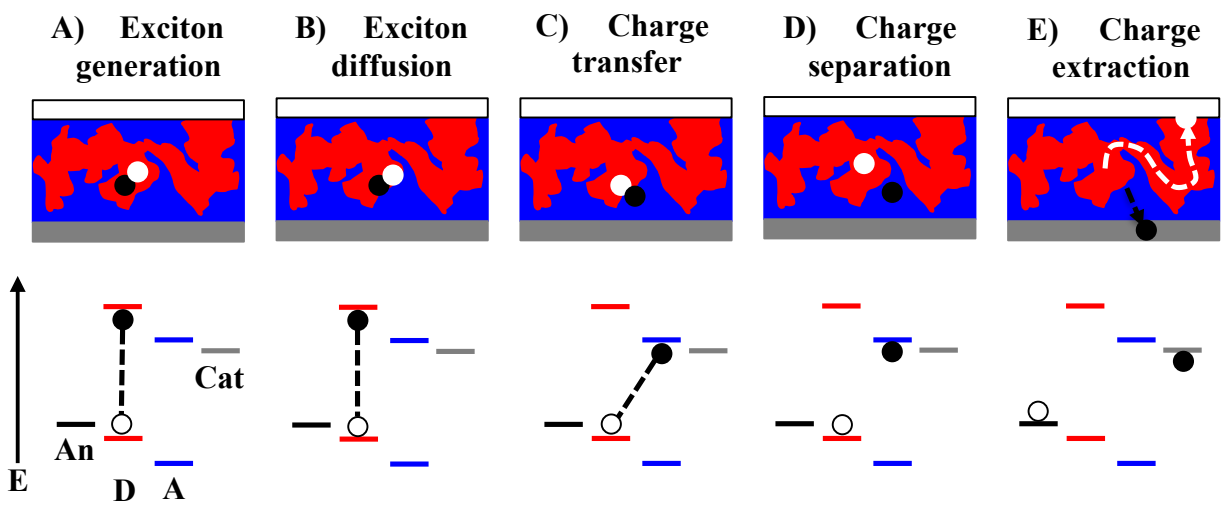

Figure 0.2. Mechanism of current generation in organic solar cells depicted through schematics of the active layer morphology and energetics. *p*-type (donor) domains are depicted in red while *n*-type (acceptor) domains are depicted in blue. The anode is shown in white while the cathode is gray. Dashed lines indicate that the electron and hole are still within the Coulombic radius of each other.

1.2.2 Bulk heterojunction solar cells

While Tang's initial organic solar cell exhibited efficiency of <1%, over the next thirty years, organic solar cell efficiencies have increased up to 15% on a laboratory scale[13, 19] and are approaching 10% on an industrial scale.[13, 20] The highest efficiency solar cells differ from Tang's in three aspects: 1) new *p*-type materials have been developed to increase absorption of the solar spectrum and promote charge separation, 2) new *n*-type materials have been utilized, most notably fullerene-based derivatives, and 3) the architecture of the solar cell has been improved to increase light absorption and free charge generation. The Tang solar cell was a bilayer solar cell with only one donor-acceptor interface where charge separation could occur. Since excitons in organic materials have lifetimes of <1 ns,[21] only excitons generated within 10 nm of the interface can separate into free charges before decaying,[22] resulting in geminate recombination of excitons in the bilayer architecture.[23] Therefore, current solar cells utilize a bulk-heterojunction (BHJ) active layer morphology (Figure 1.1C) in which the donor and acceptor are intimately mixed to create multiple interfaces for charge separation.[24, 25] However, the active layer must also consist of a bicontinuous network of donor and acceptor materials to facilitate charge transport to the electrodes. This balance between charge separation and transport necessitates a generalized ideal morphology of 10 nm domains.[26] This BHJ morphology can be modulated by thermal annealing,[27-31] solvent annealing,[32-34] use of solvent additives,[35-38] and ratio of the donor to acceptor,[39-42] but the effect of these processing conditions on morphology and solar cell performance is highly materials dependent.

Current state-of-the-art *p*-type electron donor materials are conjugated polymers or small molecules. The first generation of polymers were homopolymers, such as P3HT, but the current

generation of alternating copolymers exhibit higher efficiencies.[43] These alternating copolymers utilize the inherent dipole in a polymer chain composed of at least two types of monomers with differing electron withdrawing abilities.[44, 45] These so-called push-pull materials are composed of an electron withdrawing moiety, such as benzodithiophene and other thiophene derivatives, and an electron donating moiety, such as diketopyrrolopyrrole and benzothiadiazole (Figure 1.3).[46, 47] Using two different moieties and modulating the side chain oxidation and fluoridation, the band gap and lowest unoccupied molecular orbital (LUMO) of the polymer may be tailored to optimize solar spectrum absorption and open circuit voltage in the solar cell device. Commonly used polymers including PTB7,[48] PBDB-T,[49, 50] PCDTBT[51] and PBTI3T[52] are shown in Figure 1.4. Purity and molecular weight (MW) have been shown to have a large effect on the efficiency of the resulting solar cell, so even solar cells made with a similar polymer under the same processing conditions can exhibit a wide range of power conversion efficiencies.[53-55]

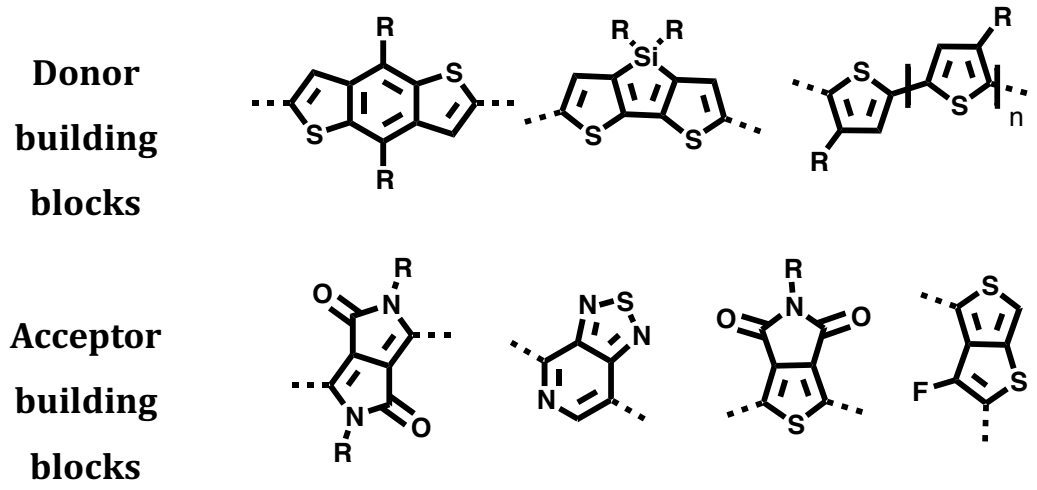

Figure 0.3. Commonly used building blocks for push-pull alternating copolymers and small molecules

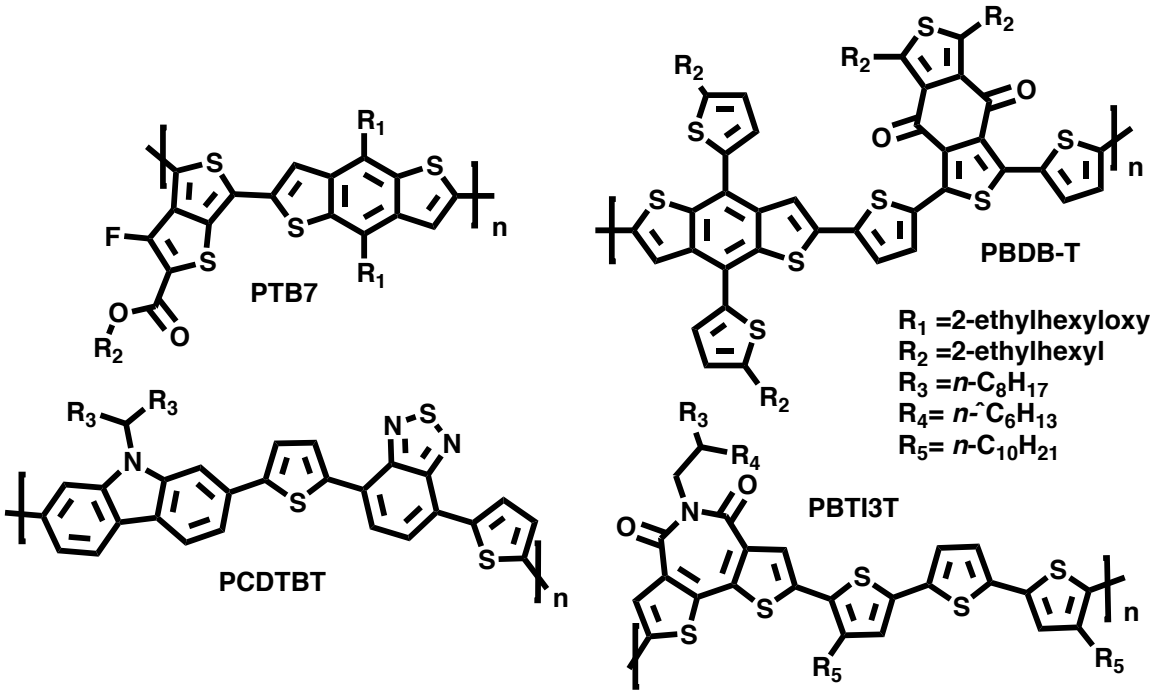

Figure 0.4. Selected high efficiency push-pull polymers

Small molecules (SM) offer an advantage over polymeric counterparts because of their inherent monodispersity and ease of synthesis resulting in less batch-to-batch variation.[56, 57] Solution processed SMs mimic the inherent dipole model of push-pull polymers and utilize many of the same building blocks shown in Figure 1.3. The dipole within the small molecule both decreases the Coulombic attraction in the exciton by localizing the hole and electron on different moieties within the SM thereby improving the probability of charge separation[58] and directing the crystallization of the small molecule domains, essential for charge transport.[59-61] Some small molecules are synthesized to create energy cascades using multiple units with varying electron withdrawing abilities.[62, 63] The highest PCE for a solution processed small molecule donor solar cells is 10.1% using DRCN5T:$PC_{71}BM$ as the active layer materials.[64, 65] Other commonly used small molecules are shown in Figure 1.5.

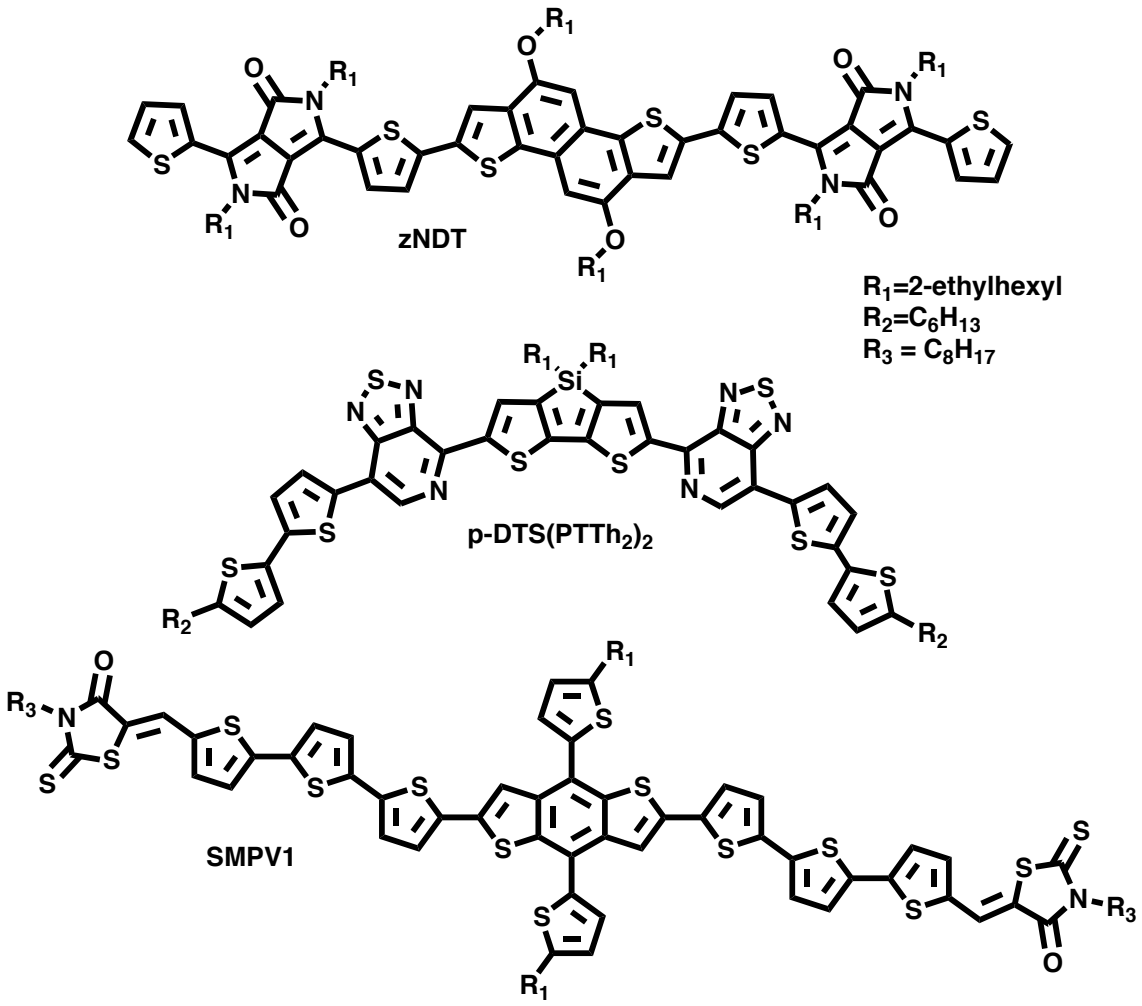

Figure 0.5. *p*-type donor small molecules with A – D – A building blocks

Both polymer and SMs are utilized as *n*-type accepting materials as well. The most common acceptor is fullerene-based, usually $PC_{61}BM$ or $PC_{71}BM$ (Figure 1.6). Studies suggest that fullerene based acceptors are superior due to their high degree of symmetry which allows for the formation of numerous degenerate states and facilitates charge separation without dependence on highly crystalline networks for efficient charge separation.[66] Polymer acceptors offer a similar advantage in the ease of charge transport but optimizing the interfacial geometry to facilitate charge separation is more difficult due to the lack of 3D symmetry in polymers. [67, 68] Recent studies show the promise of small molecule acceptors based on large conjugated planes, such as perylene diimides,[69-71] but simultaneous optimization of the crystallinity, interface geometry, and domain size has proven to be a challenge in BHJ solar cells.[70] Although new acceptor molecules demonstrate comparable efficiencies to their fullerene counterparts, they must be tailored to a given donor unlike PCBM which is universally compatible with all donor materials.[71] However, non-fullerene donors allow for the exploration of polymer and small molecule donors with non-ideal LUMOs relative to PCBM and allow for the development of low bandgap materials with absorption matched to the solar spectrum.

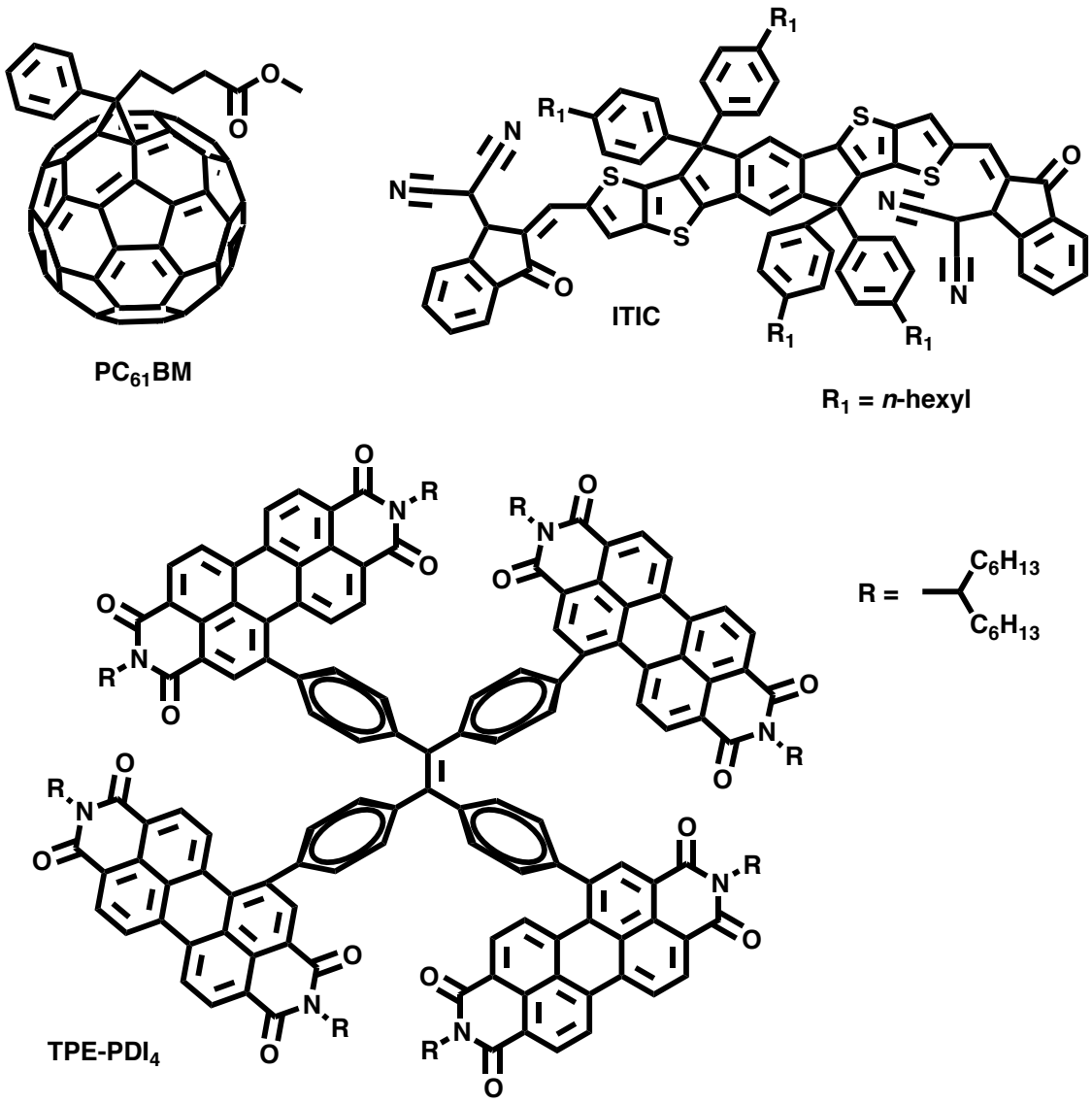

Figure 0.6. Commonly used *n*-type acceptor small molecules

1.3 Solar cell performance metrics

The power conversion efficiency (PCE) of a solar cell is evaluated using a *J-V* curve (Figure 1.7) which measures the solar cell current response at different voltages. The *PCE* is calculated using three figures of merit:

$$PCE = \frac{Jsc Voc FF}{P_{light}} \quad (1)$$

where J_{SC} is the short circuit current, V_{OC} is the open circuit voltage, and *FF* is the fill factor. P_{light} is the power of the light incident on the solar cell. The open circuit voltage (V_{OC}), a measure of the voltage at zero current, is affected by light intensity, temperature, and donor/acceptor pair materials.[72] In theory, the maximum V_{OC} achievable is usually estimated as $LUMO_{acceptor}$ - $HOMO_{donor}$ - 0.3 V, where the 0.3 V includes the energy required to overcome the Coulombic attraction of the exciton to create free charges.[73, 74] However, studies have demonstrated that systems may require more or less energy to create the charge separated state depending on the local energetics at the D/A interface[75-77] and electrode-active layer interface.[78]

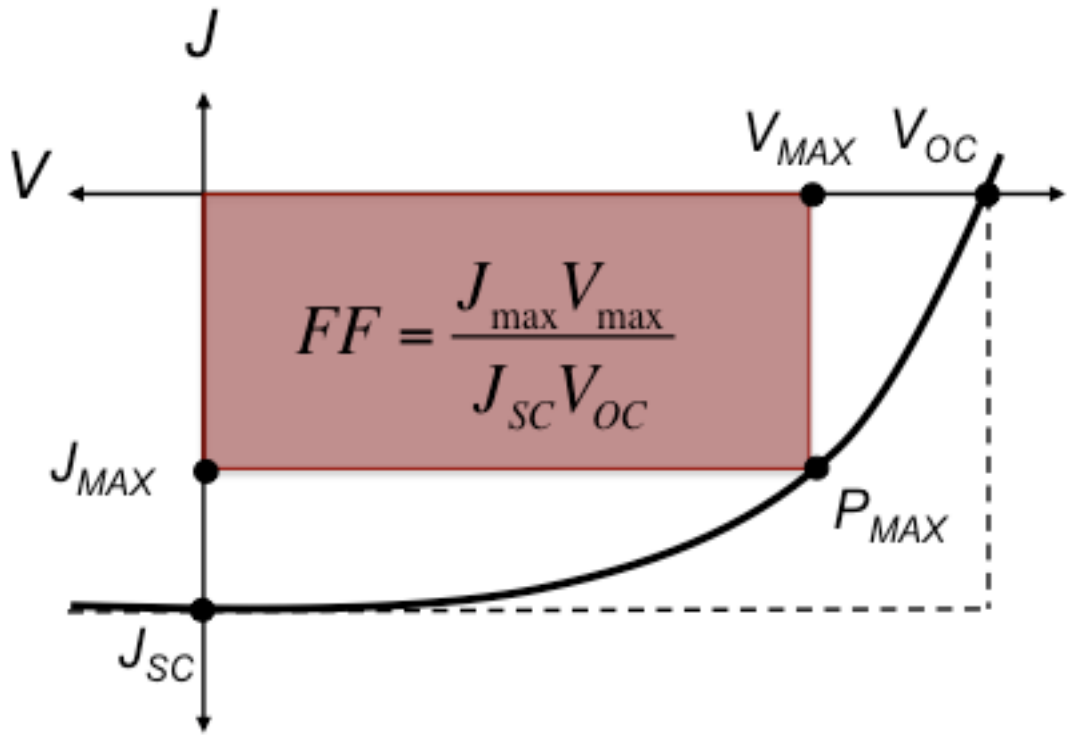

Figure 0.7. Illuminated *J-V* curve with figures of merit

The second figure of merit is the short circuit current (J_{SC}), a measure of the current at zero voltage. J_{SC} is determined by the number of free charges generated in the solar cell which is dependent on the net absorption spectrum of the active layer materials. Materials with narrow bandgaps absorb more of the solar spectrum and therefore have the potential to create more current[79, 80] while overlap of the absorption spectra of the donor and acceptor materials will result in lower J_{SC}.[81] This suggests that a thick active layer to absorb more light would be optimal for increased J_{SC}. However, J_{SC} is also reduced by recombination losses due to geminate recombination of the exciton and bimolecular recombination of the separated holes and electrons via trap states. Therefore, improvements in J_{SC} require either simultaneous increase in active layer thickness and domain interconnectivity and crystallinity to maximize charge collection, development of new materials to increase absorption of the solar spectrum while maintaining an adequate energetic offset with the acceptor LUMO to achieve high V_{OC}, or changes to device architecture to increase light absorption.

The final figure of merit is the fill factor (*FF*), a ratio between the highest possible power (J_{SC} x V_{OC}) and the actual maximum power on the *J-V* curve. The *FF* encompasses a number of variables including recombination events and exciton dissociation probability and is one of the most difficult parameters to optimize.[79] The *FF* is determined in part by the slope of the curve at the V_{OC} and J_{SC} which are related to the series resistance and the shunt resistance. The series resistance is a measure of the voltage losses associated with free charges crossing the interface(s) from the active layer to the electrodes. The shunt resistance is a measure of current losses within the active layer, so if the shunt resistance is high, then the amount of bimolecular recombination will also be high, and the *FF* will decrease because charges are trapped in the active layer.[79]

Because the *FF* is heavily dependent on recombination events, tuning the morphology of the solar cell to promote rapid charge extraction is essential to increased fill factor.[82] Solar cells with improved *FF*s include both crystalline pure domains and interpenetrating donor and acceptor mixed domains,[83, 84] domains with the π-stacked molecules parallel to the substrate to promote high charge mobility towards the electrodes,[85, 86] and/or vertical gradation of the active layer to reduce parasitic losses at the electrodes.[85, 87]

Because the figures of merit rely on a large number of structural and energetic factors, it is advantageous to characterize the fundamental processes of charge generation and recombination as well as the active layer morphology to assist in the optimization of a given system. Widely-used techniques for the study of the morphology and photophysical properties are detailed below with an emphasis on two techniques, x-ray scattering and transient absorption spectroscopy.

1.4 Characterizing morphology in organic solar cells

Characterization of the active layer morphology in organic solar cells presents an interesting challenge because the morphology is heterogeneous, purposefully neither crystalline nor amorphous. In addition, the active layer is thin (<300 nm) and organic materials have low electron density compared to inorganic materials making standard x-ray techniques difficult to employ. Therefore, a variety of techniques must be used to obtain a complete picture of the active layer since it is necessary to understand both the nanoscopic and microscopic morphology of crystalline and amorphous materials.

1.4.1 Grazing incidence x-ray scattering

To mitigate these challenges, grazing incidence x-ray scattering (GIXS) is used to elucidate the bulk thin film morphology.[88] In this technique, the incidence x-ray beam impinges at a glancing angle (usually ~0.2°) relative to the surface to minimize scattering from the substrate while completely penetrating the active layer resulting in high signal to noise ratio (Figure 1.8). The signal to noise ratio is improved with the use of a synchrotron x-ray source due to the brilliance of the incidence x-ray beam. The incident beam is scattered by the crystalline domains and the scattered beams are measured by a 2D photodiode array. The angle of scattering x-rays (θ) is inversely related to the interplanar distance, *d*, within a crystalline lattice by Bragg's law,

$$2d \sin\theta = n\lambda \quad (2)$$

where λ is the wavelength of the incident light. The *d*-spacing is inversely related to the scattering vector, *q*, by $d = 2\pi/q$. Therefore, x-rays that scatter at a wide angle ($q > 0.3$ Å^{-1}) provide information about the crystalline structure or ordering with domains while x-rays from domains (1-100 nm) scatter at a small angle (0.001 Å$^{-1} < q < 0.3$ Å^{-1}).

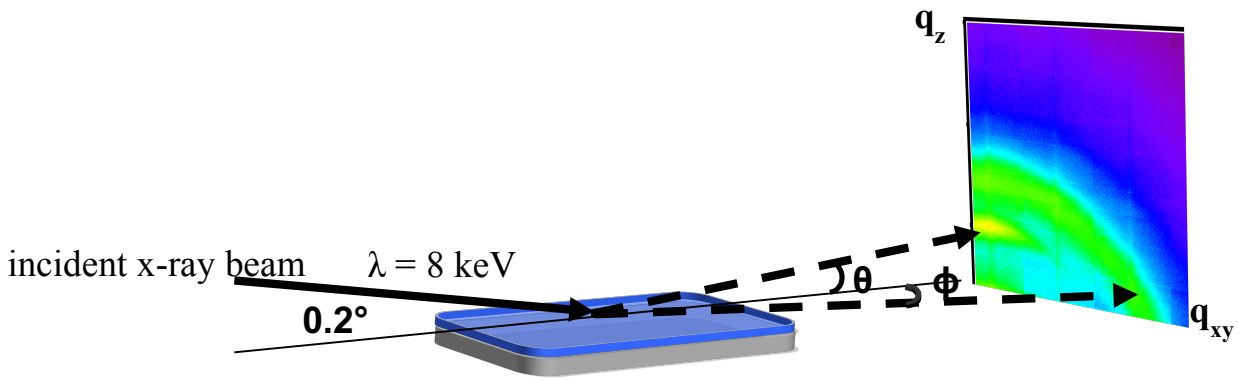

Figure 0.8. Schematic of grazing incidence x-ray scattering experimental design

Grazing incidence wide angle x-ray scattering (GIWAXS) is used to measure intercrystalline *d*-spacings up of 20 Å. The use of a 2D photodiode array detector allows for the resolution of GIWAXS scattering from structures both parallel and perpendicular to the substrate surface, where features that are perpendicular to the surface appear along the q_z axis and features that are parallel to the surface appear along the q_{xy} axis (Figure 1.9). Many polymers have low paracrystallinity and exhibit only a lamellar stacking reflection attributed to the side chain spacing and a π-stacking peak related to the separation of the π-conjugated backbones. In particularly rigid polymers, a scattering peak corresponding to the alternating monomers may be present as well as higher order reflections of the lamellar stacking.[89] By convention, the lamellar stacking reflection is referred to as (100) while the π-stacking is (010). In comparison, a typical small molecule GIWAXS image will exhibit numerous reflections which are most easily identified by comparing to the powder x-ray diffraction pattern or simulating the diffraction pattern. The number of diffraction peaks is related to the degree of crystallinity, where an increasing number of higher order peaks indicates a highly crystalline structure.

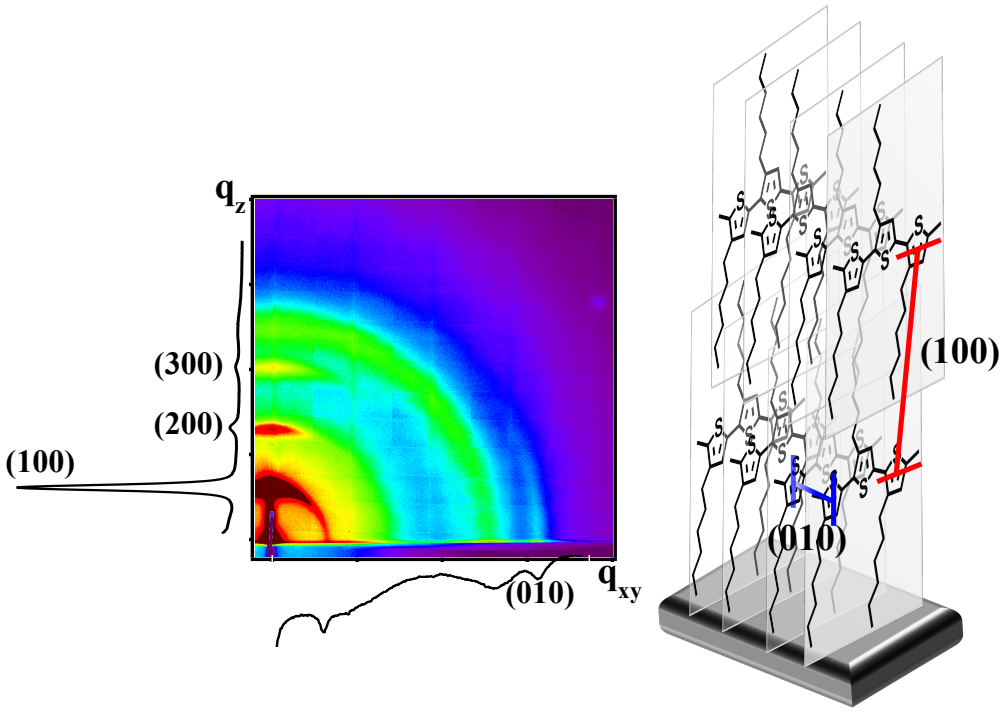

Figure 0.9. Grazing incidence x-ray scattering of poly-3-hexylthiophene (P3HT) including linecuts along the q_z and q_{xy} axis and corresponding lamellar and π-stacking crystal planes in P3HT crystal schematic

The width of the scattering peak is used to approximate the size of the crystallite using the Scherrer equation,

$$D_{hkl} = \frac{2\pi K}{\Delta q_{hkl}} \tag{3}$$

where D_{hkl} is the crystalline correlation length for a given reflection q_{hkl}, K is the Scherrer constant of about 0.9,[90] and Δq_{hkl} is the full width at half-maximum of the scattering peak. The breadth of the peak is corrected for x-ray beam divergence particularly at q > 1 Å^{-1} using

$$\Delta q_{res} = \frac{4\pi}{\lambda}\cos\left(\frac{2\theta_{hkl}}{2}\right)\frac{B_{res}}{2} \tag{4}$$

where q_{res} is the resolution in q of the instrumental resolution B_{res}.[91] The peak may also be broadened due to disorder in the crystal spacing or orientation, so the Scherrer analysis provides a minimum average crystalline domain size in thin films.

GISAXS provides additional information about amorphous or polycrystalline domains form 3 – 300 nm. The interpretation of GISAXS scattering in amorphous or semi-crystalline polymers uses the equations developed for rigid structures.[92] The GISAXS scattering trace can be divided into two regions: the Guinier knee and the Porod region (Figure 1.10). The Guinier and Porod equations are based on approximations in the small angle scattering equation in the high and low Q regimes. The Guinier equation is

$$I(Q) = \rho_0^2 v^2 e^{-\frac{q^2 R_g^2}{3}} \tag{5}$$

where $I(Q)$ is scattering intensity, ρ_0 is the average scattering length density, ν is volume, and R_g is the radius of gyration, dominates the scattering intensity in the low Q regime. The Porod equation is

$$I(Q) = \frac{2\pi(\Delta\rho)^2 S}{Q^4} \quad (6)$$

where $\Delta\rho$ is the difference in electron density between the solute and solvent and S is the boundary surface area between the aggregate and solvent. For rough or fractal surfaces, the power of q is reduced to 3 or 1-2, respectively.[93] The Porod equation is used in the high Q regime. The terms low Q and high Q are generally system dependent, but the Guinier is valid for $QR_g < 1$ and Porod is valid for $QR_g > 1$. Both of these approximations can be used to determine the size and shape of the aggregate, and texture of the aggregate surface in dilute solutions.[94]

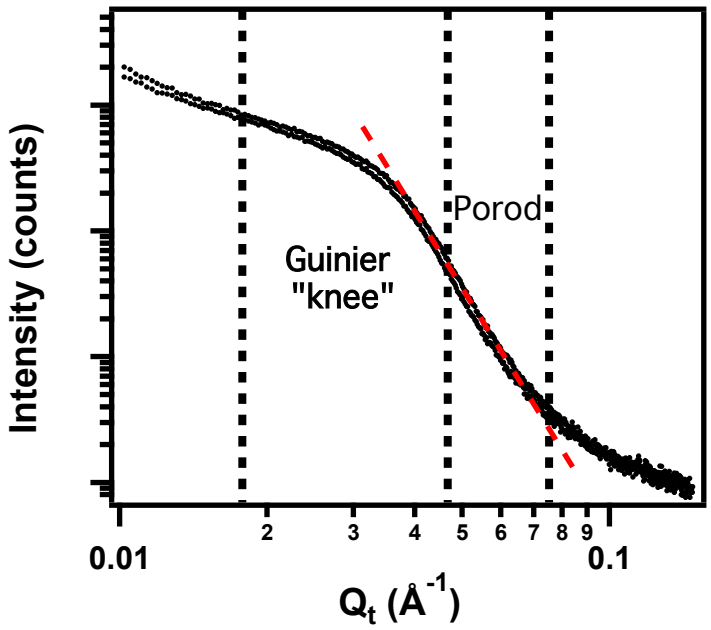

Figure 0.10. Grazing incidence small angle x-ray scattering trace showing the Guinier region which indicates the size of the domain and the Porod region, the slope of which indicates the surface structure

1.4.2 Scanning probe microscopy

In active layer systems with two materials, it is not possible to identify which domain is the donor versus the acceptor using GISAXS alone. In this case, transmission electron microscopy (TEM) and atomic force microscopy (AFM) are used to provide complimentary information.[95] TEM and AFM provide a visual of the film surface and allow imaging of distinct donor and acceptor domains based on the difference in conductivity between the donor and acceptor materials. Unfortunately, many active layers do not exhibit clear domain boundaries and on occasion the contrast between the donor and acceptor conductivities is low resulting in poorly distinguished images. Other active layers may exhibit vertical gradation so the image is non-representative of the bulk active layer.[96] However, these techniques allow for the visualization of the relative purity of the domains and an estimation of domain sizes. In highly crystalline materials, the crystalline size and shape and even packing structure may be determined.

1.5 Characterization of photophysical processes

The photogeneration of free charge carriers is a multistage process occurring over a time scale of femtoseconds to microseconds and the mechanism of this process is still a matter of debate. Transient absorption spectroscopy is a pump-probe technique that uses the absorption profiles of different excited state species to elucidate the mechanism for free charge generation.[97] The sample is initially irradiated with a flash of light at or greater than the energy of the singlet excited state to create an exciton population (Figure 1.11). The decay of this population is measured by a white light probe at regular time delays after the initial excitation. The timing

between the first excitation and the white light measurement dictates the limitation of the technique with an instrument response time of 50-80 fs possible, although attosecond transient absorption techniques exist.[98] Transient absorption is measured as a difference spectrum, so the first measurement of the white light spectrum looks approximately like an inverse of the absorption profile and is called the ground state bleach. Over time the features of the transient absorption spectrum evolve and the exciton, cation, anion, and/or additional features may be observed if they exhibit a singlet absorption signal in the experimental probe range, usually between 300 and 1400 nm.

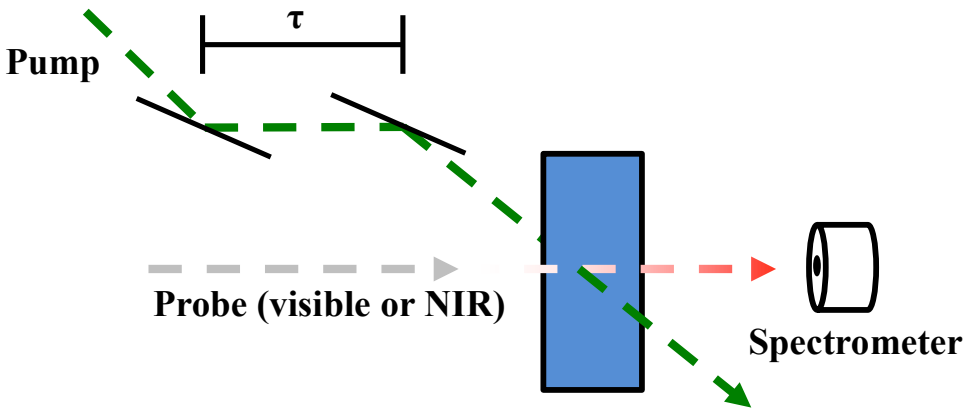

Figure 0.11. Schematic of transient absorption spectroscopy experimental setup where τ is a variable time delay

Transient absorption spectroscopy may be used to study multiple sample formats including solutions, neat thin films, and blended active layer films. Each of these samples provides information about a crucial step of the photogeneration process. In dilute solution, the dynamics of isolated molecules/polymer aggregates are probed, so dynamics of exciton formation and decay may be extracted. Neat thin film of the donor or acceptor exhibit dynamics of exciton formation in thin film as well as geminate recombination. Some neat polymer films and solutions have been shown to form a charge separated state, or cation, state as well with no acceptor present.[99] This has prompted debate about the spatial extent and energetic properties of excitons in push-pull polymer films with some evidence supporting the formation of delocalization of excitons over a nanometer scale.[100-102] Studies of blend active layer films have supported this delocalized exciton mechanism of charge generation in certain high efficiency polymer systems in which a charge separated state is observed within the instrument response time (<50 fs).[102, 103] In other polymer systems, spectral signatures for charge transfer states are observed suggesting the exciton diffusion mechanism.[40] In addition, the decay rates for each species can indicate the type of decay and pinpoint key efficiency losses including energetic or morphological trap states that promote bimolecular recombination and/or poor donor-acceptor energetic overlap.

1.6 Solar cell processing conditions

Organic solar cells are immensely complex and constantly evolving devices which are heavily dependent on the donor and acceptor materials used. Spin casting a blend of polymer and PCBM generally results in an overmixed morphology which lacks a bicontinuous network,

so several techniques may be employed at different stages of device processing to improve the morphology and final solar cell efficiency. The donor-acceptor ratios in solution may be adjusted to optimize segregation of donor and acceptor domains[104, 105] or promote donor-acceptor co-crystallization or templating in certain systems.[106-108] After spin coating, the film may be annealed to allow for the formation of larger or more crystalline domains.[109-111] Multiple solvents can be used to adjust the rate of solvent evaporation in the spin coating process to control donor or acceptor domain formation.[112] In particular, minute quantities (<3% vol/vol) of high boiling point solvent additives have seen success at improving thin film morphology in solar cells although the mechanism of improvement is still unclear.[38, 113-115] Each of these processing techniques is highly materials dependent, so understanding the fundamental morphological and photophysical relationships in a given matrix of donor-acceptor materials and developing general principles for the mechanism of charge generation in organic solar cells is paramount to improve solar cell efficiency to levels for feasible commercialization.

Chapter 2. Effects of Additives on the Morphology of Solution Phase Aggregates Formed by Active Layer Components of High-Efficiency Organic Solar Cells

2.1 Introduction

Increasing worldwide energy demands and environmental concerns about the impact of fossil fuel combustion have stimulated the quest for alternative energy sources. Bulk heterojunction (BHJ) organic photovoltaic (OPV) cells[24] are promising devices for alternative energy sources because they are composed of earth-abundant materials that are solution-processable, and therefore, cost-effective for large scale manufacture. Large scale implementation is currently limited by power conversion efficiencies (PCEs) of ~7.5%[48] while >10% is highly desirable for commercial viability.[116] One factor constraining BHJ device PCEs is the morphology of the interpenetrating networks of donor and acceptor materials in the photoactive layer. To achieve high PCEs, the network must have multiple interfaces for efficient charge separation and long percolation pathways for efficient charge transfer, requiring an ideal BHJ donor/acceptor domain length scale of ≤10 nm.[25, 117] Many largely empirical methods have been applied to achieve such morphologies, including post-production annealing,[30, 111, 118] solvent annealing,[34, 119, 120] and the introduction of processing additives.[121, 122]

OPV processing additives offer an attraction over annealing processes in that they do not require an additional fabrication step. Two general guidelines for additive design are: 1) the boiling point must be significantly greater than that of the processing solvent to maximize the

interaction time between the additive and the active layer components during thin film formation, and 2) one active layer component must be significantly more soluble in the additive than the other component.[121] Recent promising additives fulfilling these guidelines include alkanedithiols, for which fullerene acceptor solubility and the resulting BHJ film morphologies have been characterized,[123] and di(X)octanes, where X is a small, polarizable group such as halogen.[9] For BHJ systems containing donor polymers such as **PTB7**,[48] **PCPDTBT**[124] and others,[125] 1,8-diiodooctane (DIO) affords the largest PCE enhancements observed to date.

The high-PCE donor polymer **PTB7**, composed of alternating thieno[3,4-*b*]thiophene and benzodithiophene units, affords a PCE of 7.4% when combined with the fullerene acceptor, [6,6]-phenyl-C_{71}-butyric acid methyl ester (**$PC_{71}BM$**; Figure 2.1).[48] The large PCE is attributed to both the low **PTB7** band gap, affording efficient capture of solar photons, and an ideal film morphology with domain sizes of ~10 nm,[48] with $PC_{71}BM$ molecules intercalating into the PTB7 network.[126] Note that this efficacious morphology is only achieved by DIO addition, which increases the PCE by 33%.[48] While several studies reveal that processing additives promote more favorable BHJ morphologies,[127] little is understood about the microstructural evolution occurring in the transformation from solution-phase BHJ precursors to thin photoactive films.[8] In this small angle x-ray scattering (SAXS) investigation on active layer **PTB7**: **$PC_{71}BM$** solutions, we find that these species are heavily aggregated, and that DIO significantly affects the level of aggregation. A mechanism for thin BHJ film formation is hence proposed based on our results.

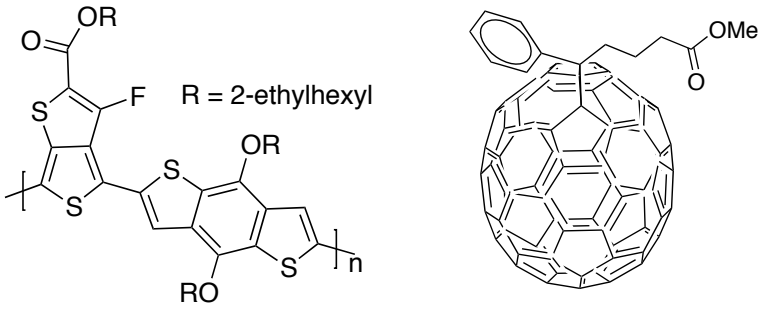

PTB7 $PC_{71}BM$

Figure 2.1. Structures of active layer components

2.2 Experimental

2.2.1 Solution sample preparation

To mimic BHJ cell fabrication conditions, the concentrations of the active layer components used were the same as those for optimized devices. The synthesis of **PTB7** has been described previously.[128] The **PTB7** (10 mg/mL; M_n = 42 KD, PDI=2.2) and **$PC_{70}BM$** (15 mg/mL, Sigma Aldrich >99%) were dissolved in anhydrous chlorobenzene (CB; Sigma Aldrich) in a dry N_2 glove box (<1ppm O_2, <1 ppm H_2O). The solutions were heated and stirred overnight at 40°C to ensure complete dissolution of the **PTB7**. Next, 1,8-diiodooctane (DIO; Sigma Aldrich >98%; 3% v/v) was added to selected solutions 1 h prior to characterization. All samples were removed from heat 1 h prior to characterization. Both single component **PTB7** and **$PC_{71}BM$** solutions as well as mixed **PTB7**:**$PC_{71}BM$** solutions (1:1.5 w/w) in chlorobenzene (CB) were studied either with the standard concentration of 3% v/v DIO or without DIO. The **PTB7** and **$PC_{71}BM$** concentrations were 10 mg/mL and 15 mg/mL, respectively.

2.2.2 Small angle x-ray scattering

Solution characterization was carried out by transmission SAXS at Beamline 5ID at the Advanced Photon Source (APS) of Argonne National Laboratory. Solution scattering was performed in the transmission mode using a collimated x-ray beam of 8 keV. To minimize x-ray damage, solutions were characterized in a 1.5 mm quartz flow cell with a flow rate of 10 μL/s. The flow cell was thoroughly cleaned between samples with CB. Data were collected using a two-dimensional area MAR detector which was situated 1500 mm from the sample. For each sample, the corresponding CB(+DIO) scattering exposure was taken immediately before the

sample was exposed for use in solvent background subtraction. Results are presented in terms of the reciprocal space variable Q which is approximately related to the d-spacing by $Q = 2\pi/d$. The experimental Q range (0.01 $Å^{-1} < Q < 0.8$ $Å^{-1}$) corresponds to 8 Å < d < 628 Å.

2.2.3 X-ray scattering fitting procedures

Solvent subtraction For each sample scattering signal, the chlorobenzene (CB) scattering signal (Figure 2.2) was subtracted. Due to the strong scattering of the CB solvent, it is difficult to completely remove the solvent scattering at higher Q ($Q > 0.6$ $Å^{-1}$). In both the samples and solvent traces, we see an intensity decrease as Q increases. While this high scattering signal at low Q can indicate large aggregates, we believe that it can be attributed to experimental set-up used in which an exponential decrease of scattering intensity is frequently seen especially for this lower Q ($Q < 0.5$ $Å^{-1}$ regime).

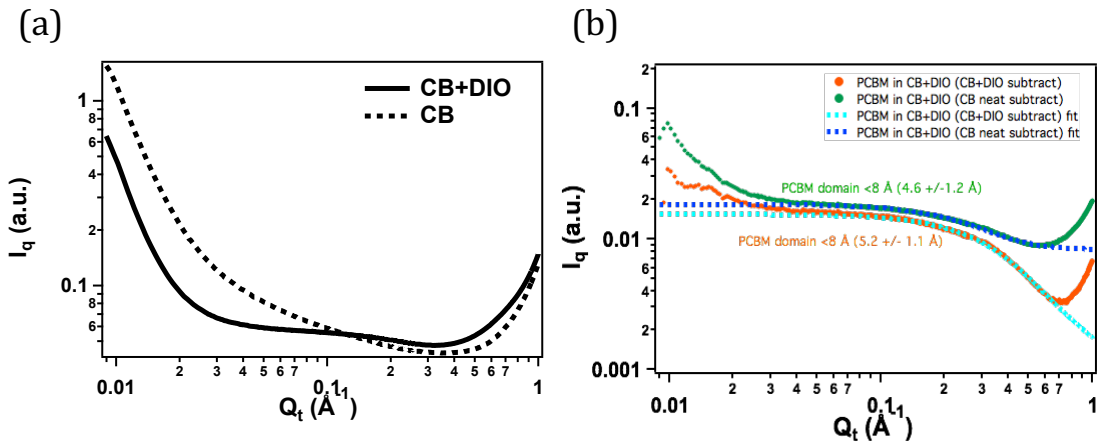

Figure 2.2. a) Scattering signal from CB solvent without DIO. b) The accompanying figure shows the difference in the subtracted signals using a background with or without DIO

Standard Modeling 1 fitting procedure The scattering profiles were fit using Modeling I, Standard Models developed by J. Ilavsky for Igor Pro[129] based on the standard small angle scattering equation,

$$I(Q) = |\Delta\rho|^2 \int_0^\infty |F(Q,r)|^2 V(r)^2 NP(r) dr \quad (7)$$

where *I(Q)* is intensity, *Δρ* the difference in electron density between the scattering particle and the surrounding medium, *F(Q,r)* the form factor, *V(r)* the particle volume, *N* the total number of particles that scatter, and *P(r)* the probability of a scattering particle with radius *r*. For all systems, we assume spherical aggregates and fit experimental *I(Q)* as a function of *Q* assuming either two or three log normal distributions of aggregate size, allowing the mean size, aggregate volume, and distribution widths to vary. We assume that all of the peaks present are due to an aggregation dimension rather than the form factor, a shape dependent function, of the aggregate. A step-by-step description of the regional fitting of **PTB7** without DIO is shown below based on three *Q* regions: $Q > 0.3$ Å^{-1}, 0.1 Å$^{-1} < Q < 0.3$ Å^{-1}, and $Q < 0.1$ Å^{-1}.

Starting at the high *Q* regime we calculate the first size distribution (Figure 2.3) allowing the mean size, distribution width, and aggregate volume to vary.

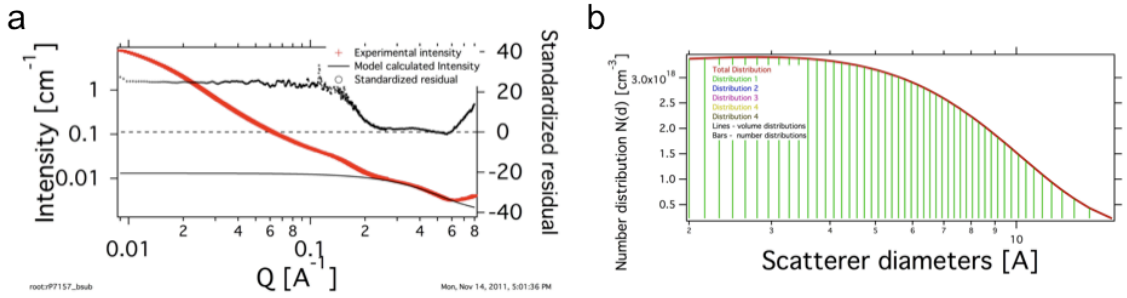

Figure 2.3. Level 1 distribution of peak in high Q regime (Q ~0.4 Å^{-1}): a) fit and residual, and b) log normal distribution

We next fit the second highest peak which we attribute to aggregate size again allowing mean size, aggregate volume, and distribution width to vary.

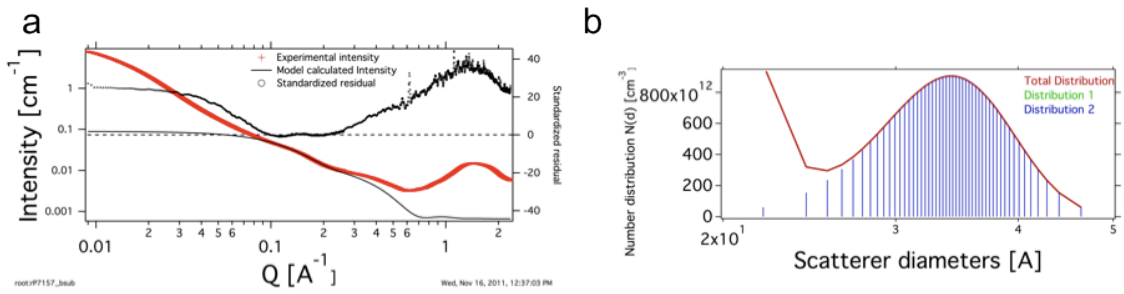

Figure 2.4. Level 2 distribution of peak in middle Q regime (Q ~0.15 Å^{-1}): a) fit and residual, and b) log normal distribution

We then fit the low Q regime (0.01 $Å^{-1}$ < Q < 0.1 $Å^{-1}$).

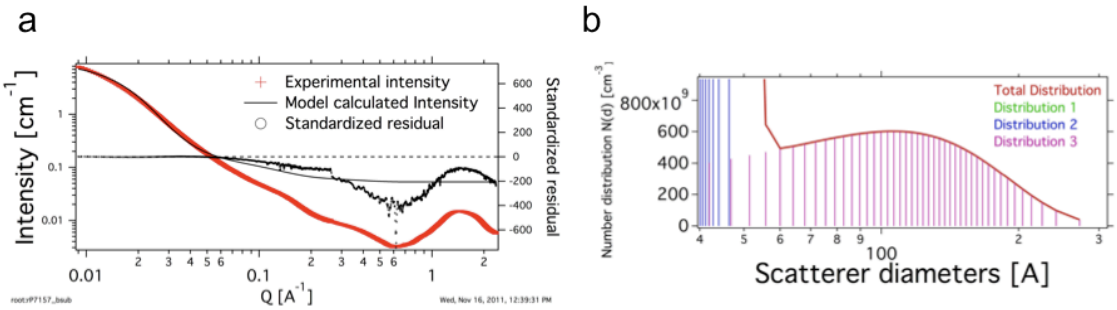

Figure 2.5 Level 3 distribution of peak in the low Q regime (Q <0.1 $Å^{-1}$): a) fit and residual, and b) log normal distribution (pink)

Finally, holding the mean size constant, the entire scattering trace was fit using all three distributions (Figure 2.6).

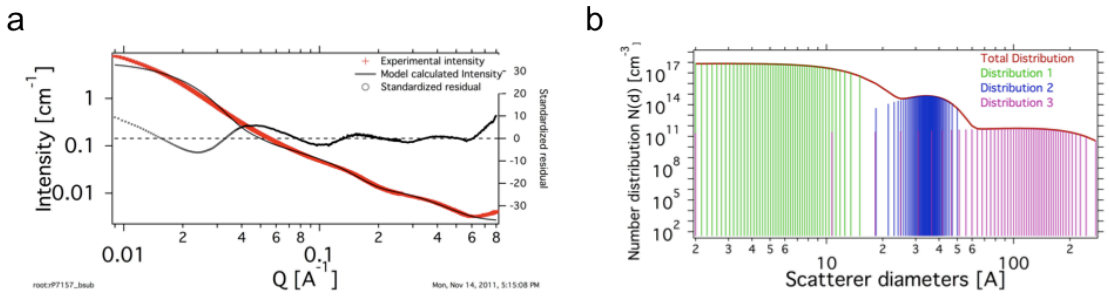

Figure 2.6. a) Total fit of PTB7 curve using all three distributions. b) Total distribution of scatterer diameter sizes. Distributions are color coded so that distribution 1 (green) corresponds to the Level 1 fit (high *Q*), distribution 2 (blue) corresponds to the Level 2 fit (mid *Q*), and distribution 3 (pink) corresponds to the Level 3 fit (low *Q*). The total distribution is shown in red

This standard model fit procedure yields an approximate minimum aggregate size and allows comparison of relative aggregation patterns rather than determination of absolute aggregate size.

2.3 Results and Discussion

PTB7 aggregation in CB solutions with and without DIO were first investigated. The SAXS results reveal a double peak structure, suggesting multiple aggregate dimensions from multiple sizes of spherical aggregates or a non-spherical aggregate shape. When the scattering profile is fit assuming spheroidal aggregates, the mean radii of the peak distributions are (34.2±0.4) Å and <8 Å within the limits of the experiment (Figure 2.7a, red trace). Since the second value is too small to attribute to aggregation, we suggest it corresponds to an intra-aggregate distance, such as π-π stacking of the polymer backbone[1,2] within an aggregate. The **PTB7** aggregate radius is 34.2 Å, and this large size likely reflect the high **PTB7** concentration and low **PTB7** solubility. When DIO is added to the CB solution, the **PTB7** scattering signals have very little changes (Figure 2.7a), and the data fitting results in a slightly larger aggregate radius of (36.7±0.8) Å with a similar small intraaggregate distance <8 Å. Hence, upon DIO addition, there is a small increase in the overall aggregate size.

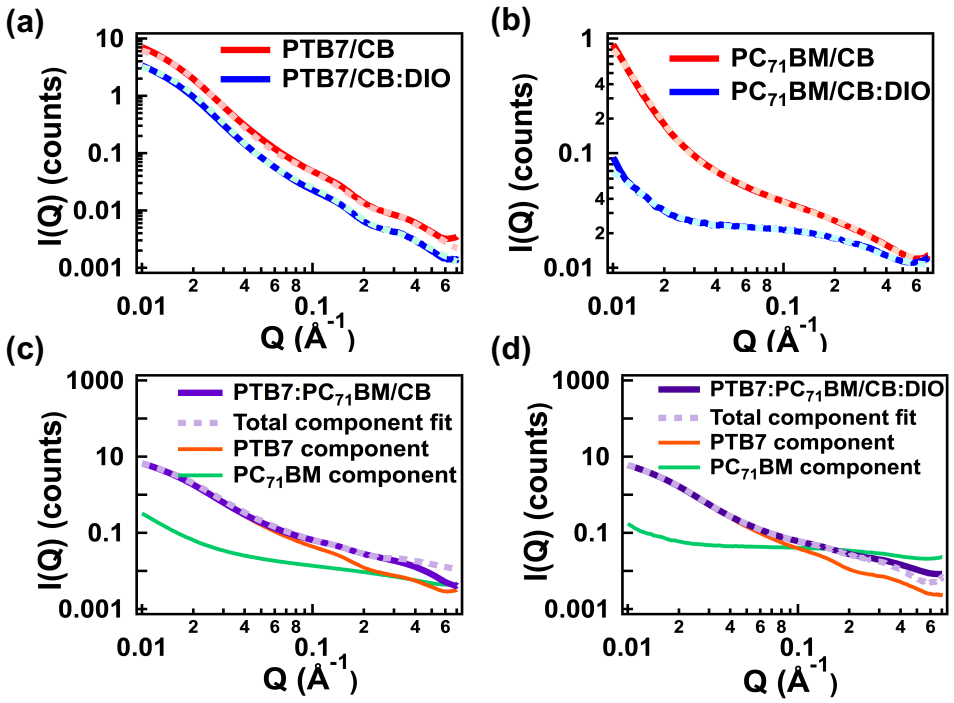

Figure 2.7. Experimental scattering profiles of active layer solutions (solid lines) and fits (dotted lines), comparing aggregation in CB and CB:DIO solutions of: (a) PTB7 (offset) and (b) $PC_{71}BM$, and two-component fits of PTB7:$PC_{71}BM$ in: (c) CB and (d) CB:DIO.

Next, the effects of DIO on **$PC_{71}BM$** aggregation were investigated. The single peak in the scattering profile and the spheroidal **$PC_{71}BM$** shape suggests that $PC_{71}BM$ forms spheroidal aggregates (Figure 2.7b). Using the aforementioned fitting procedure, we find that the mean radius of the aggregates is (11.5±0.5) Å without DIO and <8 (fit radius of 5.7±1.1) Å with DIO. In addition, the signal intensity is significantly lower for the **$PC_{71}BM$** species in the CB:DIO solution, suggesting that there are fewer aggregates. While DIO molecules cause only slight changes in the size of the **PTB7** aggregates in solution, they selectively and completely dissolve the **$PC_{71}BM$** aggregates.

We next confirmed that the aggregation patterns in the single component solutions are the same as in the blend solution by two methods. The first was a component fit in which the scattering intensity contributions of the **PTB7** and **$PC_{71}BM$** aggregates are separated by fitting the blend solution scattering trace *B(Q)* with the traces of the single component solutions,

$$B(Q) = k_0 P(Q) + k_1 C(Q) + k_2 \quad (8)$$

where *B(Q)* is the scattering profile of the blend solution, *P(Q)* the scattering profile of the **PTB7** solution, *C(Q)* the scattering profile of the **$PC_{71}BM$** solution, and k_0, k_1, and k_2 are fitting coefficients that describe the relative contributions of *P(Q)* and *C(Q)* to *B(Q)*. For the CB solutions, we find k_0 = 0.904 ± 0.001, k_1= 0.363 ± 0.007, and k_2 = 0.004 ± 0.002 indicating that the blend solution scattering has 71% **PTB7** character, meaning that the **PTB7** aggregates display increased scattering intensity compared to **$PC_{71}BM$** (Figure 2.7c).

We also confirm that there is a small change in the **$PC_{71}BM$** aggregate size upon addition of **PTB7** in the blend solution, but the trend of decreasing aggregate size is still evident. To obtain these traces, the **PTB7** component from the component fits (Figures 2.7c, d) was subtracted from the blend traces leaving only the **$PC_{71}BM$** component (Figure 2.8).

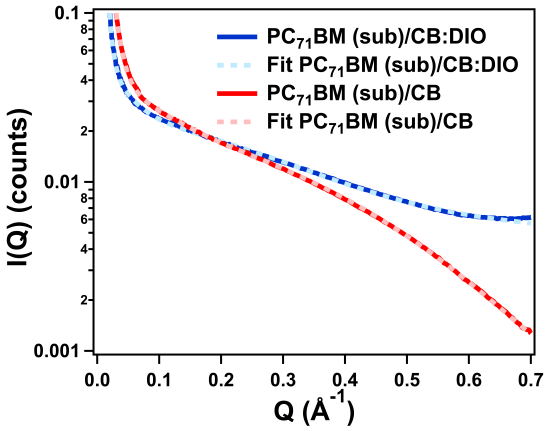

Figure 2.8. Fits of $PC_{71}BM$ traces obtained by subtracting PTB7 component fit from the blend traces

Increased scattering intensity can be related to higher electron density, arguing that the strong **PTB7** scattering is due in part to the higher **PTB7** aggregate electron density versus the **$PC_{71}BM$** aggregates. For the CB:DIO solutions (Figure 2.7d), $k_0 = 0.861 \pm 0.001$, $k_1 = 1.894 \pm 0.093$, and $k_2 = -0.019 \pm 0.002$, suggesting that **$PC_{71}BM$** now scatters more strongly than the **PTB7** aggregates. Since there is very little change in the aggregation of **PTB7**, its electron density remains the same in both solutions. However, the **$PC_{71}BM$** electron density increases when DIO is added to the CB solution. This increase is due to a change in the unit volume electron density of the **$PC_{71}BM$** aggregates rather than a change in the average electron density over the entire solution. The electron density of a single molecule of **$PC_{71}BM$** in the CB:DIO solution may be higher than the electron density of a cluster of **$PC_{71}BM$** molecules in the CB solution and therefore, the **$PC_{71}BM$** molecule will have a stronger scattering signal than the **$PC_{71}BM$** aggregate. Because of the large **PTB7** component in the blend scattering profiles, the **PTB7** scattering profile was next subtracted from that of the blend to determine the **$PC_{71}BM$** aggregate size. It is found that **PTB7** addition to the **$PC_{71}BM$** solution has little effect on the **$PC_{71}BM$** aggregate size (Figure 2.9).

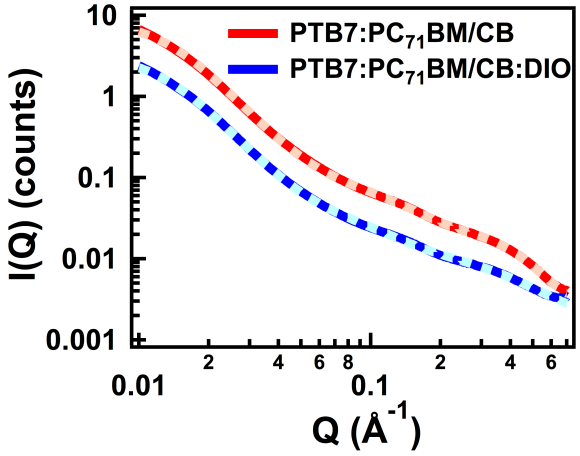

Figure 2.9. Standard Modeling I fit for PTB7:PC_{71}BM blend solutions assuming three Gaussian distributions of aggregates. PTB7:PC_{71}BM/CB:DIO is offset by a factor of 0.5.

2.4 Conclusion

DIO is an effective additive in this BHJ OPV system since it fulfills the requirement of a high boiling point and selective **$PC_{71}BM$** dissolution. Without DIO, the **$PC_{71}BM$** aggregates are large which hinders **$PC_{71}BM$** intercalation into the **PTB7** network during film formation, so that large, segregated domains form (Figure 2.10a). However, on DIO addition, the **$PC_{71}BM$** aggregates dissolve (Figure 2.10b). This facilitates integration of the **$PC_{71}BM$** molecules into the **PTB7** aggregates. Furthermore, because **$PC_{71}BM$** is selectively dissolved in DIO and DIO is relatively non-volatile, there is sufficient time for the **$PC_{71}BM$** molecules to integrate into the **PTB7** aggregates, resulting in a greater donor-acceptor interface density and smaller domains.

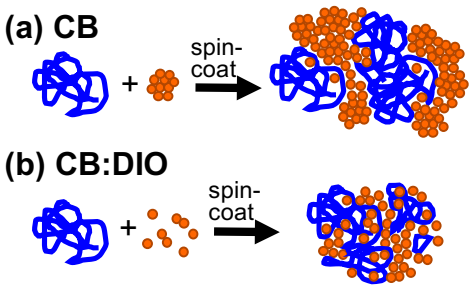

Figure 2.10. Schematic of PTB7 and $PC_{71}BM$ aggregation in: (a) CB and (b) CB:DIO and the resulting film morphology

Using solution phase SAXS we have shown that DIO addition to a CB solution completely dissolves the **$PC_{71}BM$** aggregates, promoting formation of smaller domains and greater donor-acceptor interpenetration within the film. A deeper understanding of the mechanism of film formation will assist in the selection of ideal processing additives for future BHJ solar cell systems.

Chapter 3. Effects of 1,8-Diiodooctane on Domain Nanostructure and Charge Separation Dynamics in $PC_{71}BM$-Based Bulk Heterojunction Solar Cells

3.1 Introduction

Recent advances in power conversion efficiency (PCE) of organic photovoltaic (OPV) devices demonstrate their potential in providing electricity via alternative energy sources.[130-134] Until very recently, most of these single-junction devices are bulk heterojunction (BHJ) OPV devices in which the charge-generating active layer consists of a mixture of a p-type electron donor polymer[44, 135-137] and a fullerene-based electron acceptor such as phenyl-C_{71}-butyric-acid-methyl ester ($PC_{71}BM$). Upon absorption of photons, excitons are formed in the polymer domain, which subsequently dissociate into holes and electrons at the polymer-$PC_{71}BM$ interfaces, driven by the energetic offset between the polymer LUMO and the $PC_{71}BM$ LUMO. The holes and electrons generated via exciton splitting travel through their respective interconnected polymer and $PC_{71}BM$ domains to the appropriate charge-collecting electrodes. Despite the rising power conversion efficiencies (PCEs), the design of consistently high-performing BHJ polymer solar cells presents a challenge, reflecting the inherent energetic and morphological complexity of these systems.[84, 138-148]

Energetic models of ideal solar cell polymers have been articulated[138, 149] and provide the impetus for the design of many current-generation donor polymers.[137, 150] However, it is well known that even polymers with "perfect" energetic characteristics may not exhibit

correspondingly high PCEs due to limitations in either the short circuit current (J_{sc}) or fill factor (*FF*), as well as local structural irregularities.[151-157] Often this lack of device performance predictability is attributed to "non-ideal morphology," where, in extreme cases, either the polymer and the fullerene are fully segregated with relatively small or energetically unfavorable interfacial boundaries,[131, 153, 155] thereby compromising efficient charge generation, or the two are completely intermixed resulting in a loss of domain connectivity, creating high densities of charge-trapping islands.[151] Many fabrication techniques have been utilized to improve the morphology of BHJ systems including thermal annealing,[143, 158-166] polymer:fullerene ratio optimization,[51, 104, 167-170] and solvent additives.[122, 124, 163, 171-175] In particular, solvent additives have provided the great control over film morphology since they facilitate independent formation of polymer and fullerene domains based on their different solubilities.[36, 176-178] Typically, appropriate solvent additives also have high boiling points compared to commonly used film casting solvents (e.g., chlorobenzene, chloroform, toluene, etc.) which extends the time for the polymer and fullerene to organize into ordered domains.[179-184]

Previous work has amply demonstrated that the addition of solvent additives modifies the resulting BHJ film morphology[48, 83, 115, 179, 181, 185-188] and energetics, [189, 190] although the exact effects vary with the solvent additive and polymer system. Broadly speaking, solvent additives can play either of two roles to balance film morphology. In some cases, solvent additives can improve polymer + $PC_{71}BM$ domain formation and phase segregation and often concurrently, solubilize the alkyl side chain substituents of the polymer, promoting the formation of more crystalline and pure polymer domains.[179, 188, 191] For systems in which the polymer and $PC_{71}BM$ are very miscible, OPVs without solvent additives exhibit high levels of charge recombination

due to the formation of $PC_{71}BM$ "islands" that prevent long-range charge transport after exciton splitting and hence result in charge trap creation, leading to geminate charge recombination.[181, 188, 191] In other cases, solvent additives can break up large segregated domains and/or create more mixed phase domains. For example, when 3 vol% DIO is added to the PTB7:$PC_{71}BM$ system, the domains decrease in size leading to significantly increased J_{sc} and *FF,* and a corresponding PCE increase of 150%.[48, 83, 192] We have previously attributed the improved morphology in the PTB7:$PC_{71}BM$ system with DIO to the selective dissolution of $PC_{71}BM$ aggregates in DIO favors the creation of a more interpenetrated PTB7-$PC_{71}BM$ network via slow crystallization.[183, 193]

In general, while BHJ morphology optimization must simultaneously enable effective exciton splitting and rapid charge transport in the OPV device active layer, an optimal morphology for a particular BHJ system is often hard to predict and control. While the active layer film morphology can range from a uniform distribution of donor and acceptor (one-phase morphology) at one extreme to large crystalline donor and/or acceptor domains (two-phase morphology) at the other, most polymer solar cells encompass a three-phase morphology consisting of pure donor domains, pure acceptor domains, and intermixed donor-acceptor regions on multiple length scales.[108, 194-196] In BHJ systems some mixing of the donor polymer and $PC_{71}BM$ is inevitable, however the type of mixing can vary widely from regularly intercalated $PC_{71}BM$ in crystalline polymer networks (e.g., pBTTT)[85, 106, 107, 196-198] to fully blended amorphous polymers with $PC_{71}BM$.[83, 199-204] In the former, it is found that increased $PC_{71}BM$ intercalation into the pBTTT crystalline network affords increased charge separated populations and J_{sc}, but also increased geminate charge recombination[205] and decreased *FF* due to the lack of

continuous $PC_{71}BM$ networks for electron extraction.[106] Similarly, in OPVs with semi-crystalline or amorphous donor polymers, smaller pure $PC_{71}BM$ and polymer domains and hence, increased polymer–$PC_{71}BM$ interfacial areas, afford increased charge-separated state populations,[206-208] and/or decreased charge transfer state populations.[102, 138, 209] However, large donor-acceptor interfacial areas can also lead to in charge recombination due to inadequate donor or $PC_{71}BM$ charge percolation pathways.[210, 211]

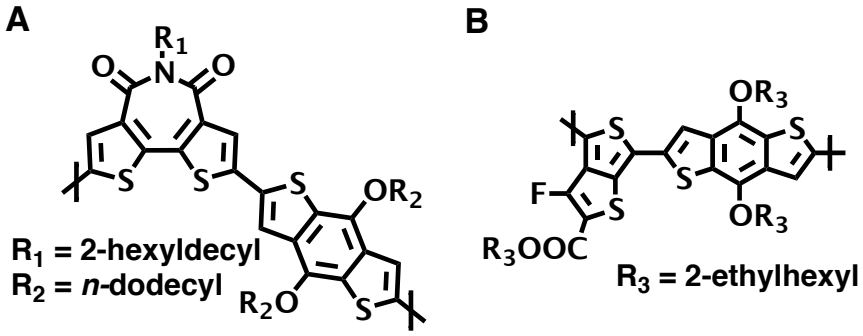

Figure 3.1. Chemical structures of the electron donor polymers A) PBTIBDT and B) PTB7

In previous work with the bithiophene imide-benzodithiophene copolymer (PBTIBDT) (Figure 3.1), addition of 3.0 vol% DIO to the film casting solution significantly increased both the OPV J_{sc} and FF.[212, 213] To better understand this performance increase, here we study the microstructural effects of varying the DIO content from 0.0 – 5.0 vol% on solution phase $PC_{71}BM$ and PBTIBDT aggregates using X-ray scattering methods, and relate changes in aggregate size to the crystalline correlation lengths and domain sizes in the resulting BHJ thin films. To further resolve whether these film morphology changes affect electronic processes in the BHJ films at different steps relevant to the OPV functions, we investigated the initial exciton splitting yields, using transient optical absorption measurements as a function of the DIO-induced morphology changes, and characterized the free carrier populations from 300 fs to >10 ns after the light excitation, and to relate these changes to the performance metrics of the corresponding devices. These results provide an incisive indirect method of probing the mixed regions of the BHJ films and highlight the extent to which processing additives optimize thin film morphology on multiple length scales.

3.2 Methods

3.2.1 Materials synthesis

The PBTIBDT synthesis and purification were carried out as previously described.[212] Comparable molecular masses (34 kD) and polydispersities (PDI = 2.3) were obtained. An inverted device structure, ITO/ZnO/PBTIBDT:$PC_{71}BM$/MoO_x/Ag, was used to characterize solar cell metrics. Pre-patterned ITO substrates (Thin Film Devices, Inc.) with a series resistance of ~8Ω were sonicated sequentially in hexane, DI water, methanol, isopropanol, and acetone for 30

min and then UV/ozone treated (Jelight Co.). Amorphous ZnO layers were deposited via a sol-gel process on the ITO substrates and then annealed in air for 5 min at 150°C. PBTIBDT:$PC_{71}BM$ active layer solutions were prepared in anhydrous *o*-dichlorobenzene (ODCB, Sigma Aldrich, 99.9% purity) with a 1:1.5 w/w ratio of PBTIBDT:$PC_{71}BM$ with a concentration of 10 mg/mL PBTIBDT and heated and stirred 12 h at 60°C to completely dissolve the polymer. When applicable, 1,8-diiododoctane (DIO; Sigma-Aldrich) was added to the active layer solution after 12 h in 1.0 – 5.0 vol%. The active layer solution was then spun-cast at 1250 rpm on the ZnO layer in an N_2 dry box to obtain thicknesses of 100 nm. Thin layers of MoO_x (5 nm) and Ag (100 nm) were subsequently thermally evaporated through a shadow mask at ~10^{-6} Torr. The solar cell was encapsulated by a glass slide and UV-curable epoxy prior to testing.

3.2.2 Device characterization

Device *J-V* characteristics were measured under AM1.5G light (100 mW/cm^2) using a Xe arc lamp of a Spectra-Nova Class A solar simulator. The light intensity was calibrated using an NREL-certified monocrystalline Si diode coupled to a KG3 filter to bring the spectral mismatch to unity. Four-point contact measurements were performed and electrical characterizations were measured with a Keithley 2400 unit. The area of all devices was 6 mm^2.

3.2.3 Solution structural characterization

Solution small-angle X-ray scattering (SAXS) was performed at Beamline 5ID-D at the Advanced Photon Source (APS) at Argonne National Laboratory (ANL). Identical conditions were used to prepare the solutions studied, including neat PBTIBDT solutions, neat $PC_{71}BM$ solutions, and PBTIBDT: $PC_{71}BM$ blend solutions with 0.0 –5.0 vol% DIO in ODCB. Solutions

were flowed through a 100 μm quartz capillary at 10 μL/s and illuminated with an 8 keV X-ray beam in a 50-μm spot size. Scattering signals without (dark) and with X-ray illumination were collected on two overlapping MAR detectors using a series of ten 3-min exposures, and the corresponding dark data were subtracted from the X-ray illuminated data. Solvent backgrounds were obtained and subtracted from the corrected X-ray illuminated data, and the scattering intensity at given radius was averaged concentrically to yield a scattering trace of intensity vs. scattering vector (q).

3.2.4 Film morphology measurements

Grazing incidence X-ray scattering (GIXS) was performed at Beamline 8ID-E at the Advanced Photon Source (APS) of Argonne National Laboratory. Thin films of the active layer were spun-cast on acetone-cleaned silicon substrates using the same conditions for OPV device fabrication. Thin films were illuminated by the 8-keV X-ray beam at an incidence angle of 0.2° for 10-20 seconds. Data were collected on a 2D Pilatus detector located 204 mm or 1450 mm from the sample for wide-angle and small-angle X-ray scattering, respectively. The location and magnitude of the scattered X-ray beam is described by scattering vector q, which is inversely related to crystalline inter-planar distances, d, by $q = 2\pi/d$. The background scattering was fit to an exponential decay and subtracted from the data trace for clarity. Line-cuts describing the in-plane and approximate the out-of-plane structure in the film were taken and fit to multiple Gaussians to obtain peak locations and widths.

Atomic force microscopy (AFM) and transmission electron microscopy (TEM) samples were prepared following identical conditions as the actual devices, but TEM samples were drop-cast on PEDOT:PSS coated glass slides. After drying, the substrates were first transferred to DI

water and the floated films then transferred to lacey carbon grids (Ted Pella, Inc.). TEM images were obtained on JOEL JEM-2100 TEM. AFM measurements were performed on a Dimension Icon Scanning Probe Microscope (Veeco) in tapping mode.

3.2.5 Transient optical absorption spectroscopy

Femtosecond transient absorption (fs TA) measurements were performed with an apparatus based on an amplified Ti−Sapphire laser system (Spitfire Pro XP). Here a 10 kHz, amplified 830 nm beam with energy of 3 mJ was generated by a Spitfire Pro XP regenerative amplifier (Spectra Physics Lasers). The Spitfire Pro XP was pumped by an Empower Nd:YLF laser (Spectra Physics Lasers) with a seed beam generated by a Mai Tai Ti:sapphire oscillator (Spectra Physics Lasers). Most of the 830 nm amplifier output is used to run a home-built, white light-seeded OPA to create the pump beam while a small percentage of the 830 nm amplifier output is used to create the white light probe. The white light probe was generated in the Helios (Ultrafast Systems) by focusing on a thin disk of sapphire for visible detection or an IR crystal. The pump wavelength was tuned to 540-580 nm with an energy of 20 μW and chopped at 500 Hz to generate the difference spectrum. At the sample, the pump beam was focused to 100 μm diameter with an instrument response function of 240 fs, yielding a fluence of 30 $\mu J/cm^2$. The white light probe was dispersed onto a CCD camera with an integration time of 3 sec per spectrum. Experiments were conducted at 25°C under an N_2 flow. Typically 5 - 6 to scans were averaged and samples were moved between scans to minimize photodegradation.

Single wavelength kinetic traces in the 5 ns– 80 μs range were also recorded. Samples were pumped at 540 nm using the output of an optical parametric oscillator pumped with the third harmonic of a NdYAG laser (Surelite-II, Continuum). The pump pulse width was

approximately 5 ns. Single wavelength kinetic traces were probed using a single wavelength 1070 nm LED operated in pulsed mode with a 0.1% duty cycle and a 200 ps pulse width (Thor labs). Spectra were detected by a biased InGaAs PIN diode (ET-3040) from Electro-Optic Technology. The diode output was digitized with a Picoscope 4227 (250 Ms/s sampling rate, 12-bit).

3.3 Results

Based on the observed variation in OPV performance with 0.0 – 5.0 vol% DIO solvent additive, we focus on understanding those factors underlying performance variations through studies of the active layer solution and thin film morphology using X-ray scattering, AFM, and TEM, as well as correlations of morphology with exciton generation and charge transport dynamics, measured with optical fs and ns transient absorption spectroscopy. It will be seen that DIO addition reduces the $PC_{71}BM$ solution aggregate size, promoting the formation of interpenetrating donor and $PC_{71}BM$ BHJ domains, leading to larger initial PBTIBDT cation populations. However, the resulting variations in $PC_{71}BM$ interconnectivity have a major impact on the resulting solar cell performance.

3.3.1 Solar cell performance

PBTIBDT:$PC_{71}BM$ solar cells were fabricated using 0.0 – 5.0 vol% DIO solvent additive in the active layer solution prior to spin-coating (Figure 3.2). The highest PCE of 5.36% is achieved using 3.0 vol% DIO with V_{oc} = 0.959 V, J_{sc} = 8.87 mA/cm^2, and FF = 65.7% (Table 3.1). Devices fabricated with 2 vol% DIO exhibit slightly lower PCEs (5.27%) attributed primarily to decreased J_{sc} of 8.38 mA/cm^2. Cells processed without DIO afford the lowest PCE = 2.82% with both the J_{sc} = 6.00 mA/cm^2 and FF = 51.8% depressed.

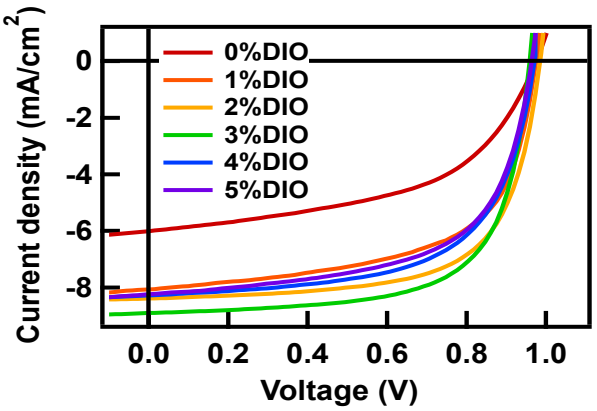

Figure 3.2. *J-V* response of PBTIBDT: $PC_{71}BM$ solar cells with varying concentrations of DIO in the *o*-dichlorobenzene film casting solution

Table 3.1. Performance metrics of PBTIBDT:$PC_{71}BM$ solar cells fabricated with varying concentrations of DIO in the *o*-dichlorobenzene film casting solution

[DIO] (%)	V_{oc} (V)	J_{sc} (mA/cm^2)	*FF* (%)	PCE_{max} (%)	PCE_{avg} (%)[a]
0	0.973	6.00	51.8	3.03	2.82
1	0.973	8.06	60.6	4.75	4.59
2	0.987	8.38	65.2	5.48	5.27
3	0.959	8.87	65.7	5.59	5.36
4	0.973	8.28	61.9	4.99	4.81
5	0.959	8.23	61.2	4.83	4.56

[a]Measured over 8-10 devices.

3.3.2 Aggregate dimensions in solution

To understand the origin of the BHJ thin film morphology differences, the aggregation properties of PBTIBDT and $PC_{71}BM$ (if any) in *o*-dichlorobenzene with 0.0 – 5.0 vol% DIO were analyzed by small angle X-ray scattering (SAXS). Data were fit using a Unified fit procedure[93, 94, 129] in which the scattering signal trace is simultaneously fit using Guinier and Porod models for small spherical non-interacting particles in a uniform matrix. The particle radius of gyration (R_g) is determined by the location and bend in the "Guinier knee," while the slope after the knee, the Porod region, is characteristic of the particle surface texture and dimensionality.[214]

The PBTIBDT solution traces exhibit a fall in intensity as a function of the scattering factor Q from $Q = 0.007$ Å^{-1} with a slight Guinier knee in the trace around $Q = 0.007 – 0.03$ Å^{-1} for all samples, and a second knee at 0.03 – 0.07 Å^{-1} (Figure 3.3A) indicating the presence of two types of PBTIBDT aggregates. Fitting the low Q Guinier knee reveals that this first population of PBTIBDT aggregates with 1.0 – 5.0 vol% DIO have a R_{g1} of 49.1 ± 1.2 Å to 43.5 ± 0.9 while PBTIBDT with no DIO has an $R_{g1} = 78 \pm 3.5$ Å (Table 2). The second Guinier knee yields R_{g2} values of 9.3 Å – 10.8 Å with no trend in R_{g2} with vol % added DIO. This large initial decrease in R_{g1} aggregate size was not present in the previously studied PTB7 system (Figure 3.1)[193], but is likely attributable here to solubilization by the side chain substituents of loosely bound PBTIBDT aggregates which would exhibit tighter packing in neat ODCB.[179] Unlike PTB7, the large branched 2-hexyldecyl and *n*-dodecyl side chains of PBTIBDT may contribute to the early solubility on incremental DIO addition. The slight fall in PBTIBDT R_{g1} with a 1.0 to 5.0 vol% DIO increase suggests the continued DIO interaction with loosely aggregated PBTIBDT segments while the constant size of the PBTIBDT R_{g2} aggregates suggests that they may be more strongly aggregated than the R_{g1} aggregate distribution.

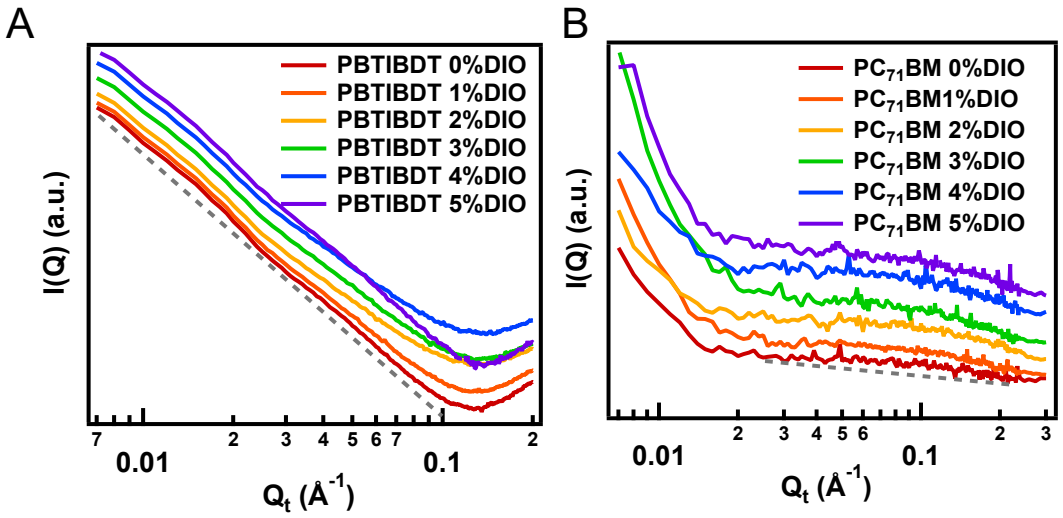

Figure 3.3. Solution phase small angle X-ray scattering traces of, (A) PBTIBDT and (B) $PC_{71}BM$ in *o*-dichlorobenzene solution with 0.0 – 5.0% DIO used to estimate aggregate size. Straight gray dotted lines provide visual guidance to peak locations and traces are offset for clarity.

Table 3.2. Solution phase radii of gyration (R_g) of neat PBTIBDT and $PC_{71}BM$ aggregates in *o*-dichlorobenzene with 0.0 – 5.0 % DIO obtained from SAXS measurements. Quantities in parentheses denote estimated uncertainties form the Unified fitting procedure.

[DIO] (%)	**PBTIBDT R_{g1} (Å)**	**PBTIBDT R_{g2} (Å)**	**$PC_{71}BM$ R_g (Å)**
0	78.0 (3.5)	10.6 (0.8)	17.0 (2.0)
1	49.1 (1.2)	10.8 (0.2)	15.9 (2.2)
2	46.1 (1.1)	10.7 (0.6)	11.9 (1.6)
3	45.9 (1.0)	10.6 (0.2)	8.8 (0.7)
4	45.9 (1.1)	10.4 (0.2)	10.0 (1.1)
5	43.5 (0.9)	9.3 (0.7)	11.6 (1.0)

The neat $PC_{71}BM$ traces in *o*-dichlorobenzene exhibit an initial sharp drop in intensity from Q = 0.007 to 0.02 Å followed by a slightly visible Guinier knee (Figure 3.3B). The DIO concentration dependence of the $PC_{71}BM$ aggregate size is evident from the decrease of the slope of the scattering intensity $I(Q)$ vs. Q, as well as the Q value as a function of the DIO concentration. Indeed, a decrease in $PC_{71}BM$ R_g from 17.0 ± 2.0 Å to 8.8 ± 0.7 Å for 0.0 – 3.0 vol% DIO and then an unexpected rise in $PC_{71}BM$ R_g to 11.6 Å with 5.0 vol% DIO (Table 3.2) is observed. Since R_g = 8.8 Å corresponds to 1-2 $PC_{71}BM$ molecules, it is conceivable that after fully solubilizing all of the $PC_{71}BM$ molecules, the solubilized $PC_{71}BM$ molecules begin to re-aggregate inside DIO-rich solvation domains as the DIO concentration increases further. Fits of the PBTIBDT: $PC_{71}BM$ blend solutions yield similar domain sizes, and traces can also be fit using a linear combination of neat PBTIBDT and $PC_{71}BM$ traces, indicating that the PBTIBDT and $PC_{71}BM$ aggregates are not strongly interacting.

3.3.3 Crystal structure and domain size in thin films

TEM images of films spun-cast from *o*-dichlorobenzene solutions with zero and 1.0 vol% DIO exhibit large dark domains (~80 nm) distributed in a matrix of lighter colored domains (Figure 3.4). Using energy dispersive X-ray spectroscopy (EDS), it can be determined that the darker regions have higher concentrations of $PC_{71}BM$. As the concentration of DIO is increased to 2.0 – 5.0 vol%, mixed film morphologies are observed in which the $PC_{71}BM$ appears to be evenly dispersed throughout the film. However, TEM can only provide a relative contrast indicative of discrete domains, and shows no obvious morphology differences between the 2.0 – 5.0 vol% DIO films.

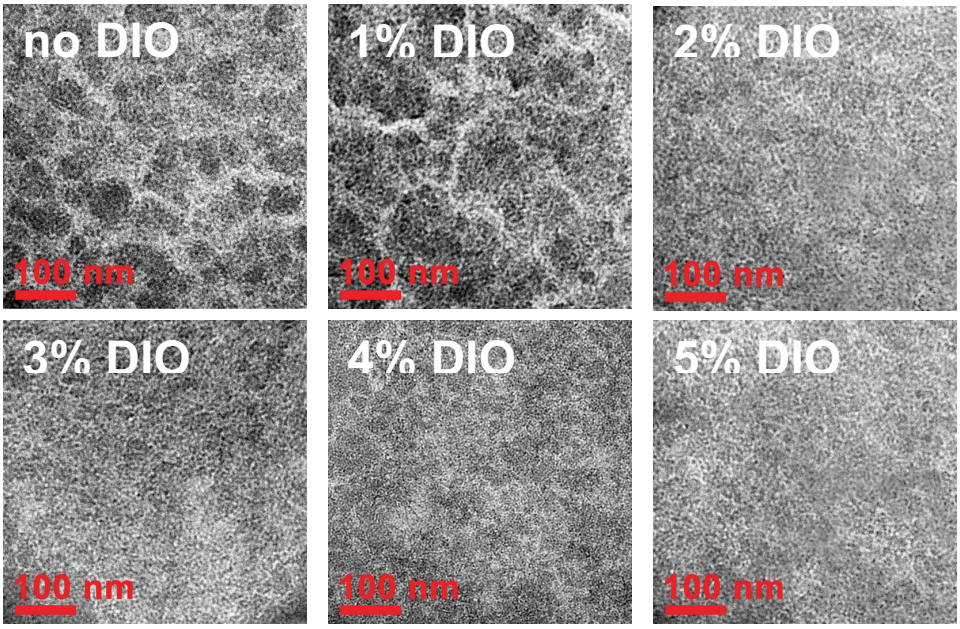

Figure 3.4. TEM images of PBTIBDT: $PC_{71}BM$ blend films cast from *o*-dichlorobenzene with 0.0-5.0 vol% DIO. The darker regions have higher $PC_{71}BM$ concentrations.

Grazing incidence X-ray scattering was next used as a complement to TEM for characterizing the film PBTIBDT packing and domain sizes. From grazing incidence wide-angle X-ray scattering (GIWAXS), the crystalline inter-chain π-stacking distances and lamellar *d*-spacings as well as crystalline correlation lengths for neat PBTIBDT films, neat $PC_{71}BM$, and PBTIBDT: $PC_{71}BM$ blend films with 0.0 – 5.0 vol% DIO can be determined (Figure 3.5A). The average lamellar *d*-spacing determined by the *q* values of the scattering feature corresponding to PBTIBDT side chains is 27.4 ± 0.8 Å in the neat film and falls slightly to 25.4 ± 0.3 Å in the blend film. The lamellar scattering reflection is isotropic, but is more intense in the in-plane scattering orientation, indicating that the polymer is largely "π-face-down" with the π-conjugated backbone parallel to the substrate. The PBTIBDT π-π stacking distance determined by the feature at q_z = 1.75 $Å^{-1}$ is consistently 3.6 Å in the neat and blend films. Since the π-π stacking reflection appears more strongly in the out-of-plane scattering, this confirms that the ordered portion of the polymer, most likely to be near the interface with the electrode surface, has a π-face-down orientation on the substrate. All lamellar *d*-spacings in the neat and blend films are within a 5% margin of error, so it is concluded that DIO addition has a negligible effect on the PBTIBDT packing (see Appendix A). In neat and blend films and at all concentrations of added DIO, $PC_{71}BM$ exhibits an isotropic ring at q_z = 1.4 $Å^{-1}$ corresponding to a *d*-spacing of 4.5 Å.

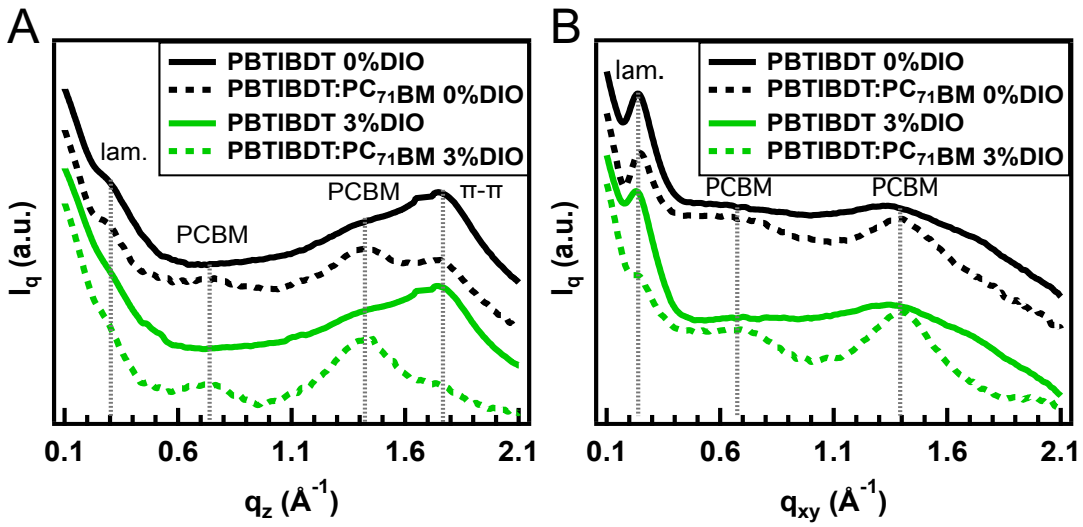

Figure 3.5. Morphology and crystal structures of neat and blend PBTIBDT films cast from *o*-dichlorobenzene with 0.0 and 3.0 vol% DIO as described by GIWAXS line-cuts in the, (A) out-of-plane orientation and (B) in-plane orientation describing the crystal structure and crystalline correlation lengths

Using a modified Scherrer analysis,[91] trends in crystalline correlation length along a given diffraction plane can be extracted. The basic Scherrer equation $D_{hkl}=2\pi K/\Delta d_{hkl}$ relates the correlation length of a given diffraction peak, D_{hkl}, to the full width half-maximum of the diffraction peak, d_{hkl}. K is a constant related to the crystalline domain shape and the commonly accepted K = 0.9 for spherical polymer crystalline domains[91] was used here. Note that the Scherrer analysis does not account for peak broadening due to crystalline disorder, so it estimates a minimum crystalline correlation length, and it is reasonably assumed that the internal disorder within the crystal remains the same for all PBTIBDT and $PC_{71}BM$ films.

In neat PBTIBDT films, the lamellar crystalline correlation length decreases from 7.9 nm to 6.2 nm as the DIO concentration is increased, mirroring the trend seen in the solution SAXS results (Table 3.3). A similar decrease is not evident in the blend PBTIBDT:$PC_{71}BM$ films, and the domain sizes vary from 5.9 – 8.9 nm, averaging 7.6 nm with no apparent correlation with DIO vol%. There is no significant change in the π-π stacking correlation length which is 3.3 nm in the neat film. We were not able to confidently determine the correlation length in the blend film due to the overlap of the $PC_{71}BM$ ring and π-π stacking peaks.

Neat $PC_{71}BM$ films were also examined by GIWAXS as a function of added DIO. The *d*-spacing remains constant in the neat and blend films, indicating that DIO does not significantly affect the $PC_{71}BM$ packing (see Appendix A). Interestingly, the films exhibit no consistent change in crystalline correlation length with different DIO concentrations in the neat (2.6 – 3.9 nm) or blend (2.8 – 3.1 nm) films, but generally the PCBM domain size decreases by ~ 0.5 nm from the neat to blend film for a given vol% DIO.

Table 3.3. Thin film domain sizes calculated by a Guinier fit to the GISAXS data, and crystalline correlation lengths calculated by Scherrer analysis of GIWAXS data. Errors in fit given in parentheses.

[DIO] (%)	Crystalline correlation length (nm)					Domain size (nm)	
	PBTIBDT			$PC_{71}BM$			
	lam. (neat)	lam. (blend)	π-π (neat)	neat	blend	PBTIBDT	$PC_{71}BM$
0	7.9 (0.1)	7.7 (0.1)	3.0 (0.0)	3.3 (0.2)	2.8 (0.0)	21.7 (3.9)	4.5 (0.4)
1	7.0 (0.2)	7.1 (0.1)	3.1 (0.0)	3.6 (0.1)	3.1 (0.4)	14.8 (2.2)	7.8 (0.9)
2	8.0 (0.1)	7.2 (0.3)	3.3 (0.3)	2.6 (0.0)	3.1 (0.2)	14.6 (4.2)	5.2 (2.2)
3	6.7 (0.2)	5.9 (0.1)	3.2 (0.0)	3.3 (0.0)	2.8 (0.0)	14.6 (6.6)	5.9 (0.7)
4	6.6 (0.1)	8.9 (0.3)	2.9 (0.0)	4.0 (0.2)	3.0 (0.1)	16.5 (7.2)	5.8 (1.4)
5	6.2 (0.1)	7.1 (0.2)	3.2 (0.0)	3.5 (0.4)	2.8 (0.3)	14.3 (5.1)	5.7 (1.9)

The grazing incidence small angle X-ray scattering (GISAXS) domain size measurement is sensitive to electron density differences, and therefore is used to determine the size of both amorphous and crystalline domains in a given material. Importantly, GISAXS measurements complement the Scherrer analysis from the above GIWAXS data analysis which estimates the size of only the crystalline domains. Because GISAXS depends on electron density contrast, we are only able to measure the domain sizes in the blend films, and the GISAXS traces were fit to two particle size distributions which can be related to the $PC_{71}BM$ and PBTIBDT domains based on the crystalline correlation lengths and solution SAXS measurements of aggregate sizes (Figure 3.6). From these data, it is only possible to determine that the larger domains are predominately BTIBDT since they exhibit a different electron density than the mixed phase and pure/predominantly PCBM regions of the film.

The radius of gyration (R_g) was determined using the same Unified fitting procedures as for the solution SAXS.[93, 94, 129] As expected, the domain sizes measured by GISAXS are consistently larger than those derived from the Scherrer analysis because the GISAXS domain size includes non-crystalline regions. The initial decrease in PBTIBDT GISAXS domain size from 21.7 nm to 14.8 nm upon 1.0 vol% DIO addition mirrors the decrease in aggregate radius seen in the solution phase SAXS measurements. This decrease is indicative of the formation of denser PBTIBDT domains due to increased side chain organization and/or expulsion of included $PC_{71}BM$ molecules. A slight increase in $PC_{71}BM$ domain size is observed on 1.0 vol% DIO addition, suggesting that DIO addition promotes the formation of purer PBTIBDT domains and a concurrent increase in the size of the pure $PC_{71}BM$ domains. However, the $PC_{71}BM$ domain size is essentially unchanged for 2.0 – 5.0 vol% DIO at ~5.7 nm, indicating that the PBTIBDT domain purity is constant for films with 1.0 – 5.0 vol% DIO.

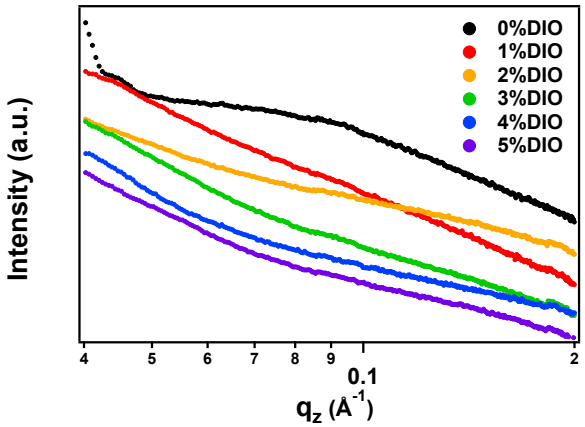

Figure 3.6. GISAXS linecuts of PBTIBDT:PCBM blend films with 0-5 vol% DIO describing the domain sizes out of plane

3.3.4 Exciton and charge generation/transport dynamics by optical transient absorption spectroscopy

Although it is well-known that the BHJ film morphology affects the OPV performance metrics, it is not clear how the film morphology in the present system affects the exciton splitting dynamics and yields. Optical transient absorption (TA) spectroscopy on both ultrafast (0 – 3 ns) and longer (5 ns to 20 μs) time scales enables monitoring of the time-dependent populations of various intermediate species, such as the exciton (EX) and charge-separated (CS) states, as well as the ground state bleach/recovery (GSB) following light absorption.[215, 216] From these measurements, the charge-separated state populations and charge-separation/recombination kinetics can be extracted.[217] We focus here on the near-infrared (NIR) spectral region, where these intermediate states absorb after being created by photoexcitation at 630 nm, the peak absorption of the polymer (Figure 3.7). In this system, the CS state spectral signature is represented by the TA spectral signal of the polymer cation (CAT), obtained independently from spectroelectrochemical measurements (Figure 3.8).

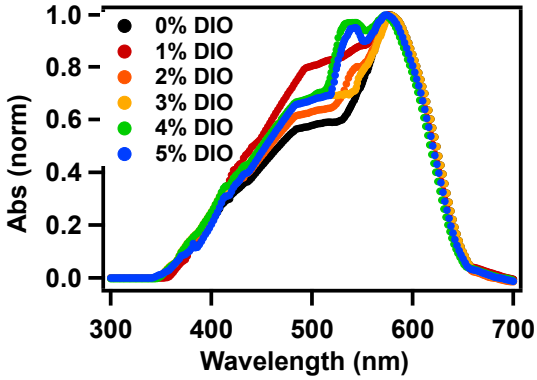

Figure 3.7. Optical absorption spectra of neat PBTIBDT films with no DIO and 1-5 vol% DIO

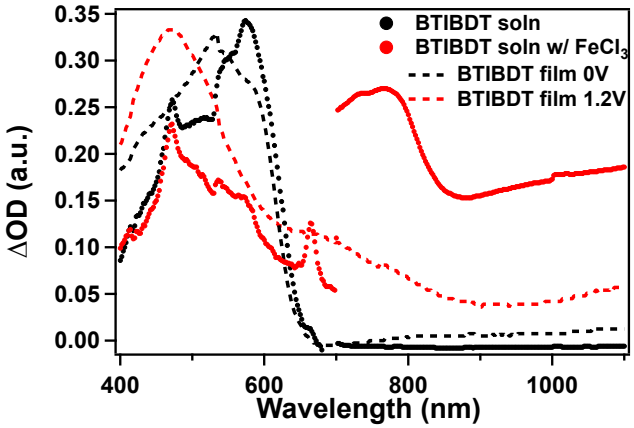

Figure 3.8. Spectroelectrochemisty spectra of PBTIBDT solutions in *o*-dichlorobenzene and neat film showing cation signals at 750-800 nm with a broad feature extending from 1000 nm to longer wavelengths

NIR and visible fs TA was performed on dilute air-free PBTIBDT solutions in *o*-dichlorobenzene to first determine the EX signal location and the intrinsic EX decay dynamics in the absence of the $PC_{71}BM$ acceptor. The solution NIR TA spectra at a delay time of 1 ps exhibit a broad signal spanning 1000-1400 nm (Figure 3.9A). Although these TA features are very broad due to the BHJ film inhomogeneous local environment and structural diversity, the central positions of the different species can be confidently assigned by scrutinizing the TA spectral evolution with the delay time. By capturing the earliest delay time TA spectra of the polymer in solution and in the neat films, the EX spectral feature centered around 1040 nm can be assigned because it is the feature emerged at the earliest when the CAT still has a very low concentration. The CAT spectral feature is assigned to the peak centered around 1180 nm, based on the results from spectroelectrochemistry (Figure 3.8). The delay time dependent EX peak intensity was next used to extract the solution phase exciton dynamics of PBTIBDT, which were later used references to determine the thin film exciton dynamics. The fitting was carried out by dual Gaussian functions centered at each delay time, and the integrated area under the Gaussian function as a function of delay time was used to extract the kinetics for both EX and CAT. The CAT formation in solution phase for the charge transfer polymers have been observed in PTB7, which was attributed to polymer self-folding/aggregation where the inter-segment within a polymer chain facilitate the CS state formation without the presence of the acceptor at much lower yields.[218]

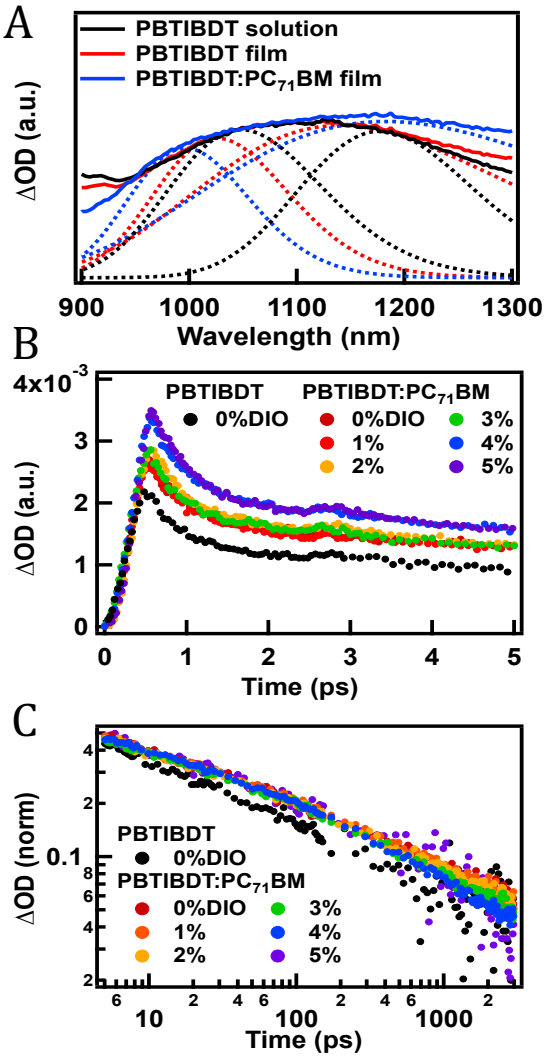

Figure 3.9. Transient absorption spectra of (A) PBTIBDT solution in *o*-dichlorobenzene, PBTIBDT neat film with 0.0 vol% DIO, and PBTIBDT: $PC_{71}BM$ film with 3.0 vol% DIO at 1 ps after excitation, showing the underlying exciton and cation peaks at λ = 1000−1040 nm and 1180 nm, respectively, (B) initial cation population and decay normalized to the ground state bleach signal amplitudes, (C) decay of the cation peak at 1180 nm with different DIO concentrations

NIR transient absorption spectra at 1 ps time delay of the neat PBTIBDT films with 0.0, 3.0, and 5.0 vol% DIO, and of PBTIBDT: $PC_{71}BM$ blend films with 0.0 – 5.0 vol% DIO exhibit a broad feature encompassing two peaks, locations and widths of which were determined from a Gaussian multi-peak fit (Figure 3.9A).[99] This analysis reveals two peaks: a broad peak centered ~1140 nm (neat films) or ~1180 nm (blend films) and a narrower feature centered at ~1000 nm for both the neat and blend films. From thin film spectroelectrochemistry, the cation absorption feature in PBTIBDT films is a broad peak extending from 950 nm into the NIR. The previously observed lack of a red-shift in the PBTIBDT ground state absorption from solution to films indicates that the polymer is significantly aggregated in ODCB solution, so similarity in EX peak location from solution to thin films is expected. Therefore, the narrow peak at 1000 nm is assigned to EX absorption and the broad feature at 1140/1180 nm to CAT absorption. The increase in intensity of the 1180 nm peak with $PC_{71}BM$ addition further supports the 1180 nm peak assignment to the cation. Kinetic traces at 1180 nm were normalized with respect to the ground state bleach intensity at 1 ps and show that the initial cation population is highest for blend films processed with 4.0 – 5.0 vol% DIO and 25% lower for films processed with 0.0 – 3.0 vol% DIO (Figure 3.9B). As expected, neat PBTIBDT film exhibits the smallest initial cation population.

Despite the variation in normalized initial CAT population at different DIO concentrations, the CAT decay kinetics of the neat PBTIBDT films remain invariant, so the CAT dynamics of the 0.0 vol% DIO film are used here as the PBTIBDT standard for later comparisons. The EX and CAT signals (Figure 3.9C) were fit using a sum of three exponential decay functions while the recovery of the GSB signal in the visible region was fit using a sum of

four exponential rise functions (recovery). The EX signal exhibits three lifetimes: 1) <1ps (τ_1) attributed to ultrafast exciton splitting and any possible exciton-exciton annihilation process; 2) 4 ps (τ_2) attributed to internal conversion because the ground state recovery kinetics also show a corresponding time constant, and 3) >3 ns (τ_4) accounting for a small portion (6%) of the long-lived exciton population. The kinetics of the CAT peak exhibit a ~100 ps decay (τ_3) due to charge recombination and a long lived cation species (τ_4) which can only be determined using ns flash photolysis as shown below (Table 3.4). Because of the global fitting procedure used, τ_2 is only observed in the EX decay while τ_1 is attributed to EX-CAT or CAT-CAT annihilation arising from the high pump power used (see Appendix A for all dynamics). The GSB kinetics show rise times corresponding to the EX decay (τ_2 = 4 ps) and CAT decay (τ_3 = 100 ps) as well as a long-lived GSB signal due to processes with long (>3 ns) time constants, such as triplet exciton decay, free carrier generation, etc.[219]

Table 3.4. Fitting parameters of PBTIBDT: $PC_{71}BM$ cation signal at 1180 nm showing decay rates (τ) and relative fractions (p^*) from the population remaining after 1 ps. The relative fractions (p) of the total and τ_1 are presented in the SI. τ_2 is only associated with the EX feature.

[DIO] (%)	τ_3 (ps)	p_3^* (%)	τ_4 (ps)	p_4^* (%)
0 (neat)	61 (10)	89 (8)	<3000	11 (4)
0	97 (8)	84 (4)	>3000	16 (2)
1	92 (10)	86 (5)	>3000	14 (2)
2	70 (10)	84 (5)	>3000	16 (2)
3	65 (11)	85 (6)	>3000	15 (3)
4	71 (5)	87 (2)	<3000	13 (1)
5	50 (8)	87 (4)	<3000	13 (2)

In the present data analyses, the three signals are globally fit using unified time constants, linking the ESA signal (τ_1), the exciton decay/GSB rise (τ_2), and the cation decay/GSB rise (τ_3) while the amplitudes of the decays are allowed to vary. A fourth exponential component with an apparent τ_4 ~3 ns was also included, but not linked for any component due to its uncertainty in the delay time window of the fs optical TA setup. Due to broadening of the CAT signal in the blend film, it was not possible to fit the EX decay with only the <1 ps, 4 ps, and >3 ns decay rates. Therefore, τ_3 is linked to the CAT decay in the global fitting procedure. Fitting parameters of the EX and GSB signals are provided in Appendix A.

The relevant cation decay rates and their corresponding relative fractions of the cation population (Table 3.4) indicate longer cation lifetimes in blend films than in the neat film. This is expected since the $PC_{71}BM$ can extract electrons from the polymer with a much larger driving force than the intrinsic polymer exciton splitting. Interestingly, as the DIO concentration is increased in the blend films, the charge recombination time constant characterized by τ_3 (Table 3.4) decreases from 97 ps to 50 ps with the largest difference between films with 1.0 and 2.0 vol% DIO, although the relative ratio to the long time constant is unchanged, 1:8-9. The long-lived cation lifetime (τ_4) is fit only approximately due to time window limitations, however films with 4.0 – 5.0 vol% DIO have shorter lifetimes (<3000 ps) and slightly smaller long-lived cation populations than films with 0.0 – 3.0 vol% DIO. To determine the longer lifetimes of the cation species, samples were studied using ns TA at a probe wavelength of 1070 nm where the exciton intensity is minimized and the cation feature is still present.

Kinetic curves for the thin films at the 1070 nm probe wavelength at early times (5 – 200 ns) (Figure 3.10; Table 3.5) show a strong DIO concentration dependence in the total signal intensity, corresponding to the population of cation charge carriers while there are no significant changes in decay rate constants. This result indicates that the highest total intensity or the highest cation population is observed in films processed with 2.0 – 3.0 vol% DIO, however the signal intensities are ~30% lower with 0.0 – 1.0 vol% DIO and ~40% lower with 4.0 – 5.0 vol% DIO. Despite a smaller initial cation population observed at 1 ps for films with 2.0 – 3.0 vol% DIO (Figure 3.9B), at a 5 ns delay time they have the largest long-lived cation population. The kinetic traces were fit by a single exponential function, neglecting a long-lasting signal with <4% contribution.

[DIO] (%)	τ (ns)[a]
0 (neat)	65 (4)
0	56 (3)
1	53 (3)
2	54 (2)
3	44 (4)
4	64 (3)
5	62 (3)

Table 3.5. Fitting parameters for cation decay at 1070 nm for long time delays (5 ns – 20 μs).[a]Numbers in parentheses are estimated fitting uncertainties.

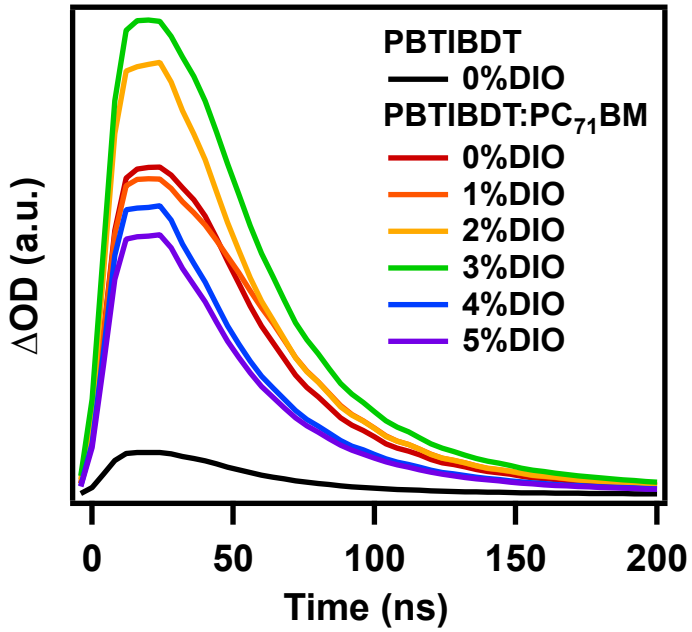

Figure 3.10. Long-lived cation populations in PBTIBDT and PBTIBDT: $PC_{71}BM$ thin films as measured by ns TA

3.4 Discussion

Based on results for 150 BHJ OPV systems reported in the literature, we recently argued that while the driving force for exciton splitting and the optical band gap correlate poorly with device PCE, both J_{sc} and *FF* correlate strongly with PCE and are influenced by the DIO used in active layer fabrication.[157] J_{sc} is a measure of charge collection efficiency resulting from multiple processes including light absorption, charge separation, and charge recombination,[132, 220] while *FF* is primarily a measure of carrier recombination;[79, 221] nevertheless both metrics are highly morphology-dependent. The present study provides detailed characterization and a direct link between active layer morphology and polymer cation kinetics and yields, demonstrating that charge separation and recombination are predominantly morphology-driven given the large driving force (0.6 eV) for exciton splitting in this system. The focus here is to elucidate the specific roles of DIO by assessing the correlations between film morphology, modulated by the different DIO concentrations, and the exciton and charge carrier dynamics at different stages of OPV function.

3.4.1 Influence of DIO on active layer morphology

From the solution X-ray analysis, a decrease in $PC_{71}BM$ aggregate size is observed on addition of 0.0 – 3.0 vol% DIO, followed by a slight increase at 4.0 – 5.0 vol% DIO, so it is noteworthy that no corresponding decrease and rise in film $PC_{71}BM$ domain size is observed over these two DIO concentration ranges. However, from the TEM images of the PBTIBDT:$PC_{71}BM$ blend films, a decrease in the size of the $PC_{71}BM$-rich regions is observed (Figure 3.4), indicating increased $PC_{71}BM$ dispersion throughout the film. Therefore, the

principal effect of DIO in this system is the dissolution of $PC_{71}BM$ aggregates in solution to enable the formation of a larger percentage of intermixed polymer + $PC_{71}BM$ networks as well as the formation of smaller pure $PC_{71}BM$ domains. This concurrent presence of range of mixed phases at length scales of < 50 nm is considered crucial to increase charge generation and decrease charge recombination and is linked to the increased *FF* and J_{sc}.[83, 194, 195, 199] Figure 3.11A presents a schematic of the PBTIBDT: $PC_{71}BM$ interfacial morphology with no DIO where there are large segregated PBTIBDT-rich and $PC_{71}BM$-rich domains, resulting in small PBTIBDT-$PC_{71}BM$ interfacial areas, but well-connected PBTIBDT and $PC_{71}BM$ charge percolation pathways. At the other extreme, PBTIBDT: $PC_{71}BM$ films with 5.0 vol% DIO form an interpenetrating texture at the interface resulting in high PBTIBDT-$PC_{71}BM$ interfacial area, but also leading to charge-trapping $PC_{71}BM$ islands (Figure 3.11C). However, films with 3.0 vol% DIO afford mixed textures, enhancing interfacial area versus films with no DIO, while maintaining charge percolation pathways through pure PBTIBDT and PCBM domains (Figure 3.11B). In addition, the small crystalline correlation length of PCBM and BTIBDT in the 3.0 vol% DIO thin film can mediate charge transport through the pure domains and mixed phase regions while the increasing purity of the BTIBDT domains measured by GISAXS enhances hole transport. Note that the 3.0 and 5.0 vol% DIO films also contain pure PBTIBDT and PCBM domains (not shown in the interfacial region of Figure 3.11) as evidenced by the X-ray scattering results in Table 3.3, but the focus here is on the donor-acceptor interface where charge generation and recombination occur.

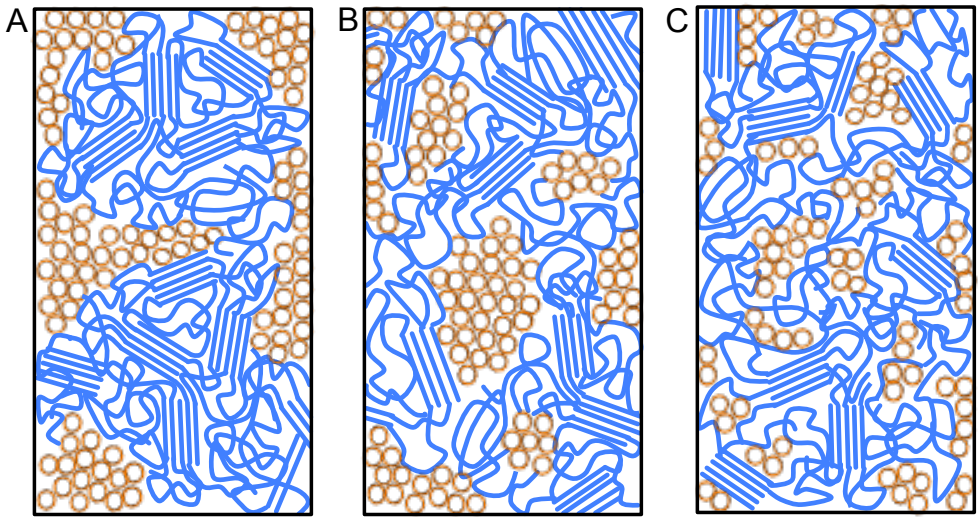

Figure 3.11. Schematic of the packing morphology of the *interfacial region* of PBTIBDT: $PC_{71}BM$ blend films processed with, A) no DIO, B) 3.0 vol% DIO, and C) 5.0 vol% DIO. PBTIBDT polymer chains are shown in blue and $PC_{71}BM$ molecules are shown in orange. As vol% DIO is increased, PBTIBDT domains become more loosely packed and $PC_{71}BM$ aggregate size decreases, allowing increased $PC_{71}BM$ intermixing.

3.4.2 Morphology-dependent dynamics of intermediate species

The effects of mixed phases and the resulting changes in interfacial area and percolation pathways in the thin films were investigated here by measuring the relative charge-separated state populations. The most striking observation is the DIO concentration dependence of the initial and long time CAT yields, and the lack of DIO concentration dependence on the time constants for the decays of the various intermediate species, a trend was also observed in PTB1:PCBM BHJ films (note: PTB1 was a derivative of PTB7 without F atoms).[126] These results are at first puzzling using models which associate long exciton splitting times with larger domain sizes.[205, 222] However, the present X-ray scattering results show that all domain sizes in the PBTIBDT: $PC_{71}BM$ blend films are rather small with dimensions of ~20 nm. This quantity can be somewhat misleading since the polymer packing is significantly disordered with the majority of structures invisible to X-ray diffraction. Therefore, in this particular polymer system, the insensitivity of the kinetics to the domain size suggests that the dominant exciton splitting takes place in interpenetrating small donor - acceptor boundary regions with negligible exciton diffusion. The sensitivity of the cation production yield to the domain size simply reflects donor-acceptor interfacial area changes as the domain sizes are adjusted by the amount of DIO present during film fabrication. The trend in the initial CAT population mirrors the increase in donor-accepter interfacial area as the concentration of DIO is increased. The initial CAT population after the exciton splitting is greatest for films processed with 4.0 – 5.0 vol% DIO, decreases ~25% for films with 1.0 – 3.0 vol% DIO, and decreases further for films having no DIO. As expected, neat PBTIBDT films exhibit the smallest initial cation population.

To determine how the initial PBTIBDT cation populations evolve over time scales longer than a few ns, the cation population surviving geminate charge recombination was measured. Ultimately, the cation and electron populations over the long timescale after exciton splitting are most likely responsible for the OPV J_{sc} and hence PCE. Note that PBTIBDT:$PC_{71}BM$ films processed with 2.0 – 3.0 vol% DIO exhibit larger cation populations than films with 0.0 – 1.0 vol% DIO, and films with 4.0 – 5.0 vol% DIO display the smallest cation population. Compared to the initial cation population increase, trends with DIO concentration on the ps timescale, the cation population on the ns - μs timescale differs and reflects the interplay between initial cation generation and cation transport away from interfacial recombination sites. Despite the formation of the largest CS population in the active layer at 1 ps delay for 4.0 – 5.0 vol% DIO concentration, the cation population that survives on the μs timescale is the lowest due to the small film $PC_{71}BM$ domain sizes and overmixing, leading to enhanced charge recombination. In contrast, the larger domain sizes in films with 0.0 – 1.0 vol% DIO suppress recombination and promote relatively larger, long-lived cation populations. In particular, the combination of a moderately large initial (1 ps) cation population for films with 2.0 – 3.0 vol% DIO and adequately separated domains, results in the largest long-lived cation populations in these PBTIBDT: $PC_{71}BM$ films. Since cations with longer lifetimes have a higher probability of charge collection, the larger long-lived cation population in the present films with 2.0 – 3.0 vol% DIO correlates with the relatively high observed J_{sc} and *FF* values.

Ade and coworkers previously linked the average purity of phases with <50 nm length scales with J_{sc} and *FF*. He found that films with a lower average purity at <50 nm lengths scales have increased *FF* and J_{sc}, attributed to improved charge transport mediation between the pure

and finely mixed phases.[195] In this investigation, we draw a similar comparison between $PC_{71}BM$ aggregate size in solution and the J_{sc} and *FF* in thin film (Figure 3.12). Since the $PC_{71}BM$ aggregate size in solution is shown to have no effect on the $PC_{71}BM$ domain size in thin films, we conclude that the primary contribution of DIO is to enhance mixing of the $PC_{71}BM$ in the film mixed phase regions. In the present BHJ system, J_{sc} is more strongly correlated with $PC_{71}BM$ solution aggregate size than *FF*. Since J_{sc} is dominated by charge generation while *FF* is primarily determined by recombination events, this suggests that the present solar cells without DIO are limited by low charge generation due to the small PBTIBDT-$PC_{71}BM$ interfacial area. With DIO addition, J_{sc} increases concurrent with an increase in the 1 ps initial cation population. This change in initial population is reasonably attributable to increased interfacial area formed by small $PC_{71}BM$ aggregates in solution which then penetrate into the polymer matrix, creating mixed phase regions. A similar increase in *FF* is observed for 0.0 – 3.0 vol% DIO, while a fall in *FF* is seen for 4.0 – 5.0 vol% DIO. The initial increase can be attributed to enhanced charge separation and transport due to the formation of smaller and more pure PBTIBDT and PCBM domains in the 0.0 – 3.0 vol% DIO regime, while films with 4.0 – 5.0 vol% DIO trend towards mixed phase morphologies, leading to $PC_{71}BM$ islands which trap charges and increase recombination. These results highlight the importance of using processing additives to balance donor-acceptor interfacial area and domain size to maximize charge separation and minimize recombination, thereby optimizing both J_{sc} and *FF*.

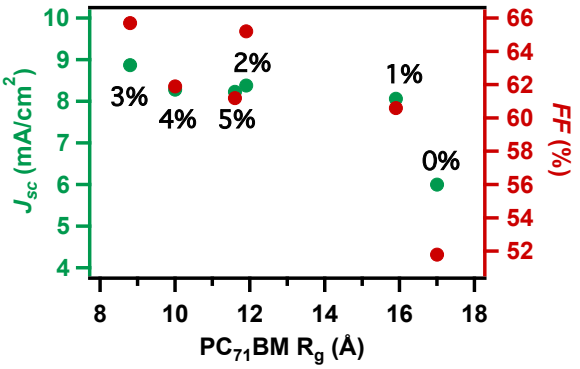

Figure 3.12. Increase in J_{sc} and *FF* as $PC_{71}BM$ solution aggregate size decreases with increasing vol% DIO

3.5 Conclusion

The effects of DIO on the PBTIBDT:$PC_{71}BM$ solar cell performance are investigated through morphology and exciton dynamics behaviors obtained respectively from X-ray scattering and optical transient absorption. We demonstrate that adding DIO to the active layer solution results in decreased $PC_{71}BM$ aggregate size, but only a slight decrease in donor polymer aggregate size, indicating that DIO selectively dissolves $PC_{71}BM$ and the loosely aggregated PBTIBDT polymer. However, smaller $PC_{71}BM$ aggregates are not observed in either the correlation length or domain size analyses, implying that these small $PC_{71}BM$ aggregates of essentially 1-2 $PC_{71}BM$ molecules do not affect the crystalline regions of the film and instead modify the amorphous mixed regions.

In this particular series of OPV active layer films, we show that DIO primarily affects the degree of mixing between the PBTIBDT polymer and $PC_{71}BM$ molecules. Within the domain size range for the donor polymer and acceptor $PC_{71}BM$, no significant DIO concentration dependence on the charge separate state decay kinetics is observed on the timescales from sub-ps to many ns. However, a strong DIO concentration dependence on the yield of the polymer cation population is observed over the same timescales, suggesting that increased mixed phase in the PBTIBDT:$PC_{71}BM$ films leads to increased initial cation population, but also enhanced charge recombination. The PBTIBDT:$PC_{71}BM$ solar cells with 3.0 vol% DIO exhibit the best balance between the initial charge generation yield and survival of the charge-separated species, and hence have the highest J_{sc} and *FF* in this series.

From this study it is learned that BHJ morphology can be a bottleneck to optimizing OPV performance and that the best performing devices result from optimal balance between the initial exciton splitting yield and minimization of wasteful charge recombination. Although DIO is only one processing additive among many, this study underscores its importance in the fundamental understanding of additive effects in different steps of OPV function.

Chapter 4. Systematic Evaluation of Structure-Property Relationships in Heteroacene-Diketopyrrolopyrrole Molecular Donors for Organic Solar Cells

4.1 Introduction

Recent advances in solution-processed small-molecule bulk-heterojunction organic photovoltaic (BHJ-OPV) cells prove their viability as a materials alternative to the more studied conjugated polymer OPV materials.[64, 65, 223-235] Unlike polymers, small molecules offer simpler syntheses and purification, inherent monodispersity, and fewer batch-to-batch properties variations. [57, 236, 237] Highly crystalline small molecules have been utilized extensively in vapor-deposited solar cells[238-242] and in thin film transistors, [243-248] establishing structure-property relationships with the goal of relating the molecular architecture and unit cell packing properties to charge transport and photovoltaic characteristics. In these systems, small-molecule morphologies differ from their polymeric counterparts in that small molecules stack in motifs that are unusual in polymers (e.g., columnar and herringbone) and are prone to form microcrystallites resulting in large grain boundaries in thin films. [249] Morphological differences between small-molecule and polymeric donors are expected to be similarly pronounced in the context of solution-processed bulk-heterojunction (BHJ) OPVs that consist of two-component blends, having a small-molecule *p*-type electron donor and an *n*-type electron acceptor. This makes it likely that morphological design rules inherited from polymer OPV studies will need to be revised in the context of small-molecule solar cells where crystallite formation and packing

structures are known to more strongly influence charge[250, 251] and energy[252, 253] transport processes. However, morphology design rules for small-molecule solar cells and the basic relationships between donor/acceptor mixing, domain size, stacking motifs, and OPV performance are still under examination.[250, 254-257] Here we investigate a series of closely related small-molecule donors with similar electronic properties that exhibit a diversity of stacking motifs and mixing behaviors when fabricated as OPVs. This series provides an opportunity to systematically probe the effect of molecular structure on crystal packing as well as BHJ morphology and photovoltaic response.

To achieve efficient OPV device performance, specific structural and morphological conditions must be met. First, the photogenerated exciton must be able reach a donor-acceptor interface before recombining, so it is generally accepted that the optimal donor domain size is ~10 nm,[18, 117, 258, 259] although some high-performing small-molecule solar cells exhibit domains of up to 20–30 nm.[2,43] Second, the charges resulting from exciton scission must be able to traverse their respective domains to the electrodes without recombining, so the domains must be electronically continuous and enable rapid charge transport. Here we use phenyl-C_{61}-butyric acid methyl ester (PCBM) as the *n*-type acceptor, recognizing that PCBM is generally capable of forming well-connected domains.[66] In polymers, the polymer backbone can facilitate charge transport to allow charges to move between neighboring donor domains.[139, 260-265] However, charge transport in small molecules is determined by the energetic coupling between neighboring molecules determined by the crystal structure[266, 267] and transport between neighboring crystallites is inefficient without appropriate relative orientations.[267-269] Furthermore, while polymer systems can tolerate low crystallinity and "mixed" donor/acceptor regions,[202, 270-274]

small-molecule blends generally require pure domains to achieve efficient charge transport.[255, 271, 275]

Aggregate properties such as domain size and mobility are determined in part by the molecular structure of the donor and acceptor, but that relationship is not easy to predict since it incorporates donor and acceptor crystal structures and intermolecular forces[276] as well as the interaction between the donor and the acceptor.[277] Nevertheless, it is generally accepted that more planar backbones allow tighter π–π stacking which can lead to increased charge mobility and an extended π-conjugated network, reducing the bandgap and therefore red-shifting the optical absorption.[278-280] Most small molecules for solution-processed solar cells incorporate a wide range of aromatic subunits in their backbone.[57, 236, 281-285] Large fused subunits enhance molecular planarity,[281, 286, 287] but may lead to decreased solubility[286] and decreased miscibility with PCBM,[286] affording large phase-segregated domains.[281] Linear subunits are most commonly used, but decreasing the aspect ratio by using non-linear subunits in which the π-conjugated network is expanded in two-dimensions[287-289] has been shown to enhance crystallinity, improve π-orbital co-facial overlap, and subsequently increase the hole mobility.[287, 290] In addition, increasing or decreasing the size of heteroatoms in the aromatic system can yield more planar backbones in polymers[154] and small molecules,[293-295] due to reduced steric interactions with neighboring subunits[295, 296] or with the solubilizing alkyl side chains.[292, 297]

Alkyl side chains appended to the central subunit are also known to impact the crystal structure while having little or no effect on molecular optoelectronic properties in solution.[59, 272, 273, 298-306] Branched side chains are frequently used to enhance the solubility of these high molecular weight small molecules.[257, 307] However, it has been demonstrated that steric

interactions due to branched alkyl side chains can induce backbone distortion in polymers[308-310] and small molecules, [300] resulting in loosely packed crystals with increased π–π stacking distances[301] and decreased co-facial overlap of neighboring π-conjugated backbones.[300] Furthermore, the position and number of the side chains can affect the crystal structure[269, 302-304] and donor miscibility with PCBM. [59, 272, 273, 279, 303, 305] We[311] and others[302, 312] have noted that side chains on the central subunit oriented towards each other generally increase lamellar spacing in polymer crystals[311, 313] and decrease backbone planarity,[312] while Fitzner, et al. showed that decreasing small-molecule side chain density results in increased π-π orbital overlap and larger phase-segregated domains with PCBM. [305]

In this contribution, we investigate and analyze fundamental structure-property relationships in a series of small molecules composed of heterocyclic acene electron-donating (D) cores flanked by thiophene-capped diketopyrrolopyrrole (TDPP) electron-accepting (A) moieties. Five molecular systems are discussed (Scheme 4.1): i) an asymmetric **BDTTDPP** (**aBDT**) molecule consisting of a benzodithiophene (BDT) electron-donating core with a single TDPP electron-accepting unit; ii) a symmetric **BDT(TDPP)$_2$** (**BDT**) molecule where the BDT core is flanked by two TDPP units; iii) **BDF(TDPP)$_2$** (**BDF**) where the BDT core is replaced by a benzodifuran (BDF) unit; iv) **NDT(TDPP)$_2$** (**NDT**) in which the π-conjugated core is expanded to two naphthodithiophene (NDT) units; and v) **zNDT(TDPP)$_2$** (**zNDT**) where the linear NDT core is replaced by the "zig-zag" NDT (zNDT) structural isomer. Solar cell device performance has been previously published for **NDT**[314], **zNDT**[315] and **BDT**[316], but the focus of this work is the systematic investigation of structure-property relationships as a result of small variations in the molecular structures. These building blocks, particularly benzodithiophene and

diketopyrrolopyrrole, are widely utilized in high-efficiency small molecule donors.[317-322] By varying the D core, hence the small-molecule π-conjugation length and aspect ratio, incremental variations in the single crystal are achieved. Using the known crystal structures, density functional theory (DFT) calculations are next used to evaluate the influence of packing on the intermolecular couplings relevant to hole transport and also to calculate the relevant reorganization energies. We find that small variations in crystal structure have significant effects on small-molecule miscibility with PCBM, hole mobility in neat films, and the resulting OPV device performance. In particular, it is observed that in addition to having large out-of-plane mobility, the most successful donors in the series also form less crystalline films, but possess packing structures with large intermolecular couplings due to high π co-facial overlap. The results on this series reveal complementary requirements for successful small-molecule donors and suggest future directions for acene-based small molecule solar cells.

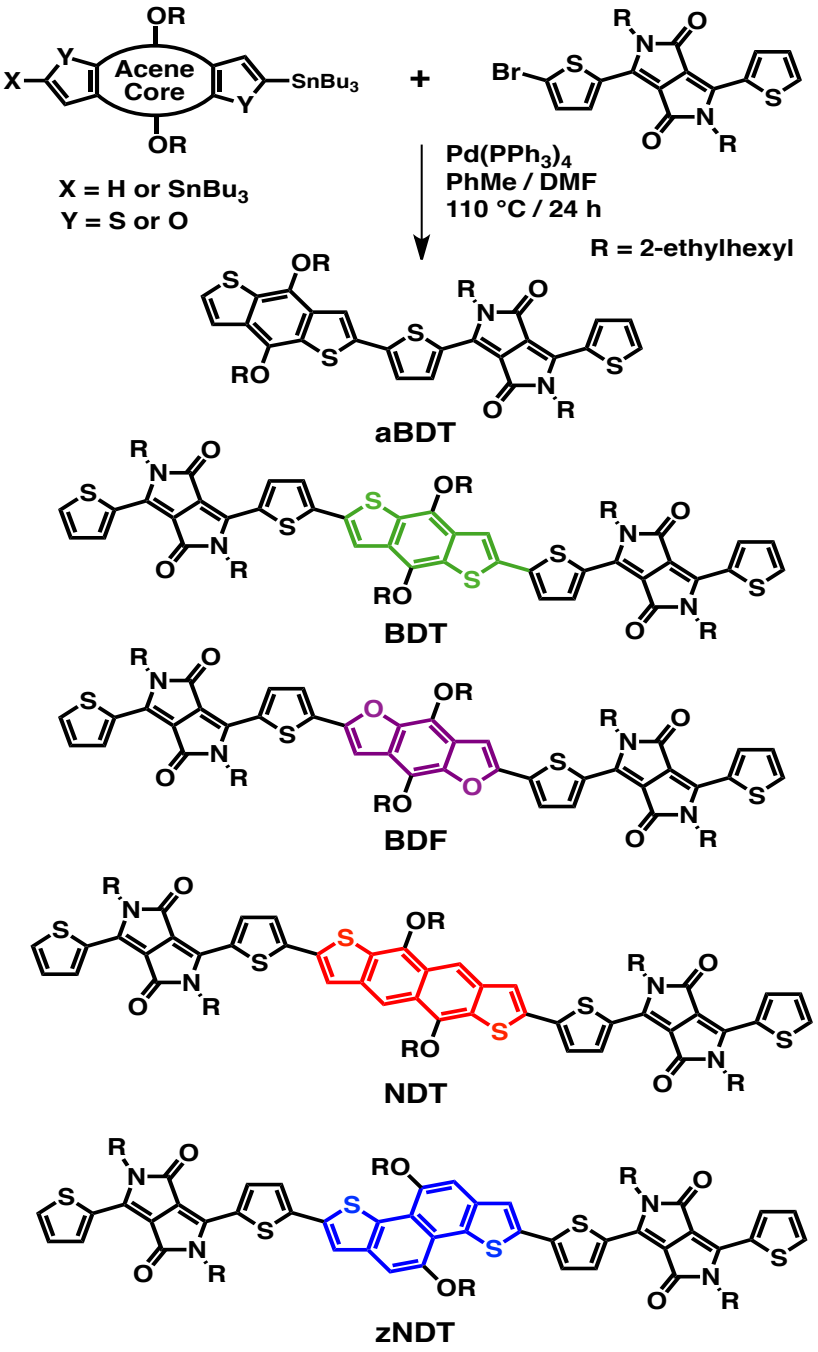

Scheme 4.1. Synthetic scheme and molecular structures of the series of heterocyclic acenes (in color) flanked by thiophene-capped DPP units where R = 2-ethylhexyl

4.2 Methods

4.2.1 Synthesis

The small-molecule donors were synthesized by Stille cross coupling of the appropriate stannylated heterocyclic acenes with TDPPBr in good yields (80%-91%) according to established methodologies (Scheme 4.1).[314, 315] Synthetic procedures for **BDT**, **NDT**, and **zNDT** have been previously published.[314-316] **BDF** was synthesized by adding $Pd(PPh_3)_4$ (85 mg, 74 μmol) to a degassed mixture of TDPPBr (702 mg, 1.16 mmol) and 1,5-bis(trimethylstannyl)-4,8-bis((2-ethylhexyl)oxy)benzo[1,2-*b*:4,5-*b′*]difuran (344 mg, 0.465 mmol) in 6:1 PhMe:DMF (7 mL) and heated to 110 °C under N_2 for 20 h. The solution was added to MeOH (100 mL) and the resulting precipitate was collected by filtration and chromatographed on SiO_2 (hexanes:$CHCl_3$ 1:2) to afford a dark purple solid. Recrystallization in $CHCl_3$ by slow vapor diffusion of EtOAc afforded **BDF** as tiny crystalline needles (426 mg, 63%). ^{1}H NMR ($CDCl_3$, 298 K, 500 MHz) δ = 9.05 (d, J = 4.0 Hz, 2H), 8.94 (d, *J* = 4.0 Hz, 2H), 7.65 (d, *J* = 5.0 Hz, 2H), 7.60 (d, *J* = 4.0 Hz, 2H), 7.29 (dd, *J* = 4.0, 5.0 Hz, 2H), 7.20 (s, 2H), 4.45 (d, *J* = 5.5 Hz, 4H), 4.13–4.02 (m, 8H), 1.96 (hep, *J* = 6.5 Hz, 2H), 1.89 (hep, *J* = 6.5 Hz, 2H), 1.83 (hep, *J* = 6.0 Hz, 2H), 1.72–1.48 (m, 8H), 1.46–1.23 (m, 40H), 1.05 (t, *J* = 7.5 Hz, 6H), 0.95 (t, *J* = 7.0 Hz, 6H), 0.94 (t, *J* = 7.5 Hz, 6H), 0.90 (t, *J* = 7.5 Hz, 6H), 0.88 (t, *J* = 7.0 Hz, 6H), 0.87 (t, *J* = 7.5 Hz, 6H). ^{13}C ($CDCl_3$, 298 K, 125 MHz) δ = 161.9, 161.8, 149.7, 142.3, 140.4, 139.8, 137.8, 136.8, 135.6, 131.1, 130.8, 130.0, 129.6, 128.6, 125.6, 122.3, 108.7, 108.3, 102.4, 75.9, 46.1, 46.1, 40.3, 39.3, 39.2, 30.5, 30.3, 29.3, 28.5, 28.5, 23.9, 23.7, 23.7, 23.3, 23.2, 14.4, 14.2, 14.2, 11.4, 10.6. HRMS (MMI-TOF-MS) *m/z* calcd for $C_{86}H_{115}N_4O_8S_4$ $[M + H]^+$: 1459.7593, found 1459.7637. Anal. Calcd for $C_{86}H_{114}N_4O_8S_4$: C, 70.74; H, 7.87; N, 3.84. Found: C, 70.97; H, 7.91; N, 3.80.

To synthesize **aBDT**, $Pd(PPh_3)_4$ (40 mg, 0.03 mmol) was added to a degassed solution of 1-trimethylstannyl-4,8-bis((2-ethylhexyl)oxy)benzo[1,2-*b*:4,5-*b'*]dithiophene (280 mg, 0.38 mmol) and TDPPBr (200 mg, 0.33 mmol) in 4:1 PhMe:DMF (3.5 mL) and heated to 110 °C for 16 h. The reaction mixture was next cooled to ambient temperature and poured into 25 mL MeOH. The resulting precipitate was then collected by vacuum filtration and chromatographed on silica (1:1 CH_2Cl_2:hexanes) to afford a purple solid (291 mg, 91%). ^{1}H NMR ($CDCl_3$, 500 MHz, 298 K) δ = 9.01 (d, J = 4.1 Hz, 1H), 8.93 (dd, J = 3.9, 1.2 Hz, 1H), 7.67 (s, 1H), 7.65 (dd, J = 4.9, 1.2 Hz, 1H), 7.48 (d, J = 5.5 Hz, 1H), 7.46 (d, J = 4.2 Hz, 1H), 7.41 (d, J = 5.5 Hz, 1H), 7.29 (d, J = 5.0, 3.9 Hz, 1H), 4.22 (d, J = 5.6 Hz, 2H), 4.19 (d, J = 5.5 Hz, 2H), 4.11–4.02 (m, 4H), 1.96 (hep, J = 6.7 Hz, 1H), 1.89 (hep, J = 6.7 Hz, 1H), 1.89–1.80 (m, 2H), 1.75–1.50 (m, 6H), 1.44–1.23 (m, 26H), 1.05 (t, J = 7.5 Hz, 3H), 1.04 (t, J = 7.5 Hz, 3H), 0.98–0.93 (m, 9H), 0.91–0.86 (m, 9H). 13C ($CDCl_3$, 125 MHz, 298K) δ = 161.7, 161.6, 145.0, 144.2, 142.6, 140.3, 139.7, 136.8, 135.4, 135.0, 132.5, 131.8, 130.6, 130.5, 129.8, 129.2, 129.0, 128.5, 126.6, 126.2, 120.4, 117.7, 108.4, 108.1, 76.2, 76.1, 45.9, 40.6, 40.6, 39.2, 39.1, 30.4, 30.4, 29.2, 28.4, 28.3, 23.8, 23.6, 23.5, 23.1, 23.1, 14.2, 14.1, 14.1, 11.3, 11.3, 10.5, 10.5. HRMS (ESI-TOF-MS): *m/z* calcd for $C_{56}H_{77}N_2O_4S_4$ $[M + H]^+$ 969.4761, found 969.4744.

4.2.2 Optical absorption spectroscopy

Optical spectra were acquired on a Varian Cary 5000 UV-Vis-NIR spectrophotometer. Serial dilution was performed for each sample to determine the molar extinction coefficients in chloroform solution. Active layers were spun-cast on glass slides from chloroform solution and film thicknesses were measured by profilometry with a Veeco Dektak 150 surface profilometer. The absorption coefficients in films were determined by scaling the absorption by film thickness.

4.2.3 Cyclic voltammetry (CV)

CV on the donor compounds was performed in CH_2Cl_2 solution at a concentration of 0.25 $mg \cdot mL^{-1}$ using 0.1 M NBu_4PF_6 as electrolyte (recrystallized from EtOH) on a Epsilon-C3 system (Bioanalytical Systems). The electrochemical cell was equipped with a Pt wire, Ag wire, and a glassy carbon (3 mm^2) electrode which were used as the counter electrode, the pseudo-reference, and working electrode, respectively. All scan rates were 100 $mV \cdot s^{-1}$ and the solutions were purged with CH_2Cl_2-saturated N_2 prior to use. Ferrocene was purified by sublimation for the ferrocene/ferrocenium (Fc/Fc^+) redox couple and was used as the internal standard, and assigned an energy level of -4.88 eV vs. vacuum.

4.2.4 Differential scanning calorimetry (DSC)

DSC data were collected on an In-calibrated Mettler-Toledo DSC822e instrument equipped with a TSO801RO autosampler. The samples (weight range 1.5 - 3.0 mg) were placed in lidded 30 μL Al pans and thermally cycled twice under N_2 with a heating rate of 10 °C per min and a slower cooling rate of 5 °C per min to minimize overcooling effects. The reported cycles correspond to the second cycle and are all plotted exotherm up/endotherm down.

4.2.5 Single crystal growth and characterization

Single crystals suitable for X-ray diffraction were grown by slow evaporation of anhydrous $CHCl_3$ solutions. Prior to crystal growth ~1 $mg \cdot mL^{-1}$ solutions of each compound were filtered through a 0.22 μm PTFE syringe filter and placed in clean vials equipped with tight-fitting caps with pierced rubber septa for slow solvent evaporation. Crystals were mounted in inert oil, and transferred to the cold gas stream of a Bruker Apex-II equipped with either

synchrotron radiation from the Advanced Photon Source (APS) at Argonne National Laboratory or a CuKα radiation source at the Integrated Molecular Structure Education and Research Center (IMSERC) of Northwestern University. SADABS was used for absorption correction of the **BDT**, **BDF**, and **aBDT** crystals, and SAINTPLUS for the **NDT** crystal.

4.2.6 Film grazing incidence X-ray scattering

Grazing incidence X-ray scattering (GIXS) was performed at Beamline 8ID at the Advanced Photon Source (APS) at Argonne National Laboratory. Thin films of the active layer were spun-cast on Si/SiO_2 wafers under the same conditions used for OPVs. Films were illuminated with a 7.35 keV (λ = 1.6868 nm) X-ray beam at an incident angle of 0.19°. Exposure times were varied between 10 and 30 s and the scattered X-ray beam, described by the scattering vector q, was collected on a Pilatus detector located 204 mm from the sample. The scattering vector $q = 4\pi sin(\theta)/\lambda$, where θ is the angle of scatter and q is inversely proportional to the d-spacing of a given diffraction plane, $q = 2\pi/d$. Data were normalized by exposure time.

Scherrer analysis was used to relate the peak width of a given diffraction spot associated with a Bragg plane to the crystalline correlation length, or the crystalline domain size, perpendicular to the given plane. The Scherrer equation is given in eq. 8,

$$D_{hkl} = \frac{2\pi K}{\Delta q_{hkl}} \tag{9}$$

where K is the Scherrer constant related to the domain shape, Δq_{hkl} is the full-width half maximum of the peak associated with Bragg reflection (*hkl*), and D_{hkl} is the crystalline domain size perpendicular to plane (*hkl)*. A corrected Δq_{hkl} was used to account for instrumental resolution and $K = 0.9$ for spherical organic domains.[91] Note that the Scherrer analysis calculates

a minimum domain size and does not account for degree of crystallinity, so a narrower peak can be attributed to either an increase in domain size or an increase in crystalline order.

4.2.7 Transmission electron microscopy (TEM) and atomic force microscopy (AFM)

TEM specimens were prepared under identical conditions as the corresponding solar cells using water-soluble PEDOT-PSS as an interfacial layer. After the active layer was spun cast, the PEDOT-PSS film was dissolved and the active layer was floated in DI water, enabling active layer film transfer to a TEM grid and drying before TEM analysis. TEM images were obtained on a Hitachi HD-2300A STEM. AFM active layer samples were analyzed using the same film fabrication conditions used for solar cell device fabrication without deposition of the top electrode. Data collection was performed on a Bruker Dimension ICON PT system in tapping mode with Si-cantilevers

4.2.8 Electronic structure calculations

The intermolecular electronic couplings relevant to hole transfer were calculated using geometries derived from the experimental crystal structures and a fragment based DFT calculation. The charge transfer integrals between HOMO orbitals on each molecule were calculated at the B3LYP/ADZP level of theory using the Amsterdam Density Functional (ADF) software package. Here ADZP is an augmented double-zeta polarizable basis set specifically developed for ADF's architecture. In the calculation, Kohn-Sham orbitals calculated for each molecule in isolation are used to evaluate the charge transfer integral between pairs of molecules.

The internal reorganization energy, λ_i, was calculated from the standard definition based on the Marcus reaction coordinates.[323, 324] In the case of cation self-exchange between identical subunits, this takes the form of eq. 10,

$$\lambda_i = E_+(0) + E_0(+) - E_+(+) - E_0(0) \quad (10)$$

where + and 0 refer to the cation and neutral species, subscripts refer to the electronic configuration, and parentheses refer to the geometric configurations (e.g., $E_+(0)$ refers to the total energy of the donor cation in the optimized neutral geometry). To evaluate the four energies in eq. 8, geometry optimizations of each donor cation and neutral species were first carried out at the B3LYP/6-31G* level using frequency analysis to confirm the minima. Single point calculations on these geometries, in each electronic configuration, were performed to obtain the terms in eq. 10.

Optical bandgap energies were computed from time-dependent density functional theory (TD-DFT) at the B3LYP/6-31G* level on the optimized neutral geometry of each donor. The first singlet excitation of non-zero oscillator strength is reported. HOMO energies were obtained from the single point calculations on the optimized neutral geometries of each donor. HOMO energies are used here as approximations of the diabatic (vertical) ionization potential of each donor for comparison with electrochemistry. All geometry optimizations, single point calculations, and TD-DFT calculations were performed with QCHEM 4.0.[325]

4.2.9 Organic field effect transistor fabrication

Bottom-gate/top-contact OFETs were fabricated on p^+-Si/SiO_2 (300 nm thermal oxide; Montco Silicon Technologies Inc.) coated with an octadecyltrichlorosilane (OTS) self-assembled monolayer to afford an advancing aqueous contact angle of 102°–103°. The molecular

semiconductor concentration was 5 mg·mL^{-1} and all solutions were filtered through a 0.45 μm PTFE membrane prior to spin-coating. Semiconductors were spun-cast at 1500 rpm for 30 s and then annealed at various temperatures under N_2. Gold source/drain electrodes were then thermally evaporated through a shadow mask (W = 5000, L = 100 μm) to afford a final device structure, Si/SiO_2/molecule/Au.

4.2.10 Space charge limited current (SCLC) single carrier diode fabrication

Hole-only diodes were fabricated on ITO coated glass with a PEDOT:PSS bottom contact and a MoO_3/Au top contact (2–3 nm MoO_3; 50 nm Au). The top contact was the injecting electrode and device areas (A) were 200 x 200 μm^2. The current density, J, as a function of applied macroscopic electric field, E, displayed both Ohmic and space charge limited regimes. The latter was fit using the model of eq. 10 to extract the zero-field mobility, μ_0, and the field dependence coefficient, γ,

$$J = \frac{9}{8}\frac{\varepsilon_s}{L}E^2\mu_0\exp\left(0.89\gamma\sqrt{E}\right) \tag{11}$$

where ε_s and L are the semiconductor permittivity (taken as $3\varepsilon_0$) and thickness, respectively. Film thicknesses were 130–190 nm for the neat materials and 200–230 nm for the blends. Averages were taken over four separate devices. The Ohmic regime was also fit with a low-field carrier density, n_0, using eq. 11, and the applied voltage was corrected for the series resistance of the ITO (10 Ω; eq. 12).

$$J = n_0 e \mu_0 E \tag{12}$$

$$E = \frac{V_{applied} - JAR_{series}}{L} \tag{13}$$

Devices were measured in the dark in vacuo using an Agilent B1500A semiconductor parameter analyzer.

4.2.11 Organic photovoltaic (OPV) cell fabrication and characterization

Pre-patterned ITO-coated glass (Thin Film Device, Inc.) with a resistivity of <10Ω and thickness of 280 nm was cleaned by sequential sonications at 50 °C in soap/DI water, DI water, methanol, isopropanol, and acetone for 30 min each. ITO substrates were next treated for 5 min in an O_2 plasma cleaner at 100 mTorr (Harrick Plasma). PEDOT:PSS (Clevios P VP Al 4083) was then spun-cast at 5000 rpm for 30 s on them and subsequently annealed at 150 °C for 15 min. Samples were then transferred to a N_2-filled glove box for active layer and top contact deposition. Active layers containing the donor molecules and the PCBM acceptor (>99.5% pure, American Dye Source) were formulated inside the glove box in a 1.5:1.0 (w:w) ratio at a molecule concentration of 7 $mg \cdot mL^{-1}$ in anhydrous chloroform ($CHCl_3$). Active layer solutions were stirred at 600 – 800 rpm for 1.5 h at 50ºC, then spun-cast at 4000 rpm for 15 s to afford an active layer thickness of ~70 nm by profilometry. Samples were then thermally annealed between 70–130 ºC for 10 min on a temperature-controlled hot plate. To complete device fabrication, LiF(1.0 nm)/Al(100 nm) were thermally evaporated, sequentially, at a base pressure of $\sim 2.0 \times 10^{-6}$ Torr. The top Al electrodes were finally encapsulated with UV-curable epoxy and a glass slide before device evaluation. Each substrate contained 4 pixels with a defined area of 0.065 cm^2 each.

OPV characterization was performed on a Spectra-Nova Class A Solar Simulator with AM1.5G light (100 mW/cm^2) from a Xe arc lamp. The light source was calibrated with an NREL-certified Si diode equipped with a KG3 filter to bring spectral mismatch to unity. Current

vs. potential (*J-V*) measurements were recorded with a Keithly 2400 digital source meter. External quantum efficiency (EQE) measurements were performed using an Oriel Model S2QE-PV-SI (Newport Instruments) equipped with a NIST-certified Si-diode, a Merlin lock-in amplifier, an optical chopper, and a 300 W Xe arc lamp.

4.3 Results

4.3.1 Solution and film optical absorption properties

Optical absorption spectra were obtained and extinction coefficients measured for each of the pristine small molecules (Figure 4.1A). The solution absorption spectra in chloroform of the D-A molecule **aBDT** has an absorption onset at λ_{onset} = 634 nm with λ_{max} = 590 nm, corresponding to a bandgap (E_g) = 1.96 eV (Table 4.1). However, the A-D-A molecules have red-shifted absorptions with $\lambda_{onset} \approx 670$ nm and $E_g \approx 1.86$ eV. The molar extinction coefficients (ε) of the A-D-A molecules (~1.1–1.5 × 10^{-5} $L \cdot mol^{-1} \cdot cm^{-1}$) are approximately twice that of the D-A molecule (0.58 × 10^{-5} $L \cdot mol^{-1} \cdot cm^{-1}$), which suggests that the absorption profile is dominated by the DPP acceptor moiety.

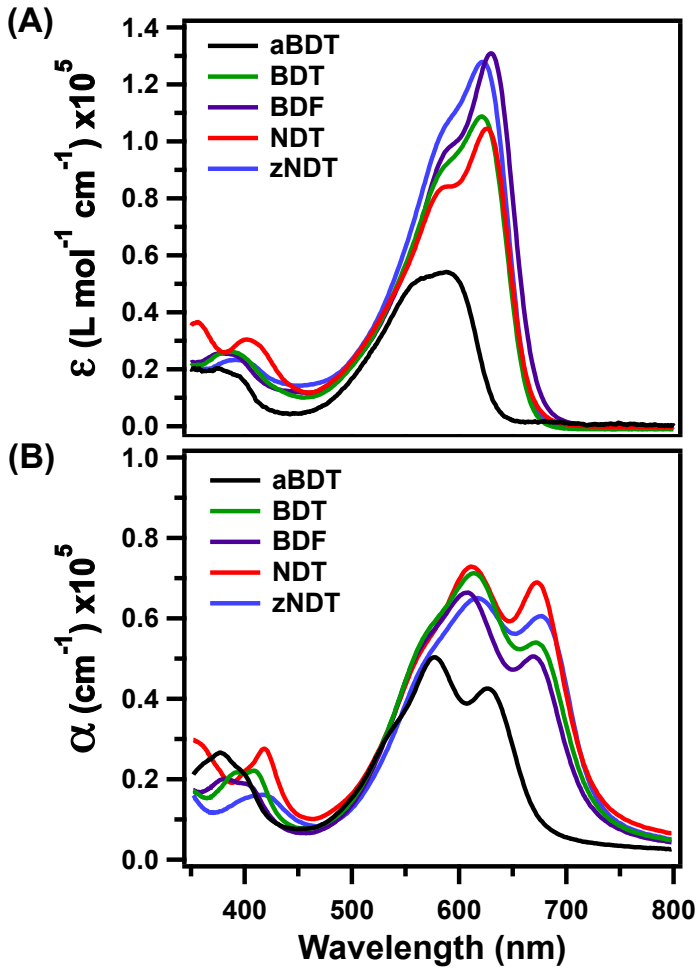

Figure 4.1. Optical absorption spectra of (A) small-molecule solutions in $CHCl_3$ showing calculated molar extinction coefficients and (B) neat, annealed small-molecule thin films cast from $CHCl_3$ showing absorption coefficients

Table 4.1. Optical properties and energetics of pristine small-molecule compounds in solution and as thin films

	Solution Properties			*Film Properties*			*Energetics*	
Compound	ε ($L \cdot mol^{-1} \cdot cm^{-1}$)	λ_{onset} (nm)	E_g (eV)	α (cm^{-1})	λ_{onset} (nm)	E_g (eV)	IP[a] (eV)	EA[b] (eV)
aBDT	0.54×10^5	634	1.96	0.50×10^5	681	1.82	5.23	3.39
BDT	1.09×10^5	671	1.85	0.71×10^5	729	1.70	5.16	3.40
BDF	1.31×10^5	666	1.86	0.66×10^5	724	1.71	5.19	3.45
NDT	1.05×10^5	666	1.86	0.73×10^5	722	1.72	5.13	3.46
zNDT	1.28×10^5	664	1.87	0.65×10^5	732	1.69	5.13	3.39

[a]Ionization potential. [b]Electron affinity measured by CV.

Note that the absorption onsets of the film spectra (Figure 4.1B) are red-shifted by 47 - 68 nm relative to the solution spectra and exhibit vibronic features (~60 nm, 1220 cm^{-1}) consistent with crystallite formation in the solid state.[326] **zNDT** has the largest red-shift (68 nm) indicating most aggregation while **aBDT** exhibits the smallest red shift (47 nm) indicating that it is the most weakly aggregated. The thin-film E_g is ~1.7 eV for all the A-D-A molecules and 1.8 eV for **aBDT**. The film absorption coefficients (α) for the A-D-A molecules are ~0.7×10^{-5} cm^{-1}, while $\alpha = 0.5 \times 10^{-5}$ cm^{-1} for **aBDT**.

4.3.2 Electronic properties from cyclic voltammetry

CV was used to extract the ionization potential (IP) and electron affinity (EA) of the new compounds. The voltammograms of all of the present molecules exhibit a quasi-reversible reduction peak at ~ –1.2 V, assignable to the reduction of the flanking DPP units,[327] and multiple oxidation peaks at +0.6 V and higher potentials, assignable to the oxidation processes associated with the electron-rich cores and end-capping thiophenes (Figure 4.2). From the CV data, the EA is approximated from the onset of the reduction and IP from the onset of oxidation (Table 4.1). Note that, as the conjugation length is increased from **aBDT** to **zNDT**, the IP decreases from 5.23 eV to 5.13 eV, suggesting that the oxidation process is energetically more favorable for **zNDT** and the other π-extended molecules than for **aBDT**. This difference is likely due to the larger extent of π-conjugation in the A-D-A molecules, which better stabilizes an oxidized cationic species versus a smaller D-A structure.[328] This result is also supported by the DFT calculations of the HOMO energies (Table 4.2), where **aBDT** is predicted to have the lowest lying HOMO level. EA values are similar and range from 3.39–3.46 eV, suggesting that the EA is influenced primarily by the TDPP electron-withdrawing unit. The energy level alignment of

the charge-separated states and singlet states inferred from the IPs and optical bandgaps ($E_{g,D}$) of the donors, and EA of PCBM, imply a sufficient energetic offset for charge separation in blends of these donors with PCBM. [101]

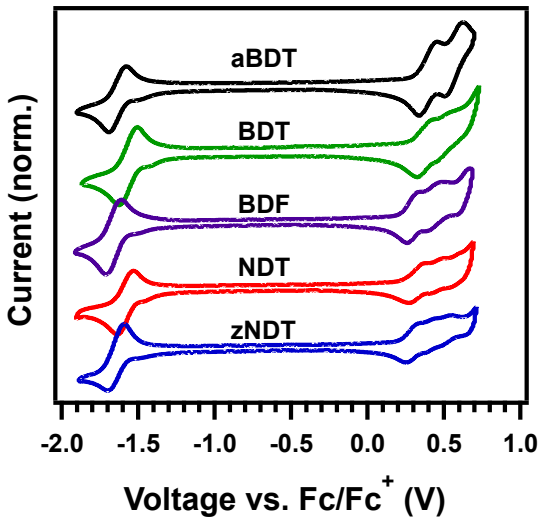

Figure 4.2. Cyclic voltammetry plots of the indicated small molecules as CH_2Cl_2 solutions

Table 4.2. Calculated HOMO energies

Compound	**aBDT**	**BDT**	**BDF**	**NDT**	**zNDT**
HOMO (eV)	-4.90	-4.84	-4.71	-4.84	-4.73

4.3.3 Differential scanning calorimetry

All of the present semiconductors except **zNDT** exhibit melting and crystallization transitions in the DSC measurements (Figure 4.3). **aBDT** has the lowest melting (T_m = 145 ºC) and crystallization temperature (T_c = 104 ºC) of the materials investigated, suggesting that it has the weakest intermolecular cohesion. In contrast, both **BDT** and **BDF**, which possess two terminal DPP units, have significantly higher melting, T_m= 272 and 267 °C, respectively, and crystallization temperatures, T_c = 249 and 240 ºC, respectively, which is not unexpected from the extended π-conjugated backbones. Further extension of the π-conjugated **NDT** results in higher melting (T_m = 299 °C) and crystallization temperatures (T_c = 280 ºC) than **BDT**. Since neither melting nor crystallization transitions are observed for **zNDT** over the temperature ranges investigated, **zNDT** is likely to have very strong intermolecular cohesion.

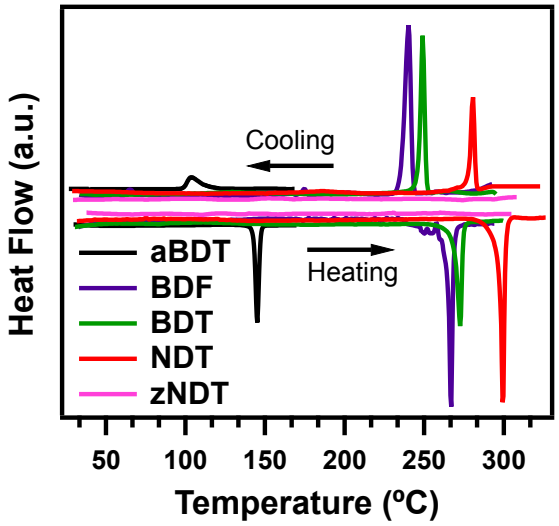

Figure 4.3. Differential scanning calorimetry scans showing the endothermic melting temperature (negative peak) and the exothermic crystallization temperature (positive peak) of the indicated small molecules

4.3.4 Crystal structures

Single crystals of **aBDT**, **BDT**, **NDT**, and **BDF** suitable for diffraction studies were obtained using slow evaporation methods. Despite several attempts, diffraction quality single crystals of **zNDT** could not be obtained. All materials form needle-shaped crystals, and the symmetric A-D-A molecular crystals are a shiny bronze color while **aBDT** crystals are dull purple. Unit cell parameters and structure solution details are summarized in Appendix B. Relevant geometries and intermolecular distances in the single crystal determinations are defined in Figure 4.4.

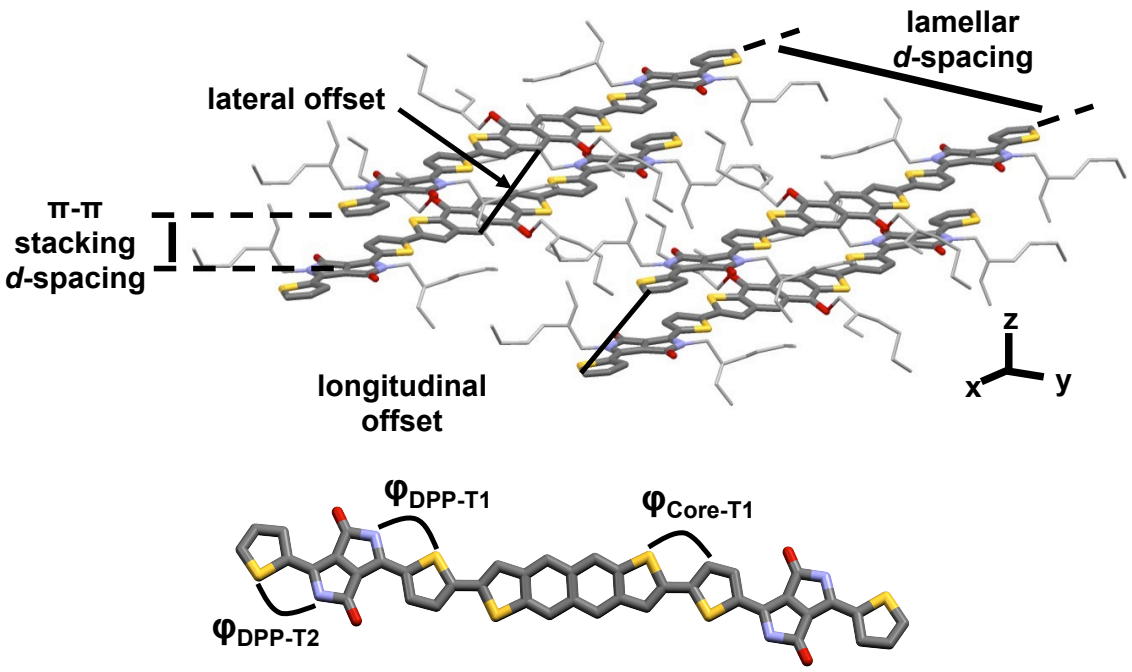

Figure 4.4. Relevant solid state geometries and distances, exemplified by the crystal structure of **NDT**. Lateral and longitudinal offsets describe the relative locations of neighboring $\pi - \pi$ stacked molecules where lateral offset is along the *y*-axis and the longitudinal offset is along the *x*-axis. The $\pi - \pi$ stacking *d*-spacing is the shortest distance perpendicular to the backbones parallel to the *z*-axis. The symbol φ denotes torsional angle about the indicated bond.

aBDT crystallizes in space group $P2_1/c$ with each unit cell containing four **aBDT** molecules stacked head-to-tail in pairs with a large longitudinal offset 5.874(3) Å within a head-to-tail pair and a small longitudinal offset of 1.698(6) Å between pairs (Figure 4.5A). The π–π stacking *d*-spacing averages 3.591 Å, while the lamellar *d*-spacing between molecular backbones is 15.776(4) Å (Table 4.3). The backbone exhibits twisting at the BDT-T1 ($\varphi_{BDT\text{-}T1}$ = 11.3(18)°) and DPP-T2 ($\varphi_{DPP\text{-}T2}$ = 13.6(15)°) junctures, where T1 is the interior flanking thiophene and T2 is the end-capping thiophene (Figure 4.4). **BDT** (Figure 4.5B) and **BDF** (Figure 4.5C) both have four molecules per unit cell in space group C2/c with the molecules slip-stacked with a longitudinal offset of 4.2-4.4 Å, and stacks alternating in their angular offset from the perpendicular to form a zig-zag, slip-stack packing motif. The longitudinal offset is smaller than in **aBDT** and results in the alignment of T1 over the core and the DPP over the flanking thiophene, T2 (Figure 4.5B, C). The π–π stacking distance is 3.3797(1) and 3.4161(8) Å for **BDF** and **BDT**, respectively. The lamellar *d*-spacing, determined by the side chain orientation, is 16.780(6) Å and 17.051(7) Å for **BDT** and **BDF**, respectively. The **BDF** exhibits slight torsion of the backbone core (T1-D-T1) and twisted acceptor moieties ($\varphi_{DPP\text{-}T1}$ = -6.519(4)° and $\varphi_{DPP\text{-}T2}$ = 13.444(7)°), while the **BDT** extended A-T1-D-T1-A backbone is flatter ($\varphi_{Core\text{-}T1}$ = 2.1904(9)°, $\varphi_{DPP\text{-}T1}$ = 5.7036(2)°) with similarly twisted end-capping thiophenes ($\varphi_{DPP\text{-}T2}$ = 14.314(4)°).

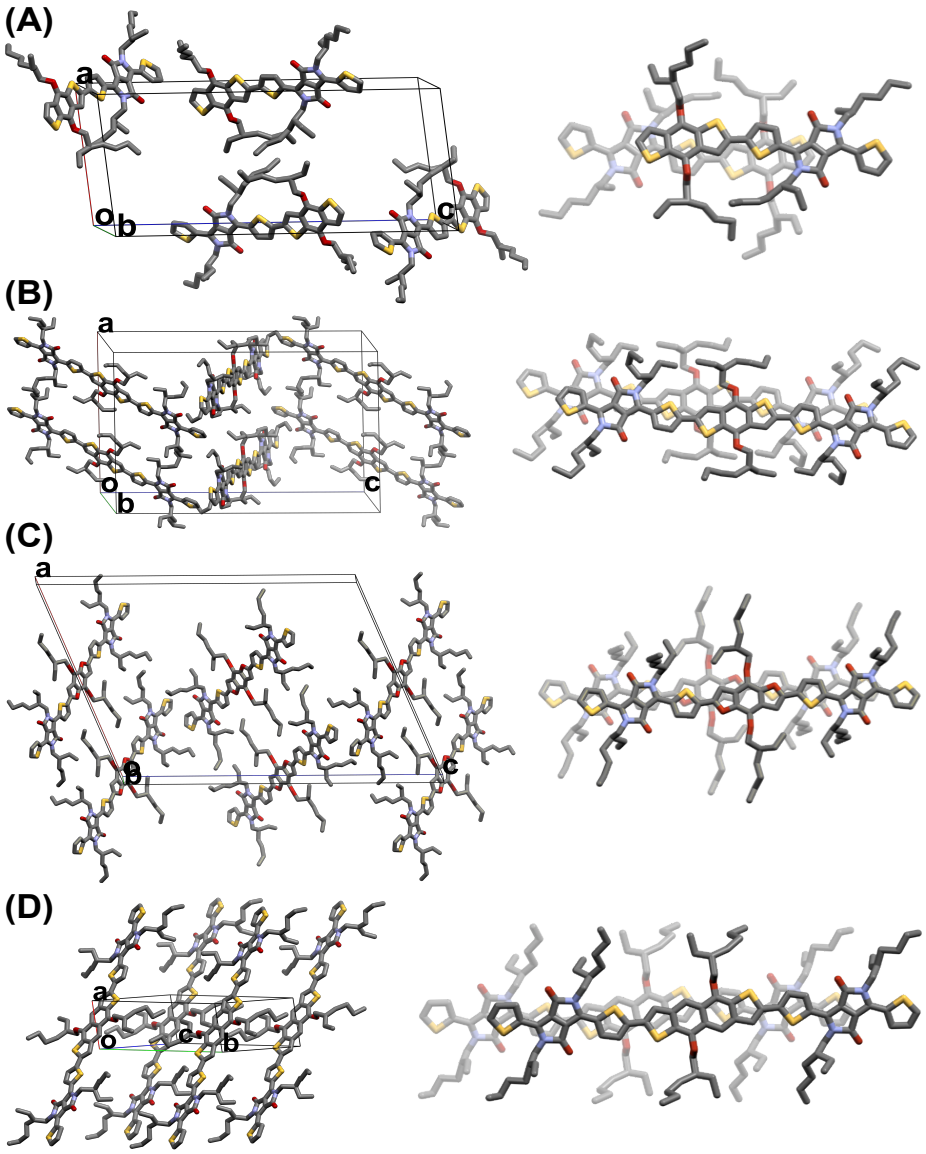

Figure 4.5. Single crystal unit cell packing diagrams (left) and π-stacking viewed along the stacking direction of the molecules (right) of (A**) aBDT**, (B) **BDT**, (C) **BDF**, and (D) **NDT**

Table 4.3. Single crystal *d*-spacings, torsional angles, and longitudinal offsets by X-ray diffraction

Compound	*d*-spacing (Å)		Torsional angles (°)			Long.	Density
	Lam.	π–π	$\varphi_{Core\text{-}T1}$	$\varphi_{DPP\text{-}T1}$	$\varphi_{DPP\text{-}T2}$	offset (Å)	(g/cm^3)
aBDT	15.776(4)	3.522(4) 3.660(4)*	11.3(18)	0.8(12)	13.6(15)	5.874(3) 1.698(6)*	1.222
BDT	16.780(6)	3.4161(8)	2.9104(9)	5.7036(2)	14.314(4)	4.444(2)	1.241
BDF	17.051(7)	3.3797(1)	5.844(2)	-6.519(4)	13.444(7)	4.274(3)	1.243
NDT	20.3068(2)	3.5233(3)	7.6256(8)	10.097(1)	2.3508(3)	5.3344(6)	1.252

*Between neighboring head-to-tail stacked molecule pairs

NDT crystallizes in space group $P\bar{1}$ with one molecule per unit cell (Figure 4.5D**)**. It has a longer longitudinal offset than **BDT** (5.3344(6) Å) in the slip-stacked structure, but the smallest lateral offset. The molecular backbone is slightly twisted at all junctions with $\varphi_{NDT\text{-}T1}$ = 7.6256(8)°, $\varphi_{DPP\text{-}T1}$ = 10.097(1)°, and $\varphi_{DPP\text{-}T2}$ = 2.3508(3)° with the most torsion through the center of the backbone (A-T1-D-T1-A). The π–π stacking distance is slightly longer than in the other ADA molecules at 3.5233(3) Å, but **NDT** has a large lamellar *d*-spacing of 20.3068(2) Å.

4.3.5 Active layer domain sizes and molecular orientations

Thin films of the neat small molecules and the small-molecule:PCBM (1.5:1.0) blends were prepared by spin-casting, and after annealing were characterized using grazing incidence x-ray scattering (GIXS) (Figure 4.6). Powder diffraction data generated from the single crystal diffraction data qualitatively match the GIXS features (Figure 4.7) and permit determination of crystallite orientational preference, *d*-spacing, and domain size in the films. The lamellar *d*-spacings and π–π stacking *d*-spacings can be estimated from the GIXS diffraction planes, and the (*hkl*) planes are identified by matching the GIXS plane orientation to the molecular orientations in the single crystal. Peak identification and the peaks used for lamellar and π–π stacking analyses are compiled in Table B.2-B.5 in Appendix B.

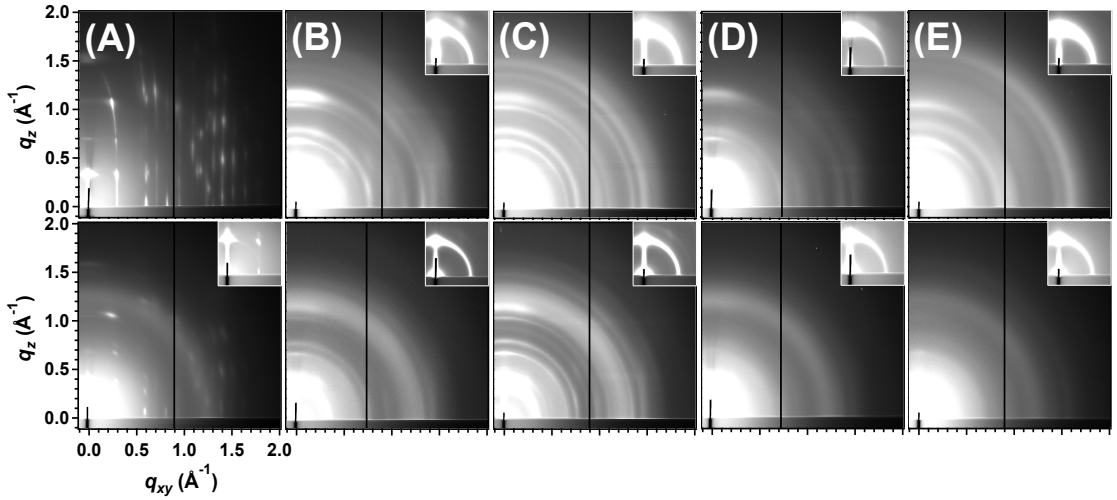

Figure 4.6. Grazing incidence X-ray scattering detector images of annealed thin films of neat small-molecule (top) and small-molecule:PCBM (1.5:1.0 w/w, bottom) materials; (A) **aBDT**, (B) **BDT**, (C) **BDF**, (D) **NDT**, (E) **zNDT**. Insets show lamellar stacking peak in the small q regime (q = 0-0.5 Å^{-1})

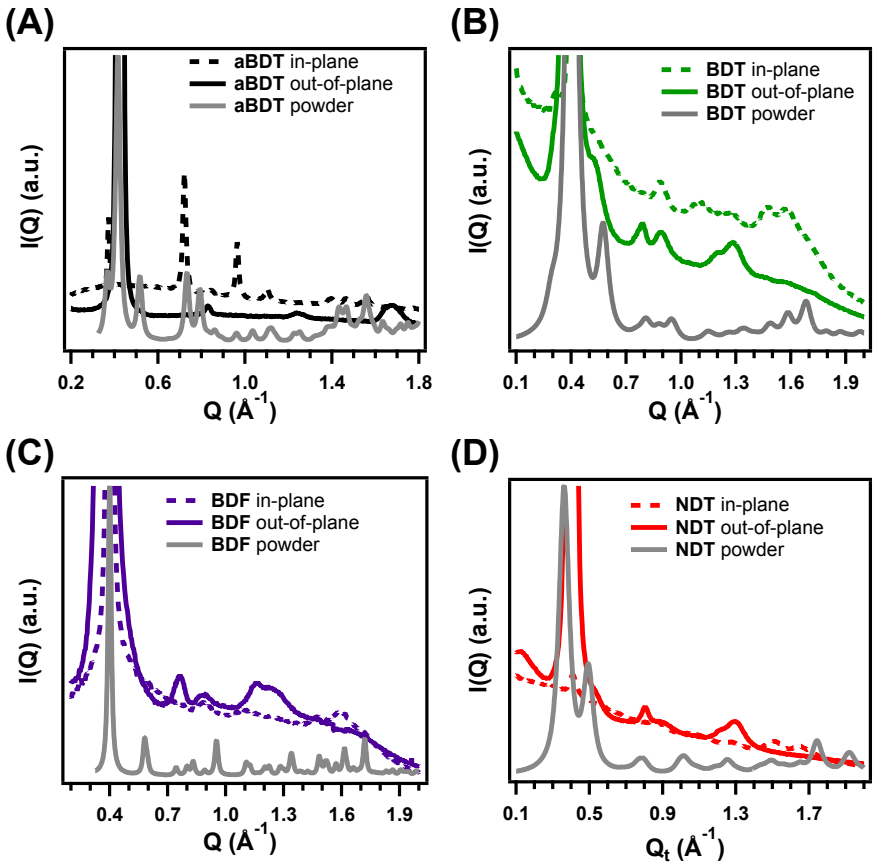

Figure 4.7. Comparison of powder diffraction calculated from the single crystal structure and data showing in-plane and out-of-plane structure from GIWAXS

aBDT forms the most crystalline films, consistent with the ease of single crystal growth. It exhibits diffraction points (Figure 4.6A) indicating preferential orientation with the (*100*) axis normal to the substrate. The neat **aBDT** film annealed at 80 °C has a compressed lamellar *d*-spacing of 14.8 Å vs. 16.0 Å in the single crystal and a significantly increased π-π stacking *d*-spacing of 4.0 Å vs. 3.5 Å in the single crystal (Table 4.4). The **aBDT**:PCBM OPV thin films are less crystalline (Figure 4.6A, bottom) and the lamellar *d*-spacing expands to 15.3 Å while the π–π stacking *d*-spacing remains virtually unchanged (4.0 Å vs 4.1 Å).Using Scherrer analysis, the lamellar domain size of **aBDT** is determined to be 75.1 ± 0.4 nm and 42.3 ± 1.4 nm, and the π–π stacking domains are 10.8 ± 4.3 nm and 8.7 ± 0.8 nm, in the neat and PCBM blend films, respectively (Table 4.4). The large domain sizes in the blend film are clearly evident from the transmission electron micrographs and atomic force micrographs, which show a rough film (RMS roughness = 3.6 nm) with large phase-segregated domains (Figure 4.8). The darker areas are assigned to PCBM domains based on energy dispersive x-ray spectroscopy (EDS) while the lighter areas are primarily small molecule domains. In qualitative agreement with the aforementioned GIXS Scherrer analysis, the **aBDT** films have large, phase separated donor domains, while all A-D-A films all exhibit smaller intermixed domains. The AFM (Figure 4.8, inset) surface topology closely parallels that observed by TEM. In particular, the **aBDT**:PCBM blend film has the largest domain sizes and the roughest surface (RMS = 3.6 nm), indicating the presence of large **aBDT** crystals. The decreased blend domain size suggests disruption of the **aBDT** domain regularity by PCBM molecules, which is likely accompanied by increased crystalline disorder.

Table 4.4. GIXS thin film molecular *d*-spacing data and crystalline domain sizes calculated by Scherrer analysis

Compound	*d*-spacing (Å)				Crystalline Domain Size (nm)			
	Neat		*Blend*		*Neat*		*Blend*	
	(lam.)	(π-π)	(lam.)	(π-π)	(lam.)	(π-π)	(lam.)	(π-π)
aBDT	14.8	4.0	15.3	4.1	75.1(0.4)	10.8(4.3)	42.3(1.4)	8.7(0.8)
BDT	16.9	4.3	16.7	4.0	17.7(0.2)	7.0(0.2)	17.0(0.2)	11.0(0.7)
BDF	16.8	3.9	15.5	3.9	18.2(0.2)	7.7(0.2)	18.7(0.2)	11.2(1.2)
NDT	16.5	3.8	16.6	3.9	17.5(0.1)	8.8(0.2)	13.7(0.2)	9.1(0.3)
zNDT	13.4	3.9	13.5	3.9	13.4(0.1)	4.8(0.1)	14.1(0.2)	4.1(1.8)

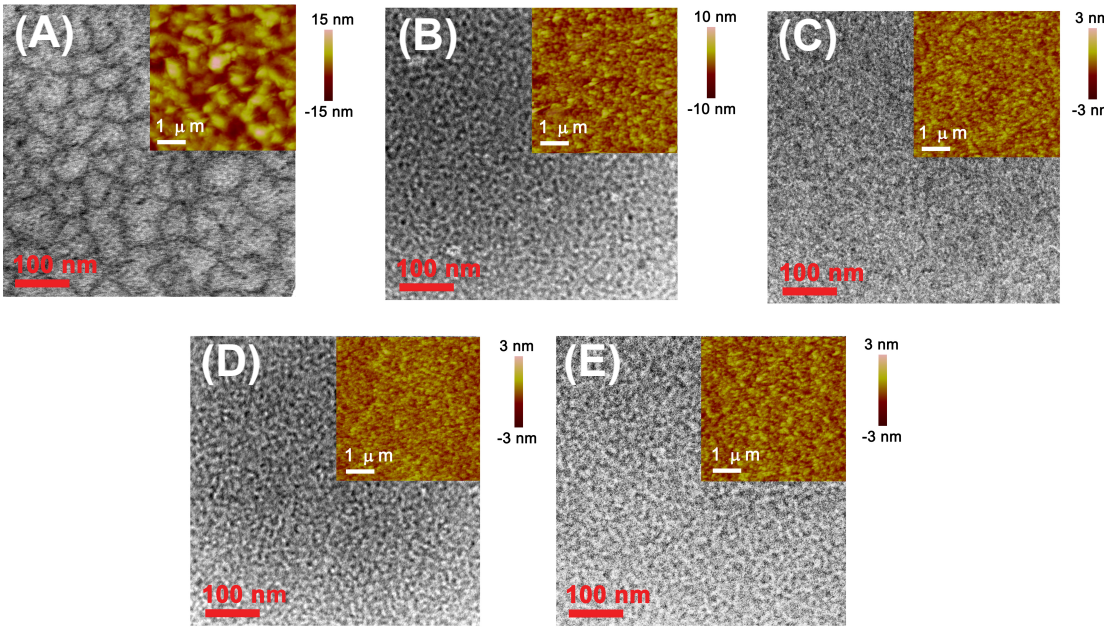

Figure 4.8. Transmission electron and atomic force micrographs (insets) of blend annealed SM:PCBM films, (A) **aBDT**, (B) **BDT**, (C) **BDF**, (D) **NDT**, (E) **zNDT**, showing varied domain sizes and roughnesses

Unlike **aBDT**, **BDT** exhibits rings and arcs in the neat annealed film GIXS (Figure 6B, top) indicating decreased preferential crystallite orientation. The single crystal **BDT** lamellar spacing is indistinguishable from the neat and blend films, however, the π–π stacking distances of 4.3 Å (neat) and 4.0 Å (blend) are significantly larger (Table 4.4) than 3.5 Å. The increase in π–π stacking *d*-spacing from single crystal to thin film may reflect changes in side chain orientations.[272, 309, 329] The π–π stacking *d*-spacing decreases upon PCBM incorporation from 4.3 Å to 4.0 Å. In addition to the π–π stacking peak displacement, a narrowing of the π–π stacking peak indicates increased π–π stacking domain sizes from 7.0 ± 0.2 nm (neat) to 11.0 ± 0.7 nm (blend). Concurrently, the lamellar stacking domains shrink from 17.7 ± 0.2 nm (neat) to 17.0 ± 0.2 nm (blend), affording a finely interpenetrating morphology (Figure 4.8B).

BDF has comparable crystallinity, *d*-spacings, and domain sizes to **BDT**, but with slight variations between the neat and the blended films (Figure 4.6C). The lamellar *d*-spacing is slightly smaller in the neat films (16.8 Å) vs. that in the single crystal (17.1 Å), but then falls significantly to 15.5 Å upon PCBM addition (Table 4.4). The π–π stacking *d*-spacing remains constant at 3.9 Å, which is 0.4 Å larger than the single crystal π–π stacking distance of 3.5 Å. When blended with PCBM, the lamellar domain size slightly expands from 18.2 ± 0.2 nm to 18.7 ± 0.2 nm while the π–π stacking domain size increases from 7.7 ± 0.2 nm to 11.2 ± 1.2 nm (Table 4.4). As with **BDT**, it appears that PCBM addition increases **BDF** structural order in the π–π stacked domains while promoting a contraction in lamellar *d*-spacing, thereby creating a more tightly packed **BDF** crystal.

Similar to the other A-D-A small molecules[300, 330] **NDT** has compressed lamellar *d*-spacings and expanded π–π stacking distances when cast as thin films versus the single crystal,

but is slightly less crystalline than **BDT** as evidenced by fewer diffraction peaks (Figure 4.6D, top). The lamellar *d*-spacing in the neat and blend films is compressed ~ 0.9 Å from the single crystal and the π–π stacking is expanded 0.3 Å to 3.8 – 3.9 Å in both the neat and blend films (Table 4.4), relative to **BDT**. While the lamellar *d*-spacing does not change on PCBM addition, the lamellar domain size falls from 17.5 ± 0.1 nm to 13.7 ± 0.2 nm (Table 4.4). No significant change is observed in the π-π stacking domain size.

zNDT exhibits the fewest diffraction rings, which correlates with decreased crystalline order (Figure 4.6E, top), and the location and relative intensities of the Bragg features suggest that crystal packing is similar to that in **NDT**. The small lamellar *d*-spacing of 13.4 Å makes **zNDT** the most tightly packed molecule in the neat thin film (Table 4.4). The π–π stacking distance is 3.9 Å, and the *d*-spacing is insensitive to PCBM addition. Unlike in **NDT** films, the **zNDT** lamellar domain size increases slightly from 13.4 ± 0.1 nm to 14.1 ± 0.2 nm with addition of PCBM (Table 4.4). Overall, the scattering intensity decreases significantly in the blend films indicating decreased **zNDT** crystallinity (Figure 4.6E, bottom).

In all of the present A-D-A small molecules, the diffraction peaks are broad arcs in the GIXS image array while in the D-A **aBDT** films, distinct diffraction points are observed (Figure 4.6). Diffraction points indicate oriented crystallites while rings or arcs signify varying degrees of orientational disorder within the film. The isotropic ring at low q (q = 0.3 – 0.4 Å^{-1}) corresponds to the lamellar *d*-spacing, but the π–π stacking peak (q = 1.5 Å^{-1}) is anisotropic and always occurs as an arc growing from the horizontal q_{xy} axis. This observation indicates that lamellar packed sheets of molecules can be oriented in any direction, but three-dimensional crystals with π–π stacked networks are preferentially oriented with the stacking axis parallel to

the substrate in an edge-on alignment (Figure 4.9A). Depending on the π–π stacking arc length, the degree of orientational preference can be estimated. By plotting the π–π stacking arc intensity versus the scattering angle, we determine the relative crystallite orientational order. The point at which the normalized intensity is equal to the baseline intensity is used to estimate the degree of preferential edge-on orientation in neat films (Figure 4.9B). From these plots, neat **BDT** exhibits the strongest edge-on preference with only a 22° orientational range while **NDT**, **BDF**, and **zNDT** exhibit decreasing edge-on preference and increasing face-on preference with angles of 25°, 56°, and 79°, respectively (Figure 4.9C). In the small-molecule PCBM blends, all films show comparable degrees of orientational preference with angles of 25–28° (Figure 4.9D).

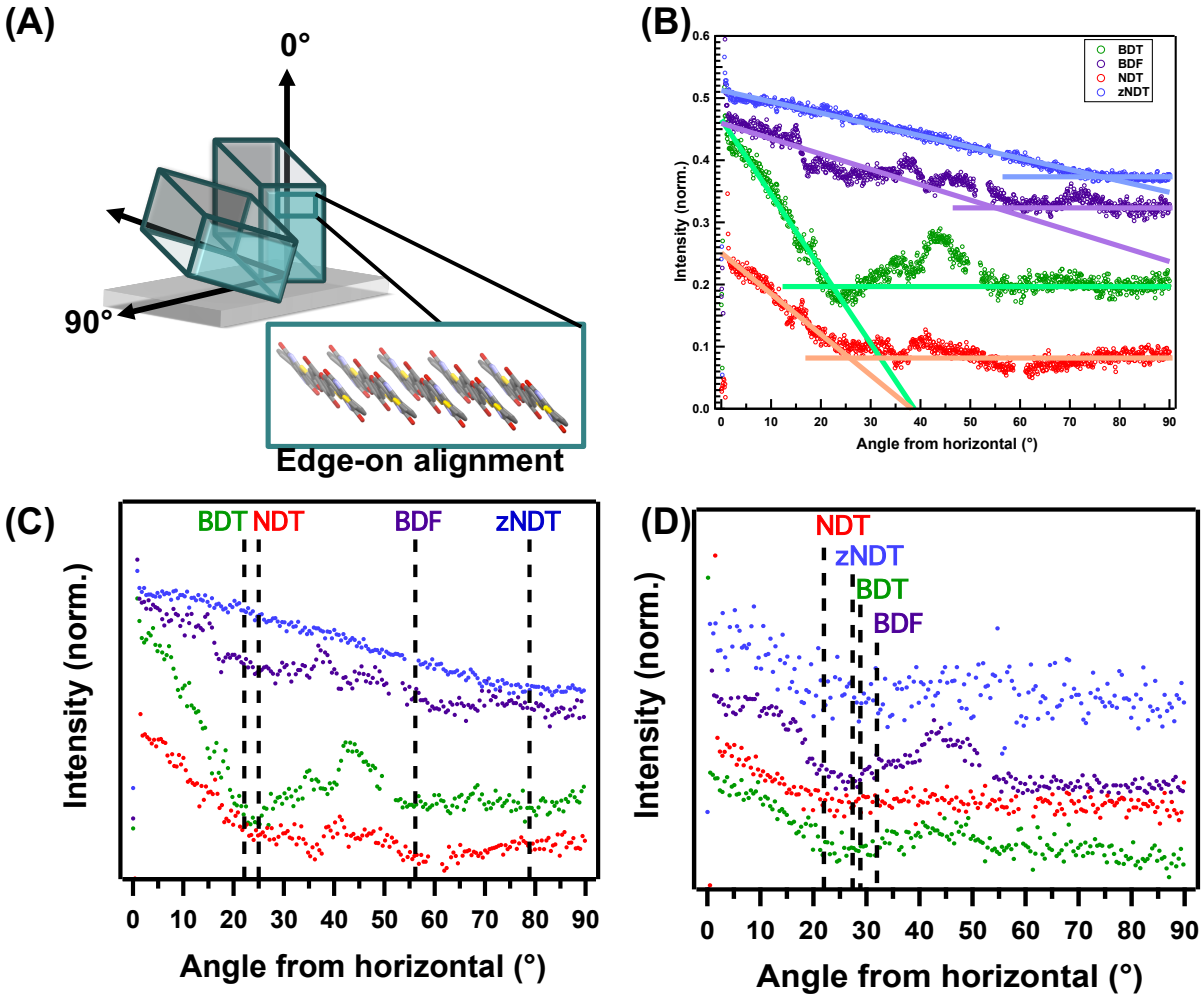

Figure 4.9. (A) Schematic of small-molecule domains in which the molecules are aligned edge-on at 0° tilt of the domain and face-on at 90° tilt of the domain. (B) Sample fits for circular linecuts of the π-π stacking peak in neat films to determine degree of preferential orientation. Angular dependence of the π–π stacking peak in (C) neat small-molecule films and (D) SM:PCBM blend films. The decrease in intensity of the π–π stacking feature vs the baseline is indicated by a dotted line and indicates the degree of orientational preference in each small-molecule system. The increase in intensity in **BDT** at 30–60° is due to an overlapping reflection.

4.3.6 Internal reorganization energies and co-facial electronic coupling

In the commonly employed Marcus description of charge transfer in a solid, the hole transfer rate, k_{CT} (eq. 14)

$$k_{CT} = \frac{V_{CT}^2}{\hbar}\sqrt{\frac{\pi}{\lambda k_B T}}\exp\left(-\frac{(\Delta G_{CT}+\lambda)^2}{4\lambda k_B T}\right) \quad (14)$$

is exponentially dependent on the charge transfer barrier height and proportional to the square of the electronic coupling parameter V_{CT} between the frontier MOs (FMOs) of the subunits. [323] For a uniform crystallite, the free energy of charge transfer, ΔG_{CT}, is zero, and the reorganization energy λ determines the barrier to charge transfer. The reorganization energy is further partitioned into an internal component, $\lambda_{i,}$, determined by the geometry change of the subunit upon ionization, and an external component, λ_{ext}, determined by the reorganization of the environment (e.g., solvation) due to the charge redistribution. [323, 331] To facilitate charge transfer and high mobility, it is paramount to efficiently couple the subunits that carry charge, and minimize the reorganization energy associated with charging of the subunits.

To investigate structure-property relationships between the crystallite packing motif and the charge transport properties of these semiconductors, both the internal reorganization energies and electronic coupling between the co-facial subunits within each crystal structure were computed (Table 4.5). Across the series, λ_i falls with increasing molecular size, with a large variance of 0.22 eV in λ_i between D-A compound **aBDT** and the A-D-A analog, **BDT**. Within the A-D-A series, the extended conjugation provided by each inserted benzene core results in a λ_i reduction of ~20–30 meV. This trend agrees well with the general design principle that larger and more rigid aromatic cores facilitate charge transfer via a reduction in the reorganization energy, [332] and is in general agreement with literature showing that the reorganization energy decreases with the expansion of the π system. [333]

Table 4.5. Computed reorganization energies, co-facial coupling, and experimental charge transport parameters for the indicated molecular donors

Compound	λ_i (meV)	π–π co-facial coupling (meV)	$\mu_{sat,\,h}$[a] ($cm^2 \cdot V^{-1}s^{-1}$)	μ_0[b] ($cm^2 \cdot V^{-1}s^{-1}$)
aBDT	398	34	$(1.3 \pm 0.3)\ 10^{-4}$	$(3.5 \pm 0.1)\ 10^{-5}$
BDT	172	131	$(5.0 \pm 0.9)\ 10^{-2}$	$(2.7 \pm 0.2)\ 10^{-4}$
BDF	186	141	$(3.2 \pm 0.1)\ 10^{-2}$	$(5.5 \pm 0.3)\ 10^{-4}$
NDT	155	98	$(3.8 \pm 0.7)\ 10^{-2}$	$(3.6 \pm 0.1)\ 10^{-4}$
zNDT	168	--	$(7.5 \pm 0.8)\ 10^{-2}$	$(1.3 \pm 0.2)\ 10^{-3}$

[a]In-plane mobility derived from top contact/bottom gate OFET architecture. [b]Out-of-plane mobility derived from hole-only diodes fit with a SCLC model.

We have also utilized the donor unit cell dimensions to make a physically reasonable assessment of the electronic couplings in the BHJ blends. Since the electronic coupling is sensitive to the orbital overlap between subunits, it is also strongly dependent on the relative orientation and spacing of the molecules. Utilizing known geometries provides a substantial advantage over estimates of the couplings based on "guessed" orientations. As for reorganization energies, the calculated couplings also show the largest difference between D-A molecule **aBDT** and A-D-A analog, **BDT**. The small coupling results from the paired head-to-tail configuration of the co-facial units in the **aBDT** unit cell (Figure 4.5A). Since the HOMO orbital has a strong contribution from the DPP component, poor overlap results in reduced couplings (Figure 4.10).

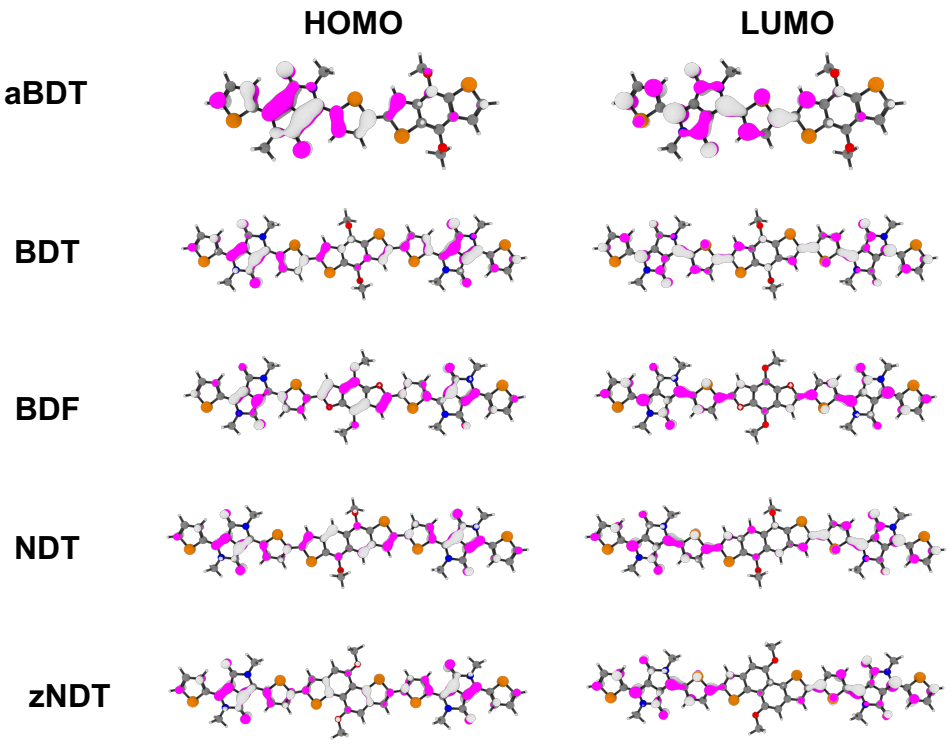

Figure 4.10. Frontier molecular orbitals calculated by TD-DFT.

4.3.7 OFET and SCLC transport properties

To probe the charge transport characteristics of these small-molecule materials and to relate the crystal structures to observed physical parameters, the hole mobility *parallel* to the substrate (in-plane) was measured in a top contact/bottom gate OFET architecture for the neat semiconductors (Table 4.5). Spun-cast **aBDT** films show the lowest saturated hole mobility ($\mu_{sat,\ h}$ = 1.3 x 10^{-4} $cm^2 \cdot V^{-1}s^{-1}$) while **NDT** and **BDF** films have larger and comparable mobilities ($\mu_{sat,\ h}$ = ~3.5 x 10^{-2} $cm^2 \cdot V^{-1}s^{-1}$). In contrast, the **zNDT** mobility ($\mu_{sat,\ h}$ = 7.5 x 10^{-2} $cm^2 \cdot V^{-1}s^{-1}$) is twice the **NDT** mobility, likely reflecting increased intermolecular π-π orbital overlap of the low aspect ratio **zNDT** core.

To probe the charge transport properties of these materials in the direction *perpendicular* to the substrate (out-of-plane), hole-only diodes of the neat donor materials were next fabricated, and the zero field mobility (μ_o) was extracted from the space charge limited current (SCLC) model (Table 4.5). Again it is found that the D-A **aBDT** films have significantly lower hole mobility (μ_o = 3.5 x 10^{-5} $cm^2 \cdot V^{-1}s^{-1}$) than the A-D-A analogues, which comports with the high computed reorganization energy and low co-facial coupling. Additionally, as in the OFET measurements, **zNDT** films exhibit the highest SCLC mobility, μ_o = 1.3 x 10^{-3} $cm^2 \cdot V^{-1}s^{-1}$, while **NDT** films have a lower SCLC mobility (μ_o = 3.6 x 10^{-4} $cm^2 \cdot V^{-1}s^{-1}$) than do **zNDT** films, again suggesting the shape of the **NDT** core is important for effective charge transport. Interestingly, **BDF** films have a larger SCLC mobility (μ_o = 5.5 x 10^{-4} $cm^2 \cdot V^{-1}s^{-1}$) than do **BDT** films, which is opposite the trend observed in the OFET measurements. This difference may reflect the relative orientational disorder in the thin films as noted above. [334]

4.3.8 OPV response

BHJ-OPV cells were fabricated to determine the impact of charge mobility and orientational disorder on solar cell metrics. Devices were optimized at a 1.5:1.0 w:w donor:acceptor ratio[314, 316, 335] and annealing is necessary to achieve optimal device performance. All of the present A-D-A BHJ films were annealed for 10 min at 130 °C and those with **aBDT** were annealed at 80 °C for 10 min. Cell performance characteristics are summarized in Table 4.6.

Table 4.6. Solar Cell *J-V* device metrics

Compound	V_{OC} (V)	*FF*	J_{SC} (mA·cm^{-2})	PCE_{avg}[a] (%)	PCE_{max} (%)
aBDT	0.81	0.27	1.74	0.4	0.5
BDT	0.85	0.49	8.67	3.6	3.9
BDF	0.83	0.50	8.97	3.7	3.9
NDT	0.84	0.43	11.1	4.0	4.1
zNDT	0.76	0.50	11.7	4.4	4.7

[a] PCE_{avg} calculated over 8 devices for aBDT and 12 devices for **BDT**, **BDF**, **NDT**, and **zNDT**.

The present OPVs exhibit a range of current-voltage (*J*-*V*) device response characteristics (Figure 4.11A). **aBDT** OPVs afford the lowest performance (PCE = 0.4%), limited principally by the low J_{sc} = 1.74 mA·cm^{-2} and *FF* = 0.27. **BDT** and **BDF** OPVs display comparable PCEs of 3.6 and 3.7 %, respectively, with **BDF** cells exhibiting a slightly higher J_{sc} = 8.97 mA·cm^{-2} and *FF* = 0.50. The π-extended **NDT**-based OPVs produce an enhanced PCE of 4.0% versus **BDF**- and **BDT**-based devices, with the primary enhancement arising from J_{sc} = 11.1 mA·cm^{-2}, but with a slight decrease in *FF* to 0.43. The highest efficiency devices are the **zNDT** cells having a respectable PCE = 4.4%, with a high J_{sc} = 11.7 mA·cm^{-2} and a moderate *FF* = 0.50. Overall, the EQEs scale with the observed J_{sc} values, exhibiting a broad photon-to-current efficiency response from 350–750 nm for the A-D-A-based cells (Figure 4.11B). However, due to the larger optical **aBDT** bandgap, only photons up to 690 nm are significantly absorbed. Note that the *FF*s of all of the small molecules in this series are uniformly low, suggesting that recombination processes limit cell efficiency, as seen in previous small-molecule studies.[79, 336, 337] That the PCEs exhibit a direct correlation with J_{sc} suggests that charge generation, charge extraction, and/or light absorption may well be limiting factors[18, 338] in the lower efficiency devices of this series.

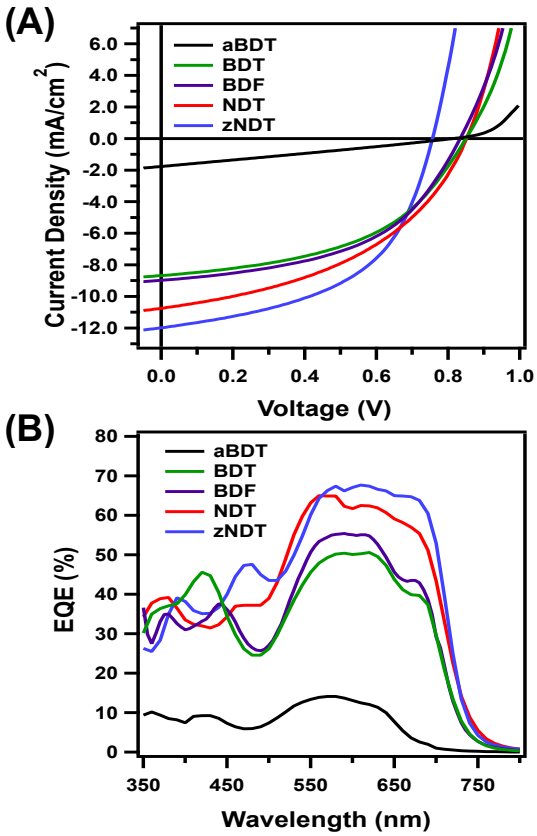

Figure 4.11. (A) *J-V* and (B) external quantum efficiency (EQE) response of optimized small-molecule:PCBM OPV devices

4.4 Discussion

We now analyze the result of three molecular structure variations: 1) π-conjugated backbone extension, 2) heteroatom replacement in the acenedithiophene core, and 3) reduction of the naphthodithiophene core aspect ratio. Specifically, we evaluate the effects of molecular structure variations on the crystal packing motif and density, and the carrier mobility in thin films. We then investigate the blend film morphology to analyze the small molecule + PCBM interactions and the impact on solar cell performance.

4.4.1 Single crystal and neat film crystal structures

The length of the conjugated backbone is almost doubled on going from **aBDT** to **BDT** with addition of a second thiophene-flanked DPP unit, and slightly extended further with the incorporation of the naphthodithiophene core in **NDT**. This extended π-conjugation affords the observed redshift in absorption onset in **BDT** and **NDT** relative to **aBDT** and increased molecular planarity as the backbone length increases. Note that the **aBDT** system exhibits twisting of the DPP unit relative to the core due to side chain steric interactions. With the additional DPP unit on **BDT**, torsion of the DPP moieties persists with respect to the core, but with the extended core in **NDT**, the terminal thiophene becomes more planar. The long lamellar stacking distance (20.3 Å for **NDT** versus 17.3 Å **BDT**) suggests that the side chains extend more perpendicularly from the **NDT** backbone than the **BDT** backbone thereby reducing the steric interaction between the sides chains on the naphthodithiophene core and the DPP units. The increased planarity of **NDT** does not affect the π–π stacking distance in the single crystal but does allow tighter π–π stacking in the neat film, which contributes to increased intermolecular

attraction in the **NDT** crystal relative to the **aBDT** and **BDT** as evidenced by the increased DSC melting temperature. We also find that the calculated co-facial coupling triples for **BDT** and **NDT** as compared to **aBDT** while the reorganization energy concurrently decreases, leading to a 100x increase in thin film mobility. By increasing the core length, the planarity of the **NDT** molecule is increased resulting in tighter crystal packing and leading to increased hole mobility.

When the linear **NDT** core is replaced by the zigzag naphthodithiophene core, the decreased **zNDT** aspect ratio results in increased π-orbital overlap and tighter π–π stacking. While only minor differences in optoelectronic characteristics are observed, **zNDT** exhibits the largest red-shift absorption onset on proceeding from solution to film, indicating the formation of strongly aggregated molecules in the thin film.[326] The absence of a **zNDT** DSC melting or crystallization feature further suggests that **zNDT** has the greatest intermolecular binding of the series. While the π–π stacking distance is comparable to linear **NDT**, the lamellar stacking is 3 Å smaller than **NDT** and comparable to the lamellar stacking distance observed in the **aBDT** single crystal. This tight **aBDT** lamellar packing is possible due to the side chain orientation parallel to the conjugated backbone, suggesting that the side chains in the **zNDT** crystal are similarly aligned. Furthermore, the **zNDT** mobility is highest in this series, arguing that co-facial coupling is strongest in **zNDT**, and that the reduced **zNDT** core aspect ratio enhances π-orbital overlap and hence, hole mobility.

4.4.2 Blend film morphology

The domain sizes and variations in small molecule *d*-spacings in films blended with PCBM provide insights into the small-molecule interactions with PCBM. While **aBDT** has large domains in the neat film, the lamellar domain size is halved with the PCBM incorporation,

suggesting that PCBM either disrupts **aBDT** crystal nucleation and/or that the weak intermolecular forces in the **aBDT** crystal structure prohibit **aBDT** crystal growth in the blend film. Despite the decreased domain size, the **aBDT** lamellar domain size remains significantly larger than the ~10 nm ideal as is clearly evident in the TEM images (Figure 4.8). **BDT** and **BDF** both display increased π–π stacked domain size and only a slight decrease in the number and intensity of diffraction rings with PCBM addition. This observation suggests that **BDT** and **BDF** have limited miscibility with PCBM, and that PCBM may even induce tighter **BDT** and **BDF** crystallite packing as evidenced by the decreased lamellar *d*-spacing in **BDF** crystals and decreased π-stacking *d*-spacing in **BDT** crystals in the blend films. In contrast, while **NDT** and **zNDT** are clearly less textured, there is little to no change in domain size or *d*-spacing, suggesting that PCBM disrupts small molecule crystallization and/or that these small molecules are more miscible with PCBM. Furthermore, **NDT** and **zNDT** form smaller domains in the blend films than do **BDT** or **BDF**, indicating sluggish nucleation or crystal growth. Because the **zNDT** and **NDT** core side chains are attached to neighboring aromatic rings, they do not have a plane of symmetry bisecting the donor (D) core like **BDT** and **BDF**. Therefore, the **NDT** and **zNDT** molecules can align in multiple spatial arrangements that are not conducive to single crystal growth. We hypothesize that the lower side chain appendage symmetry on the naphthodithiophene cores promotes mixed intermolecular arrangements, impedes nucleation, and leads to formation of smaller domains. [339]

4.4.3 *J-V* OPV characteristics

In this series, device PCE increases predominantly reflect increases in J_{sc}, while V_{oc} and *FF* remain constant across the A-D-A molecular series. Since J_{sc} is determined largely by the

solar cell light absorption and the efficiency of charge generation and collection, J_{sc} is low for **aBDT** due to the blue-shifted absorption relative to the symmetric molecules as well as to the larger domain sizes in thin films, and the low measured carrier mobility. Based on light absorption alone, one would expect J_{sc} to be equivalent for all of the A-D-A molecules, however OPVs with **zNDT** and **NDT** exhibit slightly higher J_{sc} values (~11 mA•cm^{-2}) vs **BDT** and **BDF**-based OPVs (~9.8 mA•cm^{-2}). The EQE trends mirror the J_{sc} trends, with ~68% for **zNDT** cells falling to 65-49% for **NDT**, **BDF**, and **BDT** cells. Therefore, either charge generation efficiency is low or bimolecular recombination is reducing the photogenerated current efficiency. To generate free charges, two conditions must be met: 1) the exciton must be close to a small-molecule–PCBM domain interface and 2) the energetic offset between the EA_{donor} and EA_{PCBM} must be sufficient to overcome the Coulombic force binding the electron and hole.[101] As discussed above, condition 2) is satisfied for all molecules in this series. To satisfy condition 1), the exciton must form near an interface or be able to diffuse to an interface before recombining. From the Scherrer analysis of the GIXS-derived lamellar and π–π stacking peak widths, we find that the lamellar domains of the **BDT** and **BDF** are ~18 nm and **zNDT** and **NDT** are ~14 nm, while the π–π stacked domains are ~11 nm for **BDT** and **BDF**, ~9 nm for **NDT**, and ~4 nm for **zNDT**. The smaller lamellar domain sizes in **zNDT** and **NDT** thin films increase interfacial area and increase the probability for charge generation, thereby increasing J_{sc}. However, the trend in π–π stacked domain size only weakly correlates with J_{sc}, suggesting that once a 10–11 nm small-molecule domain size is achieved, the great majority of excitons can diffuse to an interface to form free charges indicating that even with small domain sizes mutual percolation of the donor and PCBM domains persist.

Once free charges form, they can either recombine, resulting in decreased J_{sc}, or transit the donor/acceptor domains for collection at the electrodes to create current. Therefore, materials with larger hole mobilities should favor rapid hole transport and increased solar cell efficiencies, so the high mobility and small domain size of **zNDT** afford the highest J_{sc} in the series. Note also that the orientation of the crystals in the thin film impacts the measured mobility in the in-plane versus out-of-plane direction. In this series, the **zNDT** and **BDF** mobility from SCLC measurements is significantly larger than that of **NDT** or **BDT** due to the greater degree of face-on orientation, so that increased face-on preferential orientation likely contributes to J_{sc}.

In the present series, V_{oc} and *FF* are limited, as for many other small-molecule solar cells. [72, 109, 337, 340-342] Using the A_{EA}-D_{IP} energetic crossgap as the estimated theoretical maximum V_{oc}, we expect V_{oc} values here of ~1.13–1.23 V, while the experimental V_{oc} values are 0.76–0.85 V. It is reasonable to attribute the lower V_{oc}s here to non-ideal donor-PCBM molecular interfaces, [340, 343] as well as unfavorable vertical phase segregation evident in some annealed small-molecule systems. [344] The low *FFs* can be attributed to mismatched hole and electron mobilities, which is typically a result of low small-molecule hole mobilities in blend films.[345-347] Poor phase segregation can also lead to decreased charge generation and/or transport, [30] so that the small domain size in **NDT** blend films and the modest mobility may contribute to the reduced fill factor (*FF* = 0.43). Although **zNDT** domains are also very small and should favor increased recombination, the substantial hole mobility still supports the increased *FF* of 0.50.

4.5 Conclusion

In this study, we systematically compare a series of DPP-based π-conjugated small-molecule donors to determine the effects of molecular and crystal structure on optoelectronic properties, hole mobility, miscibility with PCBM, and the resulting solar cell efficiency. The D-A small molecule **aBDT** crystallizes in an antiparallel packing motif resulting in low π–π co-facial coupling, a high reorganization energy, and low hole mobility. By increasing the conjugation length with an additional DPP acceptor unit, the optical absorption spectrum is red-shifted and the molecular planarity increased, leading to decreased reorganization energy and increased π–π co-facial coupling as well as higher hole mobility. Next changing the central core from benzodithiophene to benzodifuran leads to an alteration in molecular planarity, but results in only a small enhancement in solar cell PCE to 3.7%. However, solar cells using the extended **NDT** exhibit a larger J_{sc} and PCE than **BDT** and **BDF** due to smaller NDT domain sizes in BHJ blend films with PCBM, which promotes increased small molecule–PCBM interfacial contact area for charge separation. Next, decreasing the molecular core aspect ratio with **zNDT** further increases the hole mobility, which is attributed to increased intermolecular cohesion and π–π co-facial overlap, affording the highest PCE of the series, 4.4%.

Despite the low crystallinity and small BHJ domain size of the **zNDT** blend films, the relatively high PCE performance reflects the high out-of-plane hole mobility as a result of strong intermolecular cohesive forces and high π–π co-facial coupling connected with the decreased aspect ratio of the zigzag core. We have demonstrated here that intermolecular cohesive forces and hole mobility increase with the lower aspect ratio core of **zNDT**, but note that **zNDT** is not

very crystalline, leading to small phase-segregated domains in the thin film which in turn limit the *FF*.

By systematically studying this series of small molecule donors, we have demonstrated the following general structure-property relationships relating the size and shape of the aromatic core to the coupling constant and hole mobility via the crystal structure and crystal orientation in thin film. As the core conjugation length is increased, the π-π co-facial coupling constant increases leading to improved hole mobility parallel to the π-stacking axis of the crystal structure. In addition, as the core aspect ratio is decreased, the attractive intermolecular forces increase and the crystal structure packing becomes tighter, again leading to enhanced hole mobility. We also suggest that the side chains orientated parallel to the molecular backbone allow for tighter crystal packing and that side chain attachment resulting in decreased molecular symmetry leads to the formation of smaller crystalline domains in the thin film.

To further enhance the performance of this series of small-molecule donors, it will be necessary to increase the crystallinity and domain sizes in the blend films in order to increase the hole mobility. Given the performance increases in the naphthodithiophene-based solar cells, it will be beneficial to continue to explore alternative donor cores with reduced aspect ratios and/or extended π-conjugation to maximize π-π co-facial coupling and hole mobility. Stronger intermolecular cohesion may also result in larger domain sizes in the thin films to reduce charge recombination. Larger domain sizes and enhanced crystallinity may also be obtained by developing donor cores that permit symmetrical side-chain attachment to avoid the nucleation impediments found in the naphthodithiophene cores versus the benzodithiophene cores.

Appendix A. Supplemental Materials for Effects of 1,8 Diiodooctane on Domain Nanostructure and Charge Separation Dynamics in $PC_{71}BM$-Based Bulk Heterojunction Solar Cells

A.1. Solar cell external quantum efficiency data

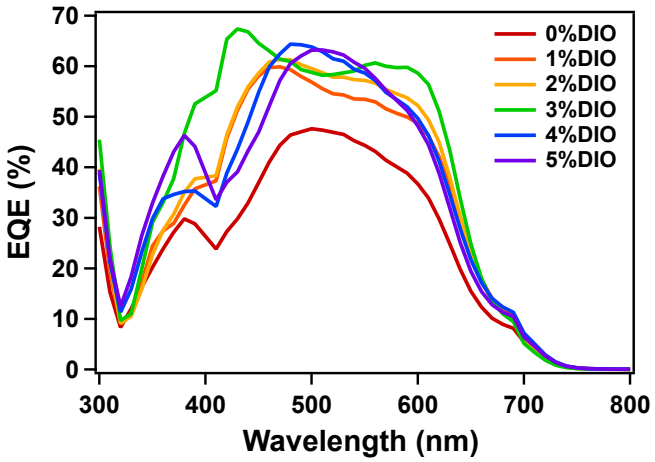

Figure A.1. External quantum efficiencies of PBTIBDT:PCBM solar cells with 0-5 vol% DIO added to the active layer solution

A.2. Small angle x-ray scattering component fits for PBTIBDT+PCBM solutions with 0-5 vol% DIO

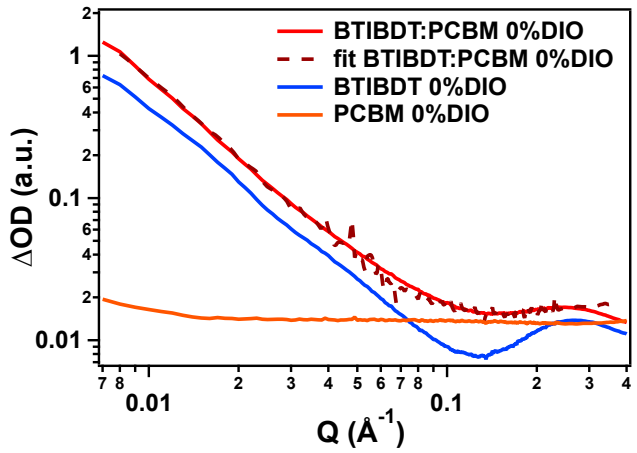

Figure A.2. Representative fits of PBTIBDT+PCBM solution data with 0 vol% DIO

Table A.1. Table of small angle x-ray scattering component fit percentages

[DIO] (vol%)	**Percentage of each component**	
	PCBM	PBTIBDT
0	6	94
1	5	95
2	5	95
3	3	97
4	4	96
5	4	96

A.3. GIWAXS data analysis procedures and 2D images

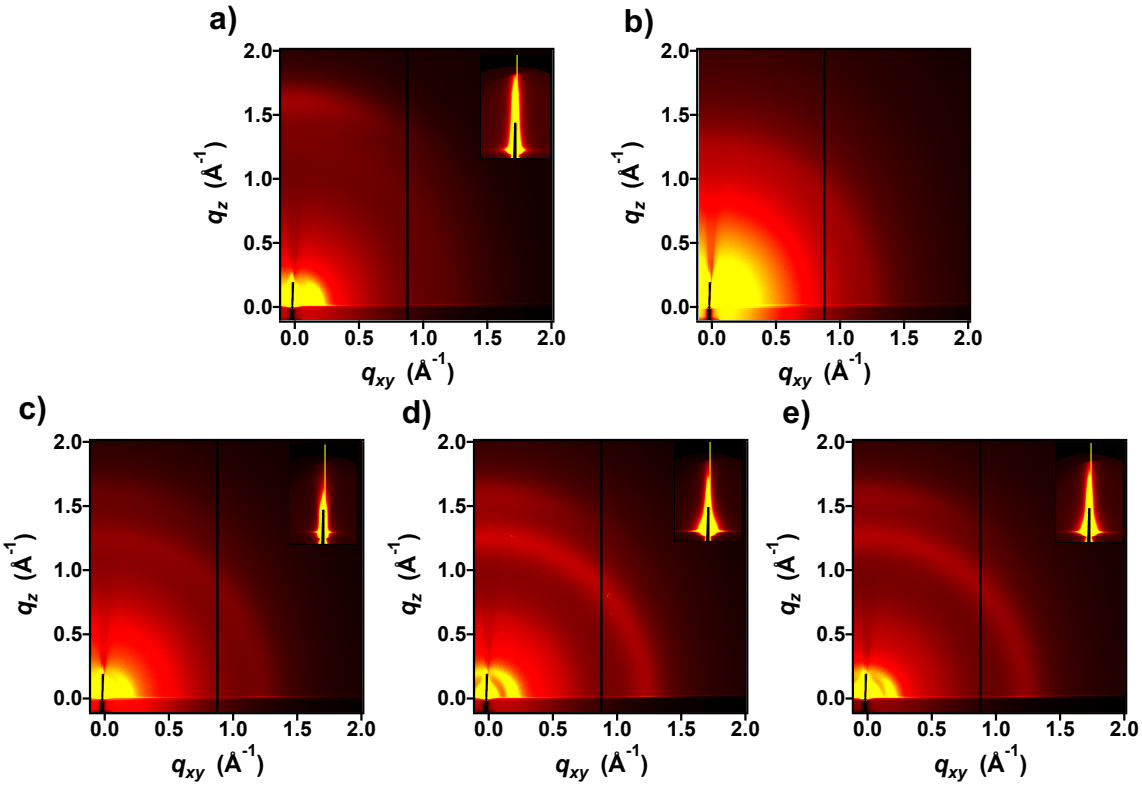

Figure A.3 2D GIWAXS images of neat films of a) PBTIBDT 0% DIO and b) PCBM and blend PBTIBDT:PCBM films with: c) 0 vol % DIO, d) 3 vol% DIO, e) 5 vol% DIO

Linecuts were taken parallel to the horizontal (q_{xy}) and vertical (q_z) axes to approximate the in-plane and out-of-plane structure of the polymer, respectively (Figure S4). The background was subtracted by fitting the trace to an exponential decay and the peaks in the resulting trace were fit using 2-5 Gaussians, depending on the trace studied. One Gaussian was always used to fit the amorphous scattering feature from the substrate which has somewhat variable intensity in each scan.

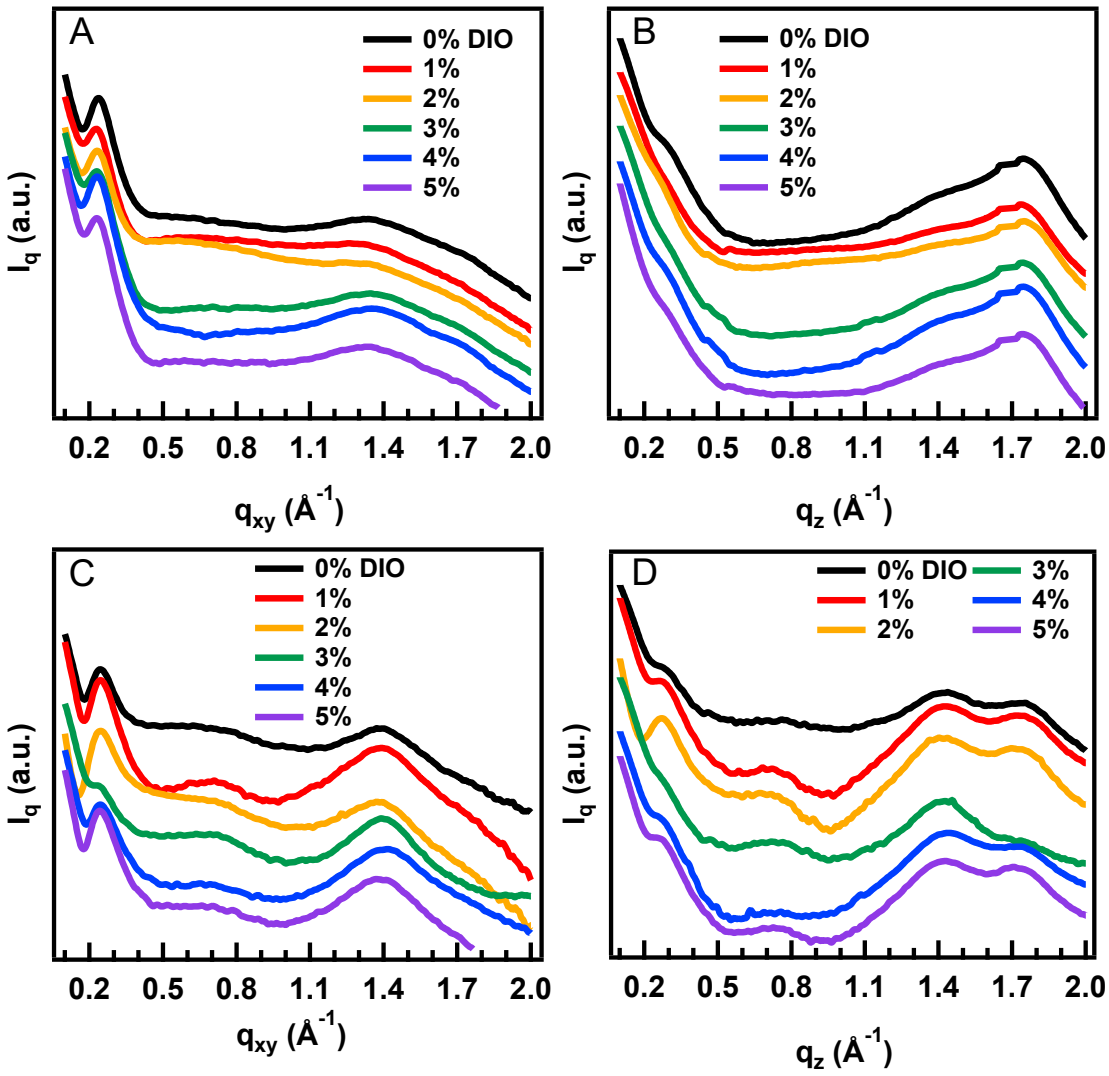

Figure A.4. GIWAXS linecuts along the horizontal and vertical axes of the 2D images showing the crystal structure of A) neat PBTIBDT films with 0-5 vol % DIO in-plane and B) neat PBTIBDT films with 0-5 vol% DIO out of plane and C) PBTIBDT:PCBM films with 0-5 vol % DIO in-plane and PBTIBDT:PCBM films with 0-5vol % DIO out of plane.

Table A.2. GIWAXS d-spacings of PBTIBDT and PCBM domains in neat and blend thin films as a function of vol% DIO.

DIO (vol %)	PBTIBDT lamellar (neat) (Å)	PBTIBDT π-π (neat) (Å)	PBTIBDT lamellar (blend) (Å)	PBTIBDT π-π (blend) (Å)	PCBM (neat) (Å)	PCBM (blend) (Å)
0	26.2	3.6	25.5	3.6	4.5	4.5
1	27.7	3.6	25.2	3.6	4.5	4.5
2	26.8	3.6	25.5	3.7	4.5	4.5
3	27.6	3.6	27.5	3.7	4.5	4.5
4	27.2	3.6	25.1	3.7	4.6	4.4
5	27.7	3.6	25.3	3.6	4.5	4.5

A.4. Optical transient absorption within 3 ns delay time window, and fitting parameters for exciton absorption and ground state bleach

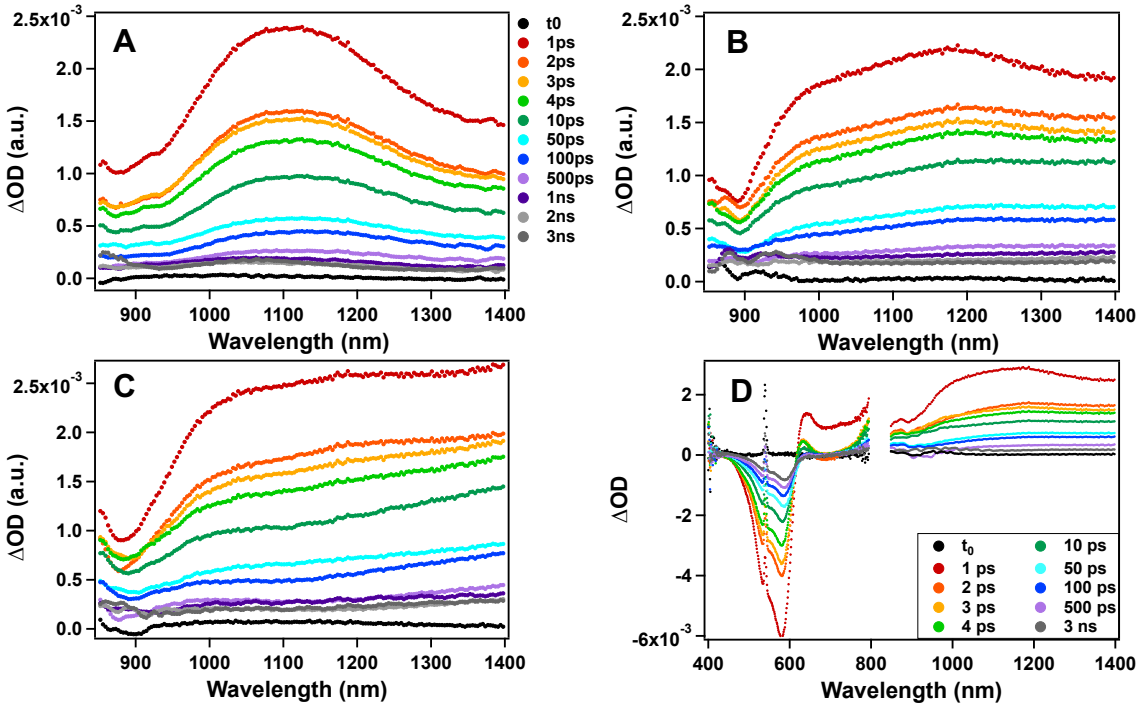

Figure A.5. Time delays of A) neat PBTIBDT film with 0 vol% DIO and B) PBTIBDT:PCBM blend film with 0 vol% DIO and C) 5 vol% DIO and D) PBTIBDT:PCBM blend film with 3 vol% DIO illustrating the entire visible and near IR spectra.

Table A.3. Exciton dynamics of PBTIBDT:PCBM blend films

[DIO] (vol %)	τ1 (ps)	τ2 (ps)	τ3 (ps)[a]	τ4 (ps)	A1 (%)	A2 (%)	A3 (%)	A4 (%)
0	0.48 (0.01)	4.3 (0.2)	82.8 (10.8)	>3000	57 (3)	15 (2)	22 (1)	6 (0)
1	0.56 (0.03)	5.0 (0.6)	63.8 (11.4)	>3000	64 (4)	8 (3)	22 (2)	6 (0)
2	0.76 (0.04)	4.8 (0.6)	84.3 (20.3)	>3000	59 (6)	11 (4)	22 (2)	8 (1)
3	0.61 (0.03)	5.2 (0.7)	62.6 (17.0)	>3000	61 (5)	10 (4)	21 (2)	8 (1)
4	0.29 (0.01)	3.4 (0.2)	86.7 (9.9)	>3000	70 (3)	12 (1)	13 (1)	4 (0)
5	0.54 (0.02)	4.3 (0.5)	53.6 (10.2)	>3000	64 (4)	10 (3)	20 (2)	6 (0)

[a] Attributed to CAT decay due to overlap of CAT and EX peaks.

Error in fit is noted in parentheses.

Table A.4. Ground state bleach dynamics of PBTIBDT:PCBM blend films

[DIO] (vol %)	τ1 (ps)	τ2 (ps)	τ3 (ps)	τ4 (ps)	A1 (%)	A2 (%)	A3 (%)	A4 (%)
0	0.48 (0.01)	4.3 (0.2)	97 (8)	>3000	66 (1)	20 (1)	10 (0)	4 (0)
1	0.56 (0.03)	5.0 (0.6)	92 (10)	>3000	64 (1)	18 (1)	10 (1)	8 (0)
2	0.76 (0.04)	4.8 (0.6)	70 (10)	>3000	67 (2)	21 (2)	6 (1)	6 (0)
3	0.61 (0.03)	5.2 (0.7)	65 (11)	>3000	70 (1)	18 (1)	6 (1)	6 (0)
4	0.29 (0.01)	3.4 (0.2)	71 (5)	>3000	72 (1)	16 (0)	7 (0)	5 (0)
5	0.54 (0.02)	4.3 (0.5)	50 (8)	>3000	76 (1)	16 (1)	4 (1)	4 (0)

Error in fit is noted in parentheses.

Table A.5. Dynamics of neat PBTIBDT films

		τ1 (ps)	**τ2 (ps)**	**τ3 (ps)**	**A1 (%)**	**A2 (%)**	**A3 (%)**	**A4 (%)**
0 vol % DIO	CS	0.39 (0.01)	NA	60.6 (10.0)	71 (9)	NA	26 (2)	3 (1)
	EX	0.39 (0.01)	4.3 (0.3)	NA	73 (4)	20 (2)	NA	7 (0)
	GSB	0.39 (0.01)	4.3 (0.3)	60.6 (10.0)	79 (1)	14 (0)	4 (0)	3 (0)
5 vol % DIO	CS	0.24 (0)	NA	68.2 (3.8)	69 (2)	NA	23 (1)	7 (0)
	EX	0.24 (0)	6.3 (0.4)	NA	70 (2)	26 (1)	NA	4 (0)

Error in fit is noted in parentheses.

A.5. Nanosecond transient absorption spectroscopy

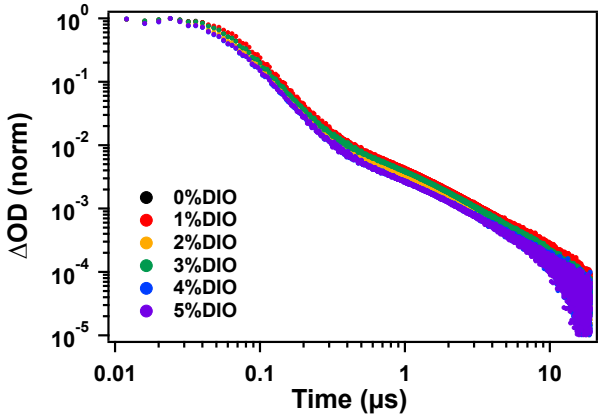

Figure A.6. Decay of cation species at 1070 nm in PBTIBDT:PCBM films as a function of vol % DIO normalized at the highest intensity

Appendix B. Supplemental Materials for Systematic Evaluation of Structure-Property Relationships in Heteroacene-Diketopyrrolopyrrole Molecular Donors for Organic Solar Cells

B.1. Single crystal x-ray diffraction

Single crystals of BDT(TDPP)$_2$ were recrystallized from anhydrous chloroform, mounted in inert oil, and transferred to the cold gas stream of a Bruker D8 goniometer with APEXII CCD detector equipped with a synchrotron with Silicon (111)&(311). SADABS-2008/1 (Bruker, 2008) was used for absorption correction.

Single crystals of BDF(TDPP)$_2$ were recrystallized from anhydrous chloroform, mounted in inert oil, and transferred to the cold gas stream of a Bruker Apex2 equipped with a synchrotron with Silicon (111). SADABS-2012/1 (Bruker, 2012) was used for absorption correction.

Single crystals of BDTTDPP were recrystallized from CHCl3/EtOAc, mounted in inert oil, and transferred to the cold gas stream of a Bruker Kappa APEX CCD area detector equipped with a CuKα microsource with MX optics. SADABS-2008/1 (Bruker, 2008) was used for absorption correction.

A brown needle crystal of NDT(TDPP)$_2$ having approximate dimensions of 0.43 x 0.02 x 0.02 mm was mounted using oil (Infineum V8512) on a glass fiber. All measurements were made on a Bruker APEX-II CCD Diffractometer with a CuKα IuS source. Data were collected using Bruker APEX2 detector and processed using SAINTPLUS from Bruker.

Table B.1. Unit cell parameters and structure solution details

Compound	BDTTDPP	$BDT(TDPP)_2$	$BDF(TDPP)_2$	$NDT(TDPP)_2$
Empirical formula	$C_{56}H_{76}N_2O_4S_4$	$C_{86}H_{114}N_4O_6S_6$	$C_{86}H_{114}N_4O_8S_4$	$C_{90}H_{116}N_4O_6S_6$
Temperature (K)	100.01	100.15	100	100 (2)
Morphology	Needle	Needle	Needle	Needle
Color	purple	brown	brown	brown
Crystal system	Monoclinic	Monoclinic	Monoclinic	Triclinic
Space group	P 2_1/c	C 2/c	C 2/c	P -1
a (Å)	15.2482(3)	33.287(11)	33.795 (2)	6.3929(5)
b (Å)	10.0758(2)	5.6052(19)	5.449(3)	17.4732(13)
c (Å)	34.5945(8)	45.613(15)	45.61(2)	18.4977(15)
α (°)	90	90	90	90.241(6)
β (°)	97.579(2)	10.234(5)	111.75	93.609(6)
γ (°)	90	90	90	97.132(6)
Molecular length (Å)	19.380	31.807	31.361	34.417
Z	4	4	4	1
Density (g/cm^3)	1.222	1.241	1.243	1.252
Volume ($Å^3$)	5268.59	7985.32	7787.45	2046.07
Void space (%)	2.9	11.3	6.8	4.6
R1 (%)	15.90	25.87	22.14	9.32
wR2 (%)	34.20	52.78	41.58	25.79
GOF	1.177	2.098	1.470	1.083

B.2. Comparison of single crystal structure and film crystal structure

Table B.2. Comparison of peaks from calculated powder diffraction and fitting of GIWAXS scattering traces for BDTTDPP. [a]Denotes peaks used to measure the lamellar *d*-spacing in thin film and [b]denotes peaks used to measure the π-π *d*-spacing in thin film. Peaks along the q_z axis are noted in bold.

BDTTDPP		
hkl	Powder	GIWAXS
(002)[a]	0.37	0.37
(100)	0.42	**0.43**
(10-2)	0.52	NA
(103)	0.73	0.72
(10-4)	0.79	**0.83**
(201)	0.86	0.84
(113)	0.96	0.96
(210)	1.04	NA
(10-6)	1.12	1.10
(30-2)	1.23	NA
(020)	1.25	**1.24**
(311) *(21-6)*	1.43	1.40
(10-8) *(008)*[b]	1.47	1.46
(22-3)	1.56	1.56
(125)	1.63	1.66, **1.67**
(223)	1.71	NA
(315)	1.76	NA
(225)	1.81	1.78

Table B.3. Comparison of peaks from calculated powder diffraction and fitting of GIWAXS scattering traces for $BDT(TDPP)_2$. [a]Denotes peaks used to measure the lamellar *d*-spacing in thin film and [b]denotes peaks used to measure the π-π *d*-spacing in thin film. Peaks along the q_z axis are noted in bold.

$BDT(TDPP)_2$		
hkl	Powder	GIWAXS
(020)[a]	0.40	0.39, **0.37**
(200)	0.58	**0.51**
(004) *(202)*	0.75	**0.77**
(400)	0.81	NA
(006)	0.88	0.88, **0.89**
(40-6) *(402)*	0.95	NA
(404) *(60-4)* *(60-2)*	1.15	1.10, **1.17**
(113)	1.24	1.27, **1.27**
(312) *(602)*	1.35	1.39
(116)	1.49	1.48
(117)[b] *(11-8)*	1.59	1.59
(118)	1.68	1.68

Table B.4. Comparison of peaks from calculated powder diffraction and fitting of GIWAXS scattering traces for $BDF(TDPP)_2$. [a]Denotes peaks used to measure the lamellar *d*-spacing in thin film and [b]denotes peaks used to measure the π-π *d*-spacing in thin film. Peaks along the q_z axis are noted in bold.

$BDF(TDPP)_2$		
hkl	Powder	GIWAXS
(200)[a]	0.40	0.40, **0.37**
(005)	0.58	NA
(40-2)	0.74	**0.76**
(40-4)	0.80	NA
(400)	0.83	NA
(20-6) *(204)*	0.89	0.89, **0.91**
(402) *(40-6)*	0.95	NA
(20-8) *(206)*	1.11	1.11
(60-4) *(60-2)*	1.13	**1.17**
(600) *(60-6)*	1.20	NA
(11-3)	1.23	1.25, **1.27**
(602)	1.34	NA
(80-4) *(51-2)*[b] *(51-3)*	1.48	1.48, **1.43**
(51-5) *(314)* *(80-2)*	1.52	NA
(31-5)	1.57	NA
(117)	1.62	1.60

Table B.5. Comparison of peaks from calculated powder diffraction and fitting of GIWAXS scattering traces for NDT(TDPP)$_2$. [a]Denotes peaks used to measure the lamellar *d*-spacing in thin film and [b]denotes peaks used to measure the π-π *d*-spacing in thin film. Peaks along the q_z axis are noted in bold.

NDT(TDPP)$_2$		
hkl	Powder	GIWAXS
(001)[a] *(010)*	0.36	0.40, **0.38**
(011) *(01-1)*	0.49	**0.53**
(012) *(021)*	0.78	0.85, **0.78, 0.88**
(003)	1.02	1.06
(1-2-1)	1.22	**1.18**
(03-2) *(023)* *(1-12)* *(102)*	1.25	1.28, **1.28**
(1-13) *(03-3)* *(041)* *(033)* *(1-2-3)*	1.50	1.50
(1-40)[b] *(1-1-4)*	1.65	1.64

B.3. OFET and SCLC mobility measurements

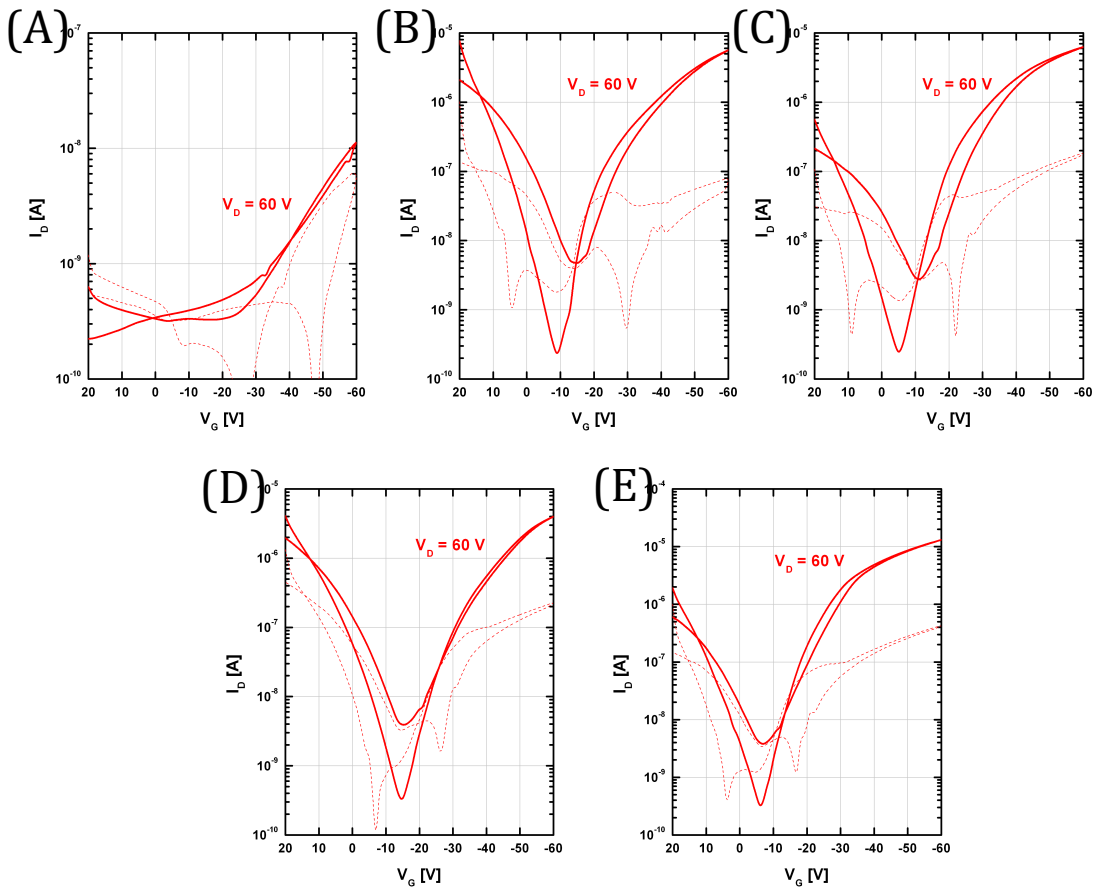

Figure B.1. Typical transfer plots of neat films of (A) **BDTTDPP**, (B) **BDT(TDPP)$_2$**, (C) **BDF(TDPP)$_2$**, (D) **NDT(TDPP)$_2$**, and (E) **zNDT(TDPP)$_2$**

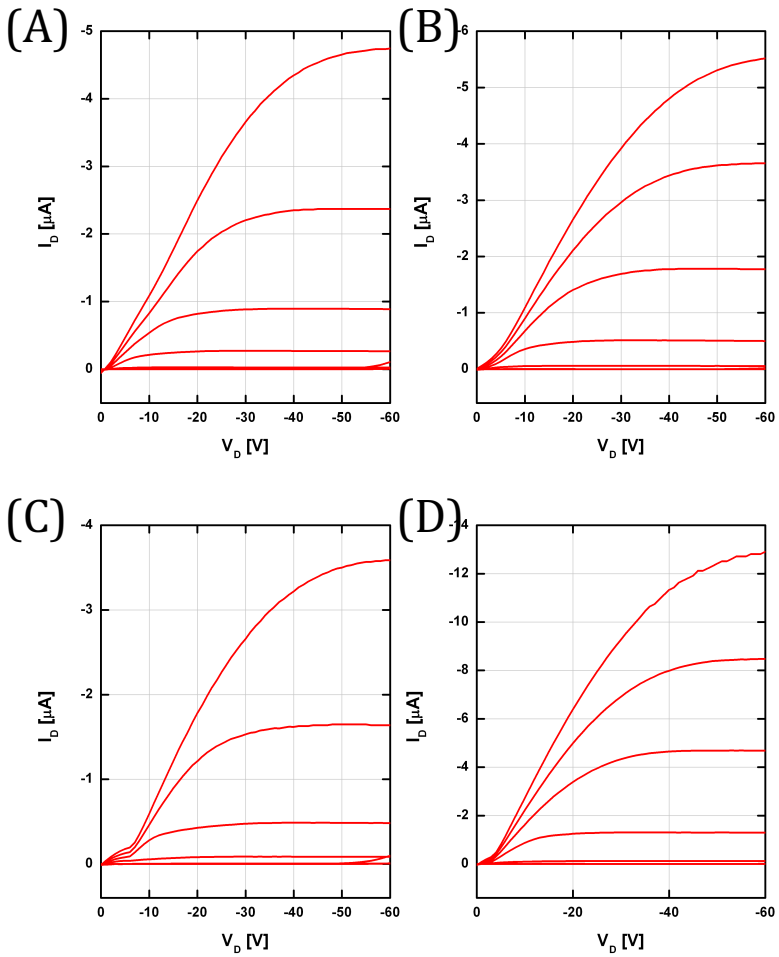

Figure B.2. Typical output plots of neat films of (A) **BDT(TDPP)$_2$**, (B) **BDF(TDPP)$_2$**, (C) **NDT(TDPP)$_2$**, and (D) **zNDT(TDPP)$_2$**

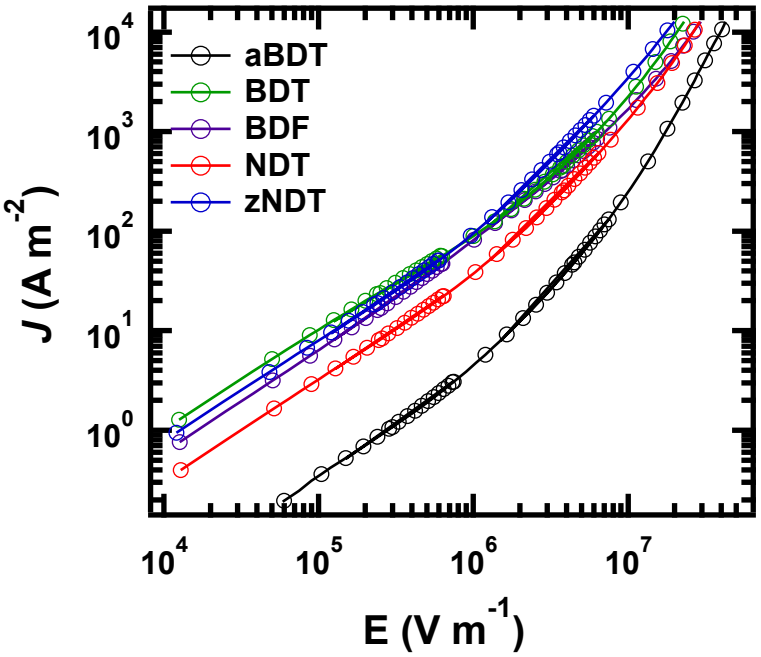

Figure B.3. J-E response data and fits describing the SCLC mobilities in small molecule donor neat films.

References

(1) Team, G., 2018: *GISS Surface Temperature Analysis (GISTEMP)* NASA Goddard Institute for Space Studies. Dataset accessed 2018-07-20 at https://data.giss.nasa.gov/gistemp/

(2) Hansen, J.; Ruedy, R.; Sato, M.; Lo, K., *Rev. Geophys.* **2010,** *48*, RG4004.

(3) IPCC, 2014: *Climate Change 2014: Synthesis Report. Contribution of Working Groups I, II, and III to the Fifth Assessment Report of the Intergovernmental Panel on Climate Change [Core Writing Team, R. K. Pachauri and L.A. Meyer (eds.)]*. IPCC, Geneva, Switzerland, p 151 In IPCC AR5 Synthesis Report website.

(4) Church, J. A.; White, N. J., *Geophys. Res. Lett.* **2006,** *33*, L01602.

(5) National Academies of Sciences, E. a. M., Attribution of Extreme Weather Events in the Context of Climate Change. National Academies Press: Washington, DC, 2016. https://books.google.com/books?id=WWEpDQAAQBAJ.

(6) Kunkel, K. E.; Karl, T. R.; Easterling, D. R.; Redmond, K.; Young, J.; Yin, X.; Hennon, P., *Geophys. Res. Lett.* **2013,** *40*, 1402-1408.

(7) John, C.; Naomi, O.; Peter, T. D.; William, R. L. A.; Bart, V.; Ed, W. M.; Carlton, J. S.; Stephan, L.; Andrew, G. S.; Sarah, A. G.; Dana, N.; Peter, J.; Mark, R.; Bärbel, W.; Rob, P.; Ken, R., *Environ. Res. Lett.* **2016,** *11*, 048002.

(8) Boden, T. A.; Andres, R. J.; Marland, G., 2013: *Global, Regional, and National Fossil-Fuel CO2 Emissions (1751 - 2010) (V. 2013)* Carbon Dioxide Information Analysis Center (CDIAC); Oak Ridge National Laboratory (ORNL); Oak Ridge, T. N., (United States)

Dataset accessed 2018-07-22 at http://cdiac.ess-dive.lbl.gov/trends/emis/overview_2010.html

(9) Ribeiro, S. K.; Kobayashi, S.; Beuthe, M.; Gasca, J.; Greene, D.; Lee, D. S.; Muromachi, Y.; Newton, P. J.; Plotkin, S.; Sperling, D.; Wit, R.; Zhou, P. J., Transport and its infrastructure. In *Climate Change 2007: Mitigation. Contribution of Working Group III to the Fourth Assessment Report of the Intergovenmental Panel on Climate Change [B. Metz., O.R. Davidson, P.R. Bosch, R. Dave, LA. Meyer (eds)]*, Cambridge University Press: Cambridge, United Kingdom and New York, NY, USA, 2007.

(10) Tsao, J.; Lewis, N.; Crabtree, G. Solar FAQs 2006, p. 1-24. http://www.sandia.gov/~jytsao/Solar FAQs.pdf.

(11) Jean, J.; Brown, P. R.; Jaffe, R. L.; Buonassisi, T.; Bulović, V., *Energ. Environ. Sci.* **2015,** *8*, 1200-1219.

(12) Almosni, S.; Delamarre, A.; Jehl, Z.; Suchet, D.; Cojocaru, L.; Giteau, M.; Behaghel, B.; Julian, A.; Ibrahim, C.; Tatry, L.; Wang, H.; Kubo, T.; Uchida, S.; Segawa, H.; Miyashita, N.; Tamaki, R.; Shoji, Y.; Yoshida, K.; Ahsan, N.; Watanabe, K.; Inoue, T.; Sugiyama, M.; Nakano, Y.; Hamamura, T.; Toupance, T.; Olivier, C.; Chambon, S.; Vignau, L.; Geffroy, C.; Cloutet, E.; Hadziioannou, G.; Cavassilas, N.; Rale, P.; Cattoni, A.; Collin, S.; Gibelli, F.; Paire, M.; Lombez, L.; Aureau, D.; Bouttemy, M.; Etcheberry, A.; Okada, Y.; Guillemoles, J.-F., *Sci. Technol. Adv. Mat.* **2018,** *19*, 336-369.

(13) Green Martin, A.; Hishikawa, Y.; Dunlop Ewan, D.; Levi Dean, H.; Hohl-Ebinger, J.; Ho-Baillie Anita, W. Y., *Prog. Photovoltaics* **2017,** *26*, 3-12.

(14) Candelise, C.; Winskel, M.; Gross, R., **2012,** *20*, 816-831.

(15) Tang, C. W., *Appl. Phys. Lett.* **1986,** *48*, 183-185.

(16) Kearns, D.; Calvin, M., *J. Chem. Phys.* **1958,** *29*, 950-951.

(17) Armantas, M.; Vytenis, P.; Donato, S.; Johannes, B.; Olle, I.; Vidmantas, G.; Koen, V.; Martijn, K., *Adv. Energy Mater.* **2017,** *7*, 1700888.

(18) Heeger, A. J., *Adv. Mater.* **2014,** *26*, 10-28.

(19) Che, X.; Li, Y.; Qu, Y.; Forrest, S. R., *Nat. Energy* **2018,** *3*, 422-427.

(20) Hosoya, M.; Oooka, H.; Nakao, H.; Gotanda, T.; Mori, S.; Shida, N.; Hayase, R.; Nakano, Y.; Saito, M. In *Organic thin film photovoltaic modules*, Proceedings of the 93rd Annual Meeting of the Chemical Society of Japan, 2013; pp 21-37.

(21) Tamai, Y.; Ohkita, H.; Benten, H.; Ito, S., *J. Phys. Chem. Lett.* **2015,** *6*, 3417-3428.

(22) Hoppe, H.; Sariciftci, N. S., *J. Mater. Chem.* **2006,** *16*, 45-61.

(23) Credgington, D.; Kim, Y.; Labram, J.; Anthopoulos, T. D.; Durrant, J. R., **2011,** *2*, 2759.

(24) Yu, G.; Gao, J.; Hummelen, J. C.; Wudl, F.; Heeger, A. J., *Science* **1995,** *270*, 1789-1791.

(25) Dennler, G.; Scharber, M. C.; Brabec, C. J., *Adv. Mater.* **2009,** *21*, 1323-1338.

(26) Hoppe, H.; Sariciftci, N. S., *J. Mater. Res.* **2004,** *19*, 1924-1945.

(27) Yi, Z.; Ni, W.; Zhang, Q.; Li, M. M.; Kan, B.; Wan, X. J.; Chen, Y. S., *J. Mater. Chem. C* **2014,** *2*, 7247-7255.

(28) Lilliu, S.; Agostinelli, T.; Verploegen, E.; Pires, E.; Hampton, M.; Al-Hashimi, M.; Heeney, M. J.; Toney, M. F.; Nelson, J.; Macdonald, J. E., *Macromol. Rapid Comm.* **2011,** *32*, 1454-1460.

(29) Verploegen, E.; Mondal, R.; Bettinger, C. J.; Sok, S.; Toney, M. F.; Bao, Z., *Adv. Funct. Mater.* **2010,** *20*, 3519-3529.

(30) Agostinelli, T.; Lilliu, S.; Labram, J. G.; Campoy-Quiles, M.; Hampton, M.; Pires, E.; Rawle, J.; Bikondoa, O.; Bradley, D. D. C.; Anthopoulos, T. D.; Nelson, J.; Macdonald, J. E., *Adv. Funct. Mater.* **2011,** *21*, 1701-1708.

(31) Sharma, A.; Pan, X.; Campbell, J. A.; Andersson, M. R.; Lewis, D. A., *Macromolecules* **2017,** *50*, 3347-3354.

(32) Kumar, C. V.; Cabau, L.; Viterisi, A.; Biswas, S.; Sharma, G. D.; Palomares, E., *J. Phys. Chem. C* **2015,** *119*, 20871-20879.

(33) He, Z.; Liu, F.; Wang, C.; Chen, J.; He, L.; Nordlund, D.; Wu, H.; Russell, T. P.; Cao, Y., *Mater. Horiz.* **2015,** *2*, 592-597.

(34) Li, G.; Yao, Y.; Yang, H.; Shrotriya, V.; Yang, G.; Yang, Y., *Adv. Funct. Mater.* **2007,** *17*, 1636-1644.

(35) Kyaw, A. K. K.; Wang, D. H.; Luo, C.; Cao, Y.; Nguyen, T.-Q.; Bazan, G. C.; Heeger, A. J., *Adv. Energy Mater.* **2014,** *4*, 1301469-n/a.

(36) Graham, K. R.; Wieruszewski, P. M.; Stalder, R.; Hartel, M. J.; Mei, J. G.; So, F.; Reynolds, J. R., *Adv. Funct. Mater.* **2012,** *22*, 4801-4813.

(37) Rogers, J. T.; Schmidt, K.; Toney, M. F.; Kramer, E. J.; Bazan, G. C., *Adv. Mater.* **2011,** *23*, 2284-2288.

(38) Choi Won, T.; Song, J.; Ko, J.; Jang, Y.; Kim, T.-H.; Han, Y.-S.; Lim, J.; Lee, C.; Char, K., *J. Polym. Sci. Pol. Phys.* **2015,** *54*, 128-134.

(39) Dimitrov, S. D.; Durrant, J. R., *Chem. Mater.* **2014,** *26*, 616-630.

(40) Kniepert, J.; Lange, I.; van der Kaap, N. J.; Koster, L. J. A.; Neher, D., *Adv. Energy Mater.* **2014,** *4*, 1301401-n/a.

(41) Yan, H.; Zhu, L. Y.; Li, D. H.; Zhang, Y. J.; Yi, Y. P.; Yang, Y. L.; Wei, Z. X.; Bredas, J. L., *J. Phys. Chem. C* **2014,** *118*, 29473-29481.

(42) Sharenko, A.; Kuik, M.; Toney, M. F.; Nguyen, T. Q., *Adv. Funct. Mater.* **2014,** *24*, 3543-3550.

(43) Berger, P. R.; Kim, M., *J. Renew. Sustain. Energy* **2018,** *10*.

(44) Cheng, Y. J.; Yang, S. H.; Hsu, C. S., *Chem. Rev.* **2009,** *109*, 5868-5923.

(45) Liang, Y. Y.; Yu, L. P., *Accounts Chem. Res.* **2010,** *43*, 1227-1236.

(46) Facchetti, A., *Chem. Mater.* **2011,** *23*, 733-758.

(47) Duan, C.; Huang, F.; Cao, Y., *J. Mater. Chem.* **2012,** *22*, 10416-10434.

(48) Liang, Y.; Xu, Z.; Xia, J. B.; Tsai, S. T.; Wu, Y.; Li, G.; Ray, C.; Yu, L. P., *Adv. Mater.* **2010,** *22*, E135-E138.

(49) Zhao, W.; Li, S.; Yao, H.; Zhang, S.; Zhang, Y.; Yang, B.; Hou, J., *J. Am. Chem. Soc.* **2017,** *139*, 7148-7151.

(50) Wenchao, Z.; Sunsun, L.; Shaoqing, Z.; Xiaoyu, L.; Jianhui, H., **2017,** *29*, 1604059.

(51) Park, S. H.; Roy, A.; Beaupre, S.; Cho, S.; Coates, N.; Moon, J. S.; Moses, D.; Leclerc, M.; Lee, K.; Heeger, A. J., *Nature Photon.* **2009,** *3*, 297-303.

(52) Guo, X.; Zhou, N.; Lou, S. J.; Smith, J.; Tice, D. B.; Hennek, J. W.; Ortiz, R. P.; Navarrete, J. T. L.; Li, S.; Strzalka, J.; Chen, L. X.; Chang, R. P. H.; Facchetti, A.; Marks, T. J., *Nat. Photon* **2013**, DOI: 10.1038/nphoton.2013.207.

(53) Kaake, L.; Dang, X. D.; Leong, W. L.; Zhang, Y.; Heeger, A.; Nguyen, T. Q., *Adv. Mater.* **2013,** *25*, 1706-1712.

(54) Curtin, I. J.; Blaylock, D. W.; Holmes, R. J., *Appl. Phys. Lett.* **2016,** *108*, 163301.

(55) Muller, C.; Wang, E. G.; Andersson, L. M.; Tvingstedt, K.; Zhou, Y.; Andersson, M. R.; Inganas, O., *Adv. Funct. Mater.* **2010,** *20*, 2124-2131.

(56) Demeter, D.; Mohamed, S.; Diac, A.; Grosu, I.; Roncali, J., *Chemsuschem* **2014,** *7*, 1046-1050.

(57) Mishra, A.; Bauerle, P., *Angew. Chem., Int. Ed.* **2012,** *51*, 2020-2067.

(58) Bredas, J. L., *Science* **2014,** *343*, 492-493.

(59) Wunsch, B. H.; Rumi, M.; Tummala, N. R.; Risko, C.; Kang, D. Y.; Steirer, K. X.; Gantz, J.; Said, M.; Armstrong, N. R.; Bredas, J. L.; Bucknall, D.; Marder, S. R., *J. Mater. Chem. C* **2013,** *1*, 5250-5260.

(60) Collins, S. D.; Ran, N. A.; Heiber, M. C.; Nguyen, T.-Q., *Adv. Energy Mater.* **2017**, 1602242.

(61) Logsdon, J. L.; Hartnett, P. E.; Nelson, J. N.; Harris, M. A.; Marks, T. J.; Wasielewski, M. R., *ACS Appl. Mater. Inter.* **2017,** *9*, 33493-33503.

(62) Kyaw, A. K. K.; Gehrig, D.; Zhang, J.; Huang, Y.; Bazan, G. C.; Laquai, F.; Nguyen, T. Q., *J. Mater. Chem. A* **2015,** *3*, 1530-1539.

(63) Hartnett, P. E.; Mauck, C. M.; Harris, M. A.; Young, R. M.; Wu, Y. L.; Marks, T. J.; Wasielewski, M. R., *J. Am. Chem. Soc.* **2017,** *139*, 749-756.

(64) Kan, B.; Li, M. M.; Zhang, Q.; Liu, F.; Wan, X. J.; Wang, Y. C.; Ni, W.; Long, G. K.; Yang, X.; Feng, H. R.; Zuo, Y.; Zhang, M. T.; Huang, F.; Cao, Y.; Russell, T. P.; Chen, Y. S., *J. Am. Chem. Soc.* **2015,** *137*, 3886-3893.

(65) Kan, B.; Zhang, Q.; Li, M. M.; Wan, X. J.; Ni, W.; Long, G. K.; Wang, Y. C.; Yang, X.; Feng, H. R.; Chen, Y. S., *J. Am. Chem. Soc.* **2014,** *136*, 15529-15532.

(66) Savoie, B. M.; Rao, A.; Bakulin, A. A.; Gelinas, S.; Movaghar, B.; Friend, R. H.; Marks, T. J.; Ratner, M. A., *J. Am. Chem. Soc.* **2014,** *136*, 2876-2884.

(67) Jung, J.; Lee, W.; Lee, C.; Ahn, H.; Kim, B. J., *Adv. Energy Mater.* **2016**, 1600504.

(68) Li, Z.; Lin, J. D. A.; Phan, H.; Sharenko, A.; Proctor, C. M.; Zalar, P.; Chen, Z. H.; Facchetti, A.; Nguyen, T. Q., *Adv. Funct. Mater.* **2014,** *24*, 6989-6998.

(69) Javed, I.; Saleem, I.; Wang, Y.; Akhtar, M. N., *J. Chem. Soc. Pakistan* **2015,** *37*, 418-425.

(70) McAfee, S. M.; Topple, J. M.; Hill, I. G.; Welch, G. C., *J. Mater. Chem. A* **2015,** *3*, 16393-16408.

(71) Chen, W. Q.; Zhang, Q. C., *J. Mater. Chem. C* **2017,** *5*, 1275-1302.

(72) Perez, M. D.; Borek, C.; Forrest, S. R.; Thompson, M. E., *J. Am. Chem. Soc.* **2009,** *131*, 9281-9286.

(73) Elumalai, N. K.; Uddin, A., *Energ. Environ. Sci.* **2016,** *9*, 391-410.

(74) Scharber, M. C.; Mühlbacher, D.; Koppe, M.; Denk, P.; Waldauf, C.; Heeger, A. J.; Brabec, C. J., *Adv. Mater.* **2006,** *18*, 789-794.

(75) Vandewal, K.; Widmer, J.; Heumueller, T.; Brabec, C. J.; McGehee, M. D.; Leo, K.; Riede, M.; Salleo, A., *Adv. Mater.* **2014,** *26*, 3839-3843.

(76) Graham, K. R.; Cabanetos, C.; Jahnke, J. P.; Idso, M. N.; El Labban, A.; Ndjawa, G. O. N.; Heumueller, T.; Vandewal, K.; Salleo, A.; Chmelka, B. F.; Amassian, A.; Beaujuge, P. M.; McGehee, M. D., *J. Am. Chem. Soc.* **2014,** *136*, 9608-9618.

(77) Ndjawa Guy, O. N.; Graham Kenneth, R.; Mollinger, S.; Wu Di, M.; Hanifi, D.; Prasanna, R.; Rose Bradley, D.; Dey, S.; Yu, L.; Brédas, J.-L.; McGehee Michael, D.; Salleo, A.; Amassian, A., *Adv. Energy Mater.* **2017,** *7*, 1601995.

(78) Ratcliff, E. L.; Garcia, A.; Paniagua, S. A.; Cowan, S. R.; Giordano, A. J.; Ginley, D. S.; Marder, S. R.; Berry, J. J.; Olson, D. C., *Adv. Energy Mater.* **2013,** *3*, 647-656.

(79) Jao, M. H.; Liao, H. C.; Su, W. F., *J Mater Chem A* **2016,** *4*, 5784-5801.

(80) Choi, H.; Ko, S.-J.; Kim, T.; Morin, P.-O.; Walker, B.; Lee Byoung, H.; Leclerc, M.; Kim Jin, Y.; Heeger Alan, J., *Adv. Mater.* **2015,** *27*, 3318-3324.

(81) An, Q.; Zhang, F.; Li, L.; Wang, J.; Sun, Q.; Zhang, J.; Tang, W.; Deng, Z., *ACS Appl. Mater. Inter.* **2015,** *7*, 3691-3698.

(82) Dibb, G. F. A.; Jamieson, F. C.; Maurano, A.; Nelson, J.; Durrant, J. R., *J. Phys. Chem. Lett.* **2013,** *4*, 803-808.

(83) Collins, B. A.; Li, Z.; Tumbleston, J. R.; Gann, E.; McNeill, C. R.; Ade, H., *Adv. Energy Mater.* **2013,** *3*, 65-74.

(84) Liu, Y.; Zhao, J.; Li, Z.; Mu, C.; Ma, W.; Hu, H.; Jiang, K.; Lin, H.; Ade, H.; Yan, H., *Nature Commun.* **2014,** *5*, 5293.

(85) Guo, X. G.; Zhou, N. J.; Lou, S. J.; Smith, J.; Tice, D. B.; Hennek, J. W.; Ortiz, R. P.; Navarrete, J. T. L.; Li, S. Y.; Strzalka, J.; Chen, L. X.; Chang, R. P. H.; Facchetti, A.; Marks, T. J., *Nat. Photonics* **2013,** *7*, 825-833.

(86) Zhang, X.; Richter, L. J.; DeLongchamp, D. M.; Kline, R. J.; Hammond, M. R.; McCulloch, I.; Heeney, M.; Ashraf, R. S.; Smith, J. N.; Anthopoulos, T. D.; Schroeder, B.; Geerts, Y. H.; Fischer, D. A.; Toney, M. F., *J. Am. Chem. Soc.* **2011,** *133*, 15073-15084.

(87) Intemann, J. J.; Yao, K.; Li, Y. X.; Yip, H. L.; Xu, Y. X.; Liang, P. W.; Chueh, C. C.; Ding, F. Z.; Yang, X.; Li, X. S.; Chen, Y.; Jen, A. K. Y., *Adv. Funct. Mater.* **2014,** *24*, 1465-1473.

(88) Wu, Y.; Wang, Z. Y.; Meng, X. Y.; Ma, W., *Prog. Chem.* **2017,** *29*, 93-101.

(89) Huang, H.; Chen, Z. H.; Ortiz, R. P.; Newman, C.; Usta, H.; Lou, S.; Youn, J.; Noh, Y. Y.; Baeg, K. J.; Chen, L. X.; Facchetti, A.; Marks, T. J., *J Am Chem Soc* **2012,** *134*, 10966-10973.

(90) Warren, B. E.; Clarke, J. S., *J. Appl. Phys.* **1965,** *36*, 324-&.

(91) Smilgies, D. M., *J. Appl. Crystallogr.* **2009,** *42*, 1030-1034.

(92) Muller-Buschbaum, P., *Prog. Coll. Pol. Sci. S* **2006,** *132*, 23-32

171.

(93) Beaucage, G., *J. Appl. Crystallogr.* **1996,** *29*, 134-146.

(94) Beaucage, G., *J. Appl. Crystallogr.* **1995,** *28*, 717-728.

(95) DeLongchamp, D. M.; Kline, R. J.; Fischer, D. A.; Richter, L. J.; Toney, M. F., *Adv. Mater.* **2011,** *23*, 319-337.

(96) Germack, D. S.; Chan, C. K.; Kline, R. J.; Fischer, D. A.; Gundlach, D. J.; Toney, M. F.; Richter, L. J.; DeLongchamp, D. M., *Macromolecules* **2010,** *43*, 3828-3836.

(97) Berera, R.; van Grondelle, R.; Kennis, J. T. M., *Photosynth. Res.* **2009,** *101*, 105-118.

(98) Chini, M.; Zhao, K.; Chang, Z., *Nature Photon.* **2014,** *8*, 178.

(99) Rolczynski, B. S.; Szarko, J. M.; Son, H. J.; Yu, L. P.; Chen, L. X., *J. Phys. Chem. Lett.* **2014,** *5*, 1856-1863.

(100) Kaake, L. G.; Moses, D.; Heeger, A. J., *Phys. Rev. B* **2015,** *91*, 075436.

(101) Bakulin, A. A.; Rao, A.; Pavelyev, V. G.; Van Loosdrecht, P. H. M.; Pshenichnikov, M. S.; Niedzialek, D.; Cornil, J.; Beljonne, D.; Friend, R. H., *Science* **2012,** *335*, 1340-1344.

(102) Jakowetz, A. C.; Böhm, M. L.; Zhang, J.; Sadhanala, A.; Huettner, S.; Bakulin, A. A.; Rao, A.; Friend, R. H., *J. Am. Chem. Soc.* **2016,** *138*, 11672-11679.

(103) Zhong, C. M.; Choi, H.; Kim, J. Y.; Woo, H. Y.; Nguyen, T. L.; Huang, F.; Cao, Y.; Heeger, A. J., *Adv. Mater.* **2015,** *27*, 2036-2041.

(104) Wakim, S.; Beaupre, S.; Blouin, N.; Aich, B. R.; Rodman, S.; Gaudiana, R.; Tao, Y.; Leclerc, M., *J. Mater. Chem.* **2009,** *19*, 5351-5358.

(105) Liu, F.; Fan, H. J.; Zhang, Z. G.; Zhu, X. Z., *ACS Appl. Mater. Inter.* **2016,** *8*, 3661-3668.

(106) Rance, W. L.; Ferguson, A. J.; McCarthy-Ward, T.; Heeney, M.; Ginley, D. S.; Olson, D. C.; Rumbles, G.; Kopidakis, N., *ACS Nano* **2011,** *5*, 5635-5646.

(107) Few, S.; Frost, J. M.; Kirkpatrick, J.; Nelson, J., *J. Phys. Chem. C* **2014,** *118*, 8253-8261.

(108) Eastham, N. D.; Dudnik, A. S.; Aldrich, T. J.; Manley, E. F.; Fauvell, T. J.; Hartnett, P. E.; Wasielewski, M. R.; Chen, L. X.; Melkonyan, F. S.; Facchetti, A.; Chang, R. P. H.; Marks, T. J., *Chem. Mater.* **2017,** *29*, 4432-4444.

(109) Luo, D. Y.; Man, J. X.; Yu, L. M.; Liu, Z.; Peng, J.; Shi, G. Z.; Zhu, X. X.; Ma, W. L., *Phys. Status Solidi A* **2016,** *213*, 412-418.

(110) Constantinou, I.; Lai, T. H.; Hsu, H. Y.; Cheung, S. H.; Klump, E. D.; Schanze, K. S.; So, S. K.; So, F., *Adv. Electron. Mater.* **2015,** *1*, 1500167.

(111) Wang, T.; Pearson, A. J.; Lidzey, D. G.; Jones, R. A. L., *Adv. Funct. Mater.* **2011,** *21*, 1383-1390.

(112) Miao, J. S.; Chen, H.; Liu, F.; Zhao, B. F.; Hu, L. Y.; He, Z. C.; Wu, H. B., *Appl. Phys. Lett.* **2015,** *106*, 183302.

(113) Gao, K.; Miao, J. S.; Xiao, L. A.; Deng, W. Y.; Kan, Y. Y.; Liang, T. X.; Wang, C.; Huang, F.; Peng, J. B.; Cao, Y.; Liu, F.; Russell, T. P.; Wu, H. B.; Peng, X. B., *Adv. Mater.* **2016,** *28*, 4727-4733.

(114) Xu, W. L.; Zheng, F.; He, J. L.; Zhu, M. Q.; Hao, X. T., *Chem. Phys.* **2015,** *457*, 7-12.

(115) Schaffer, C. J.; Schlipf, J.; Indari, E. D.; Su, B.; Bernstorff, S.; Muller-Buschbaum, P., *ACS Appl. Mater. Inter.* **2015,** *7*, 21347-21355.

(116) Dennler, G.; Brabec, C. J., Socio-Economic Impact of Low-Cost PV Technologies. In *Organic Photovoltaics*, Wiley-VCH Verlag GmbH & Co. KGaA: 2009; pp 531-566.

(117) Scully, S. R.; McGehee, M. D., *J. Appl. Phys.* **2006,** *100*, 034907-1.

(118) Erb, T.; Zhokhavets, U.; Hoppe, H.; Gobsch, G.; Al-Ibrahim, M.; Ambacher, O., *Thin Solid Films* **2006,** *511*, 483-485.

(119) Miller, S.; Fanchini, G.; Lin, Y. Y.; Li, C.; Chen, C. W.; Su, W. F.; Chhowalla, M., *J. Mater. Chem.* **2008,** *18*, 306-312.

(120) Chen, F. C.; Ko, C. J.; Wu, J. L.; Chen, W. C., *Sol. Energ. Mat. Sol. Cells* **2010,** *94*, 2426-2430.

(121) Pivrikas, A.; Neugebauer, H.; Sariciftci, N. S., *Sol. Energy* **2011,** *85* 1226-1238.

(122) Hoven, C. V.; Dang, X. D.; Coffin, R. C.; Peet, J.; Nguyen, T. Q.; Bazan, G. C., *Adv. Mater.* **2010,** *22*, E63-E66.

(123) Salim, T.; Wong, L. H.; Brauer, B.; Kukreja, R.; Foo, Y. L.; Bao, Z. N.; Lam, Y. M., *J. Mater. Chem.* **2011,** *21*, 242-250.

(124) Lee, J. K.; Ma, W. L.; Brabec, C. J.; Yuen, J.; Moon, J. S.; Kim, J. Y.; Lee, K.; Bazan, G. C.; Heeger, A. J., *J. Am. Chem. Soc.* **2008,** *130*, 3619-3623.

(125) Zhang, Y. G.; Li, Z.; Wakim, S.; Alem, S.; Tsang, S. W.; Lu, J. P.; Ding, J. F.; Tao, Y., *Org. Electron.* **2011,** *12*, 1211-1215.

(126) Guo, J. C.; Liang, Y. Y.; Szarko, J.; Lee, B.; Son, H. J.; Rolczynski, B. S.; Yu, L. P.; Chen, L. X., *J. Phys. Chem. B* **2010,** *114*, 742-748.

(127) Di Nuzzo, D.; Aguirre, A.; Shahid, M.; Gevaerts, V. S.; Meskers, S. C. J.; Janssen, R. A. J., *Adv. Mater.* **2010,** *22*, 4321-4324.

(128) Liang, Y. Y.; Wu, Y.; Feng, D. Q.; Tsai, S. T.; Son, H. J.; Li, G.; Yu, L. P., *J. Am. Chem. Soc.* **2009,** *131*, 56-57.

(129) Ilavsky, J.; Jemian, P. R., *J. Appl. Crystallogr.* **2009,** *42*, 347-353.

(130) Lu, L.; Zheng, T.; Wu, Q.; Schneider, A. M.; Zhao, D.; Yu, L., *Chem. Rev.* **2015,** *115*, 12666-12731.

(131) Scharber, M. C., *Adv. Mater.* **2016,** *28*, 1994-2001.

(132) Choi, H.; Ko, S.-J.; Kim, T.; Morin, P.-O.; Walker, B.; Lee, B. H.; Leclerc, M.; Kim, J. Y.; Heeger, A. J., *Adv. Mater.* **2015,** *27*, 3318-3324.

(133) Lin, Y.; Zhao, F.; Wu, Y.; Chen, K.; Xia, Y.; Li, G.; Prasad, S. K. K.; Zhu, J.; Huo, L.; Bin, H.; Zhang, Z.-G.; Guo, X.; Zhang, M.; Sun, Y.; Gao, F.; Wei, Z.; Ma, W.; Wang, C.; Hodgkiss, J.; Bo, Z.; Inganäs, O.; Li, Y.; Zhan, X., *Adv. Mater.* **2017,** *29*, 1604155.

(134) Yan, C. Q.; Barlow, S.; Wang, Z. H.; Yan, H.; Jen, A. K. Y.; Marder, S. R.; Zhan, X. W., *Nat. Rev. Mater.* **2018,** *3*, 18003.

(135) Chu, T. Y.; Lu, J. P.; Beaupre, S.; Zhang, Y. G.; Pouliot, J. R.; Wakim, S.; Zhou, J. Y.; Leclerc, M.; Li, Z.; Ding, J. F.; Tao, Y., *J. Am. Chem. Soc.* **2011,** *133*, 4250-4253.

(136) Scharber, M. C.; Sariciftci, N. S., *Prog. Polym. Sci.* **2013,** *38*, 1929-1940.

(137) Li, S.; Ye, L.; Zhao, W.; Yan, H.; Yang, B.; Liu, D.; Li, W.; Ade, H.; Hou, J., *J. Am. Chem. Soc.* **2018,** *140*, 7159-7167.

(138) Dimitrov, S. D.; Durrant, J. R., *Chem. Mater.* **2013,** *26*, 616-630.

(139) Noriega, R.; Rivnay, J.; Vandewal, K.; Koch, F. P. V.; Stingelin, N.; Smith, P.; Toney, M. F.; Salleo, A., *Nature Mater.* **2013,** *12*, 1038-1044.

(140) Hawks, S. A.; Deledalle, F.; Yao, J.; Rebois, D. G.; Li, G.; Nelson, J.; Yang, Y.; Kirchartz, T.; Durrant, J. R., *Adv. Energy Mater.* **2013,** *3*, 1201-1209.

(141) Kurpiers, J.; Neher, D., *Sci. Rep.* **2016,** *6*, 26832.

(142) Bartesaghi, D.; Perez, I. d. C.; Kniepert, J.; Roland, S.; Turbiez, M.; Neher, D.; Koster, L. J. A., *Nat. Commun.* **2015,** *6*, 7083.

(143) Lima, I. T.; Risko, C.; Aziz, S. G.; da Silva, D. A.; Bredas, J. L., *J. Mater. Chem. C* **2014,** *2*, 8873-8879.

(144) Zhang, K.; Hu, Z.; Sun, C.; Wu, Z.; Huang, F.; Cao, Y., *Chem. Mater.* **2017,** *29*, 141-148.

(145) Wang, G.; Eastham, N. D.; Aldrich, T. J.; Ma, B. R.; Manley, E. F.; Chen, Z. H.; Chen, L. X.; de la Cruz, M. O.; Chang, R. P. H.; Melkonyan, F. S.; Facchetti, A.; Marks, T. J., *Adv. Energy Mater.* **2018,** *8*, 1702173.

(146) Verma, A. K.; Agnihotri, P.; Patel, M.; Sahu, S.; Tiwari, S., *Mater. Res. Found.* **2017,** *17*, 299-309.

(147) Do, K.; Ravva, M. K.; Wang, T. H.; Bredas, J. L., *Chem. Mater.* **2017,** *29*, 346-354.

(148) Hildner, R.; Kohler, A.; Muller-Buschbaum, P.; Panzer, F.; Thelakkat, M., *Adv. Energy Mater.* **2017,** *7*, 1700314.

(149) Ryno, S. M.; Ravva, M. K.; Chen, X. K.; Li, H. Y.; Bredas, J. L., *Adv. Energy Mater.* **2017,** *7*, 1601370.

(150) Ma, Y. L.; Kang, Z. J.; Zheng, Q. D., *J. Mater. Chem. A* **2017,** *5*, 1860-1872.

(151) Zhang, Y.; Zou, J.; Cheuh, C.-C.; Yip, H.-L.; Jen, A. K. Y., *Macromolecules* **2012,** *45*, 5427-5435.

(152) Wang, J.-Y.; Hau, S. K.; Yip, H.-L.; Davies, J. A.; Chen, K.-S.; Zhang, Y.; Sun, Y.; Jen, A. K. Y., *Chem. Mater.* **2010,** *23*, 765-767.

(153) Stalder, R.; Grand, C.; Subbiah, J.; So, F.; Reynolds, J. R., *Polym. Chem. - UK* **2012,** *3*, 89-92.

(154) Liu, B.; Chen, X. W.; He, Y. H.; Xiao, L.; Li, Y. F.; Zhou, K. C.; Fan, L.; Zou, Y. P., *RSC Adv.* **2013,** *3*, 5366-5369.

(155) Li, W. W.; Furlan, A.; Roelofs, W. S. C.; Hendriks, K. H.; van Pruissen, G. W. P.; Wienk, M. M.; Janssen, R. A. J., *Chem. Commun.* **2014,** *50*, 679-681.

(156) Pandit, B.; Jackson, N. E.; Zheng, T.; Fauvell, T. J.; Manley, E. F.; Orr, M.; Brown-Xu, S.; Yu, L.; Chen, L. X., *J. Phys. Chem. C* **2016,** *120*, 4189-4198.

(157) Jackson, N. E.; Savoie, B. M.; Marks, T. J.; Chen, L. X.; Ratner, M. A., *J. Phys. Chem. Lett.* **2015,** *6*, 77-84.

(158) Hwang, I. W.; Soci, C.; Moses, D.; Zhu, Z. G.; Waller, D.; Gaudiana, R.; Brabec, C. J.; Heeger, A. J., *Adv. Mater.* **2007,** *19*, 2307-2312.

(159) Padinger, F.; Rittberger, R. S.; Sariciftci, N. S., *Adv. Funct. Mater.* **2003,** *13*, 85-88.

(160) Grzegorczyk, W. J.; Savenije, T. J.; Heeney, M.; Tierney, S.; McCulloch, I.; van Bavel, S.; Siebbeles, L. D. A., *J. Phys. Chem. C* **2008,** *112*, 15973-15979.

(161) Muller, C.; Bergqvist, J.; Vandewal, K.; Tvingstedt, K.; Anselmo, A. S.; Magnusson, R.; Alonso, M. I.; Moons, E.; Arwin, H.; Campoy-Quiles, M.; Inganas, O., *J. Mater. Chem.* **2011,** *21*, 10676-10684.

(162) Park, J. K.; Jo, J.; Seo, J. H.; Moon, J. S.; Park, Y. D.; Lee, K.; Heeger, A. J.; Bazan, G. C., *Adv. Mater.* **2011,** *23*, 2430-2435.

(163) Tummala, N. R.; Sutton, C.; Aziz, S. G.; Toney, M. F.; Risko, C.; Bredas, J.-L., *Chem. Mater.* **2015,** *27*, 8261-8272.

(164) Li, Z. F.; Dong, Q. F.; Yao, S. Y.; Qian, J. Y.; Wang, Y. L.; Jiang, F. Y.; Yang, H.; Zhao, Q.; Hou, Q. F.; Meng, W.; Tong, J. H.; Xiong, S. X.; Tian, W. J., *J. Mater. Sci.* **2015,** *50*, 937-947.

(165) He, Z.; Zhong, C.; Su, S.; Xu, M.; Wu, H.; Cao, Y., *Nat. Photonics* **2012,** *6*, 591-595.

(166) Aldrich, T. J.; Swick, S. M.; Melkonyan, F. S.; Marks, T. J., *Chem. Mater.* **2017,** *29*, 10294-10298.

(167) Hoppe, H.; Niggemann, M.; Winder, C.; Kraut, J.; Hiesgen, R.; Hinsch, A.; Meissner, D.; Sariciftci, N. S., *Adv. Funct. Mater.* **2004,** *14*, 1005-1011.

(168) Muller, C.; Ferenczi, T. A. M.; Campoy-Quiles, M.; Frost, J. M.; Bradley, D. D. C.; Smith, P.; Stingelin-Stutzmann, N.; Nelson, J., *Adv. Mater.* **2008,** *20*, 3510-3515.

(169) Huo, L.; Liu, T.; Sun, X.; Cai, Y.; Heeger, A. J.; Sun, Y., *Adv. Mater.* **2015,** *27*, 2938-2944.

(170) Liu, C.; Yi, C.; Wang, K.; Yang, Y.; Bhatta, R. S.; Tsige, M.; Xiao, S.; Gong, X., *ACS Appl. Mater. Inter.* **2015,** *7*, 4928-4935.

(171) Moon, J. S.; Takacs, C. J.; Cho, S.; Coffin, R. C.; Kim, H.; Bazan, G. C.; Heeger, A. J., *Nano Lett.* **2010,** *10*, 4005-4008.

(172) Aich, B. R.; Lu, J. P.; Beaupre, S.; Leclerc, M.; Tao, Y., *Org. Electron.* **2012,** *13*, 1736-1741.

(173) Chen, F. C.; Tseng, H. C.; Ko, C. J., *Appl. Phys. Lett.* **2008,** *92*, 103316.

(174) Jhuo, H.-J.; Liao, S.-H.; Li, Y.-L.; Yeh, P.-N.; Chen, S.-A.; Wu, W.-R.; Su, C.-J.; Lee, J.-J.; Yamada, N. L.; Jeng, U. S., *Adv. Funct. Mater.* **2016,** *26*, 3094-3104.

(175) Zhao, J.; Li, Y.; Yang, G.; Jiang, K.; Lin, H.; Ade, H.; Ma, W.; Yan, H., *Nature Energ.* **2016,** *1*, 15027.

(176) Duong, D. T.; Walker, B.; Lin, J.; Kim, C.; Love, J.; Purushothaman, B.; Anthony, J. E.; Nguyen, T. Q., *J. Polym. Sci. Pol. Phys.* **2012,** *50*, 1405-1413.

(177) Kniepert, J.; Lange, I.; Heidbrink, J.; Kurpiers, J.; Brenner, T. J. K.; Koster, L. J. A.; Neher, D., *J. Phys. Chem. C* **2015,** *119*, 8310-8320.

(178) Fischer, F. S. U.; Trefz, D.; Back, J.; Kayunkid, N.; Tornow, B.; Albrecht, S.; Yager, K. G.; Singh, G.; Karim, A.; Neher, D.; Brinkmann, M.; Ludwigs, S., *Adv. Mater.* **2015,** *27*, 1223-1228.

(179) Peet, J.; Cho, N. S.; Lee, S. K.; Bazan, G. C., *Macromolecules* **2008,** *41*, 8655-8659.

(180) Dang, M. T.; Wuest, J. D., *Chem. Soc. Rev.* **2013,** *42*, 9105-9126.

(181) Rogers, J. T.; Schmidt, K.; Toney, M. F.; Bazan, G. C.; Kramer, E. J., *J. Am. Chem. Soc.* **2012,** *134*, 2884-2887.

(182) Lee, T. H.; Park, S. Y.; Walker, B.; Ko, S.-J.; Heo, J.; Woo, H. Y.; Choi, H.; Kim, J. Y., *Rsc Adv.* **2017,** *7*, 7476-7482.

(183) Manley, E. F.; Strzalka, J.; Fauvell, T. J.; Jackson, N. E.; Leonardi, M. J.; Eastham, N. D.; Marks, T. J.; Chen, L. X., *Adv. Mater.* **2017,** *29*, 1703933.

(184) Manley, E. F.; Strzalka, J.; Fauvell, T. J.; Marks, T. J.; Chen, L. X., *Adv. Energy Mater.* **2018**, 1800611.

(185) Shin, N.; Richter, L. J.; Herzing, A. A.; Kline, R. J.; DeLongchamp, D. M., *Adv. Energy Mater.* **2013,** *3*, 938-948.

(186) Mao, Z. H.; Le, T. P.; Vakhshouri, K.; Fernando, R.; Ruan, F.; Muller, E.; Gomez, E. D.; Sauve, G., *Org. Electron.* **2014,** *15*, 3384-3391.

(187) Zhang, X.; Zhan, C. L.; Yao, J. N., *Chem. Mater.* **2015,** *27*, 166-173.

(188) Huang, W.; Gann, E.; Thomsen, L.; Dong, C.; Cheng, Y.-B.; McNeill, C. R., *Adv. Energy Mater.* **2015,** *5*, 1401259.

(189) Gao, F.; Himmelberger, S.; Andersson, M.; Hanifi, D.; Xia, Y. X.; Zhang, S. Q.; Wang, J. P.; Hou, J. H.; Salleo, A.; Inganas, O., *Adv. Mater.* **2015,** *27*, 3868.

(190) Sweetnam, S.; Prasanna, R.; Burke, T. M.; Bartelt, J. A.; McGehee, M. D., *J. Phys. Chem. C* **2016,** *120*, 6427-6434.

(191) Woo, C. H.; Beaujuge, P. M.; Holcombe, T. W.; Lee, O. P.; Fréchet, J. M. J., *J. Am. Chem. Soc.* **2010,** *132*, 15547-15549.

(192) Guo, S.; Wang, W.; Herzig, E. M.; Naumann, A.; Tainter, G.; Perlich, J.; Müller-Buschbaum, P., *Acs Appl. Mater. Inter.* **2017,** *9*, 3740-3748.

(193) Lou, S. J.; Szarko, J. M.; Xu, T.; Yu, L. P.; Marks, T. J.; Chen, L. X., *J. Am. Chem. Soc.* **2011,** *133*, 20661-20663.

(194) Mukherjee, S.; Jiao, X.; Ade, H., *Adv. Energy Mater.* **2016,** *6*, 1600699.

(195) Mukherjee, S.; Proctor, C. M.; Bazan, G. C.; Nguyen, T. Q.; Ade, H., *Adv. Energy Mater.* **2015,** *5*, 1500877.

(196) Sweetnam, S.; Graham, K. R.; Ngongang Ndjawa, G. O.; Heumüller, T.; Bartelt, J. A.; Burke, T. M.; Li, W.; You, W.; Amassian, A.; McGehee, M. D., *J. Am. Chem. Soc.* **2014,** *136*, 14078-14088.

(197) Guilbert, A. A. Y.; Schmidt, M.; Bruno, A.; Yao, J.; King, S.; Tuladhar, S. M.; Kirchartz, T.; Alonso, M. I.; Goñi, A. R.; Stingelin, N.; Haque, S. A.; Campoy-Quiles, M.; Nelson, J., *Adv. Funct. Mater.* **2014,** *24*, 6972-6980.

(198) Oh, S. J.; Kim, J.; Mativetsky, J. M.; Loo, Y.-L.; Kagan, C. R., *ACS Appl. Mater. Inter.* **2016,** *8*, 28743-28749.

(199) Collins, B. A.; Gann, E.; Guignard, L.; He, X.; McNeill, C. R.; Ade, H., *J. Phys. Chem. Lett.* **2010,** *1*, 3160-3166.

(200) You, J. B.; Chen, C. C.; Hong, Z. R.; Yoshimura, K.; Ohya, K.; Xu, R.; Ye, S. L.; Gao, J.; Li, G.; Yang, Y., *Adv. Mater.* **2013,** *25*, 3973-3978.

(201) Xin, H.; Guo, X. G.; Ren, G. Q.; Watson, M. D.; Jenekhe, S. A., *Adv. Energy Mater.* **2012,** *2*, 575-582.

(202) Collins, B. A.; Li, Z.; Tumbleston, J. R.; Gann, E.; McNeill, C. R.; Ade, H., *Adv. Energy Mater.* **2012,** *3*, 65-74.

(203) Zhou, C.; Zhang, G.; Zhong, C.; Jia, X.; Luo, P.; Xu, R.; Gao, K.; Jiang, X.; Liu, F.; Russell, T. P.; Huang, F.; Cao, Y., *Adv. Energy Mater.* **2017,** *7*, 1601081.

(204) Yuan, J.; Ford, M.; Ma, W.; Bazan, G. C., *J. Mater. Chem. A* **2017,** *5*, 8903-8908.

(205) Scarongella, M.; De Jonghe-Risse, J.; Buchaca-Domingo, E.; Causa, M.; Fei, Z. P.; Heeney, M.; Moser, J. E.; Stingelin, N.; Banerji, N., *J. Am. Chem. Soc.* **2015,** *137*, 2908-2918.

(206) Kaake, L. G.; Welch, G. C.; Moses, D.; Bazan, G. C.; Heeger, A. J., *J. Phys. Chem. Lett.* **2012,** *3*, 1253-1257.

(207) Huettner, S.; Hodgkiss, J. M.; Sommer, M.; Friend, R. H.; Steiner, U.; Thelakkat, M., *J. Phys. Chem. B* **2012,** *116*, 10070-10078.

(208) Poelking, C.; Andrienko, D., *J. Am. Chem. Soc.* **2015,** *137*, 6320-6326.

(209) Scharber, M. C.; Lungenschmied, C.; Egelhaaf, H. J.; Matt, G.; Bednorz, M.; Fromherz, T.; Gao, J.; Jarzab, D.; Loi, M. A., *Energ. Environ. Sci.* **2011,** *4*, 5077-5083.

(210) Grancini, G.; Martino, N.; Antognazza, M. R.; Celebrano, M.; Egelhaaf, H.-J.; Lanzani, G., *J. Phys. Chem. C* **2012,** *116*, 9838-9844.

(211) Eastham, N. D.; Logsdon, J. L.; Manley, E. F.; Aldrich, T. J.; Leonardi, M. J.; Wang, G.; Powers-Riggs, N. E.; Young, R. M.; Chen, L. X.; Wasielewski, M. R.; Melkonyan, F. S.; Chang, R. P. H.; Marks, T. J., *Adv Mater* **2018,** *30*, 1704263.

(212) Zhou, N. J.; Guo, X. G.; Ortiz, R. P.; Li, S. Q.; Zhang, S. M.; Chang, R. P. H.; Facchetti, A.; Marks, T. J., *Adv. Mater.* **2012,** *24*, 2242-2248.

(213) Huang, H.; Yang, L.; Facchetti, A.; Marks, T. J., *Chem. Rev.* **2017,** *117*, 10291-10318.

(214) Hammouda, B., *J. Appl. Crystallogr.* **2010,** *43*, 716-719.

(215) Bakulin, A. A.; Dimitrov, S. D.; Rao, A.; Chow, P. C. Y.; Nielsen, C. B.; Schroeder, B. C.; McCulloch, I.; Bakker, H. J.; Durrant, J. R.; Friend, R. H., *J. Phys. Chem. Lett.* **2013,** *4*, 209-215.

(216) Andernach, R.; Utzat, H.; Dimitrov, S. D.; McCulloch, I.; Heeney, M.; Durrant, J. R.; Bronstein, H., *J. Am. Chem. Soc.* **2015,** *137*, 10383-10390.

(217) Collado-Fregoso, E.; Boufflet, P.; Fei, Z.; Gann, E.; Ashraf, S.; Li, Z.; McNeill, C. R.; Durrant, J. R.; Heeney, M., *Chem. Mater.* **2015,** *27*, 7934-7944.

(218) Fauvell, T. J.; Zheng, T. Y.; Jackson, N. E.; Ratner, M. A.; Yu, L. P.; Chen, L. X., *Chem. Mater.* **2016,** *28*, 2814-2822.

(219) Soon, Y. W.; Shoaee, S.; Ashraf, R. S.; Bronstein, H.; Schroeder, B. C.; Zhang, W.; Fei, Z.; Heeney, M.; McCulloch, I.; Durrant, J. R., *Adv. Funct. Mater.* **2014,** *24*, 1474-1482.

(220) Li, K. J.; Khlyabich, P. P.; Li, L. J.; Burkhart, B.; Thompson, B. C.; Campbell, J. C., *J. Phys. Chem. C* **2013,** *117*, 6940-6948.

(221) Dibb, G. F. A.; Jamieson, F. C.; Maurano, A.; Nelson, J.; Durrant, J. R., *J. Phys. Chem. Lett.* **2013,** *4*, 803-808.

(222) Howard, I. A.; Mauer, R.; Meister, M.; Laquai, F., *J. Am. Chem. Soc.* **2010,** *132*, 14866-14876.

(223) Wu, Q. H.; Zhao, D. L.; Schneider, A. M.; Chen, W.; Yu, L. P., *J. Am. Chem. Soc.* **2016,** *138*, 7248-7251.

(224) Marrocchi, A.; Facchetti, A.; Lanari, D.; Petrucci, C.; Vaccaro, L., *Energ. Environ. Sci.* **2016,** *9*, 763-786.

(225) Wang, J. L.; Xiao, F.; Yan, J.; Wu, Z.; Liu, K. K.; Chang, Z. F.; Zhang, R. B.; Chen, H.; Wu, H. B.; Cao, Y., *Adv. Funct. Mater.* **2016,** *26*, 1803-1812.

(226) Harschneck, T.; Zhou, N. J.; Manley, E. F.; Lou, S. J.; Yu, X. G.; Butler, M. R.; Timalsina, A.; Turrisi, R.; Ratner, M. A.; Chen, L. X.; Chang, R. P. H.; Facchetti, A.; Marks, T. J., *Chem. Commun.* **2014,** *50*, 9609-9609.

(227) Zhong, Y.; Trinh, M. T.; Chen, R. S.; Wang, W.; Khlyabich, P. P.; Kumar, B.; Xu, Q. Z.; Nam, C. Y.; Sfeir, M. Y.; Black, C.; Steigerwald, M. L.; Loo, Y. L.; Xiao, S. X.; Ng, F.; Zhu, X. Y.; Nuckolls, C., *J. Am. Chem. Soc.* **2014,** *136*, 15215-15221.

(228) Min, J.; Luponosov, Y. N.; Gerl, A.; Polinskaya, M. S.; Peregudova, S. M.; Dmitryakov, P. V.; Bakirov, A. V.; Shcherbina, M. A.; Chvalun, S. N.; Grigorian, S.; Kaush-Busies, N.; Ponomarenko, S. A.; Ameri, T.; Brabec, C. J., *Adv. Energy Mater.* **2014,** *4*, 1301234.

(229) Love, J. A.; Nagao, I.; Huang, Y.; Kuik, M.; Gupta, V.; Takacs, C. J.; Coughlin, J. E.; Qi, L.; van der Poll, T. S.; Kramer, E. J.; Heeger, A. J.; Nguyen, T. Q.; Bazan, G. C., *J. Am. Chem. Soc.* **2014,** *136*, 3597-3606.

(230) Sun, Y. M.; Seifter, J.; Wang, M.; Perez, L. A.; Luo, C.; Bazan, G. C.; Huang, F.; Cao, Y.; Heeger, A. J., *Adv. Energy Mater.* **2014,** *4*, 1301601.

(231) Kwon, O. K.; Park, J. H.; Kim, D. W.; Park, S. K.; Park, S. Y., *Adv. Mater.* **2015,** *27*, 1951-1956.

(232) Zhang, Q.; Kan, B.; Liu, F.; Long, G. K.; Wan, X. J.; Chen, X. Q.; Zuo, Y.; Ni, W.; Zhang, H. J.; Li, M. M.; Hu, Z. C.; Huang, F.; Cao, Y.; Liang, Z. Q.; Zhang, M. T.; Russell, T. P.; Chen, Y. S., *Nat. Photonics* **2015,** *9*, 35-41.

(233) Burckstummer, H.; Tulyakova, E. V.; Deppisch, M.; Lenze, M. R.; Kronenberg, N. M.; Gsanger, M.; Stolte, M.; Meerholz, K.; Wurthner, F., *Angew. Chem., Int. Ed.* **2011,** *50*, 11628-11632.

(234) Sun, Y. M.; Welch, G. C.; Leong, W. L.; Takacs, C. J.; Bazan, G. C.; Heeger, A. J., *Nature Mater.* **2012,** *11*, 44-48.

(235) Walker, B.; Liu, J. H.; Kim, C.; Welch, G. C.; Park, J. K.; Lin, J.; Zalar, P.; Proctor, C. M.; Seo, J. H.; Bazan, G. C.; Nguyen, T. Q., *Energ. Environ. Sci.* **2013,** *6*, 952-962.

(236) Roncali, J.; Leriche, P.; Blanchard, P., *Adv. Mater.* **2014,** *26*, 3821-3838.

(237) Walker, B.; Kim, C.; Nguyen, T. Q., *Chem. Mater.* **2011,** *23*, 470-482.

(238) Chen, Y. H.; Lin, L. Y.; Lu, C. W.; Lin, F.; Huang, Z. Y.; Lin, H. W.; Wang, P. H.; Liu, Y. H.; Wong, K. T.; Wen, J. G.; Miller, D. J.; Darling, S. B., *J. Am. Chem. Soc.* **2012,** *134*, 13616-13623.

(239) Fitzner, R.; Reinold, E.; Mishra, A.; Mena-Osteritz, E.; Ziehlke, H.; Korner, C.; Leo, K.; Riede, M.; Weil, M.; Tsaryova, O.; Weiss, A.; Uhrich, C.; Pfeiffer, M.; Bauerle, P., *Adv. Funct. Mater.* **2011,** *21*, 897-910.

(240) Wang, S.; Mayo, E. I.; Perez, M. D.; Griffe, L.; Wei, G.; Djurovich, P. I.; Forrest, S. R.; Thompson, M. E., *Appl. Phys. Lett.* **2009,** *94*, 233304-233307.

(241) Yoo, S.; Domercq, B.; Kippelen, B., *J. Appl. Phys.* **2005,** *97*, 103706-103715.

(242) Yang, F.; Shtein, M.; Forrest, S. R., *J. Appl. Phys.* **2005,** *98*, 014906-014916.

(243) Usta, H.; Kim, C.; Wang, Z. M.; Lu, S. F.; Huang, H.; Facchetti, A.; Marks, T. J., *J. Mater. Chem.* **2012,** *22*, 4459-4472.

(244) Youn, J.; Huang, P. Y.; Huang, Y. W.; Chen, M. C.; Lin, Y. J.; Huang, H.; Ortiz, R. P.; Stern, C.; Chung, M. C.; Feng, C. Y.; Chen, L. H.; Facchetti, A.; Marks, T. J., *Adv. Funct. Mater.* **2012,** *22*, 48-60.

(245) Qiao, Y.; Guo, Y.; Yu, C.; Zhang, F.; Xu, W.; Liu, Y.; Zhu, D., *J. Am. Chem. Soc.* **2012,** *134*, 4084-4087.

(246) Yanagi, H.; Araki, Y.; Ohara, T.; Hotta, S.; Ichikawa, M.; Taniguchi, Y., *Adv. Funct. Mater.* **2003,** *13*, 767-773.

(247) Shtein, M.; Mapel, J.; Benziger, J. B.; Forrest, S. R., *Appl. Phys. Lett.* **2002,** *81*, 268-270.

(248) Dimitrakopoulos, C. D.; Brown, A. R.; Pomp, A., *J. Appl. Phys.* **1996,** *80*, 2501-2508.

(249) Wong, C. Y.; Cotts, B. L.; Wu, H.; Ginsberg, N. S., *Nature Commun.* **2015,** *6*, 5946.

(250) van der Poll, T. S.; Zhugayevych, A.; Chertkov, E.; Bakus, R. C.; Coughlin, J. E.; Teat, S. J.; Bazan, G. C.; Tretiak, S., *J. Phys. Chem. Lett.* **2014,** *5*, 2700-2704.

(251) Savoie, B. M.; Kohlstedt, K. L.; Jackson, N. E.; Chen, L. X.; de la Cruz, M. O.; Schatz, G. C.; Marks, T. J.; Ratner, M. A., *Proc. Natl. Acad. Sci. USA* **2014,** *111*, 10055-10060.

(252) Ran, N. A.; Kuik, M.; Love, J. A.; Proctor, C. M.; Nagao, I.; Bazan, G. C.; Nguyen, T. Q., *Adv. Mater.* **2014,** *26*, 7405-7412.

(253) Heitzer, H. M.; Savoie, B. M.; Marks, T. J.; Ratner, M. A., *Angew. Chem., Int. Ed.* **2014,** *53*, 7456-7460.

(254) Huang, Y.; Liu, X. F.; Wang, C.; Rogers, J. T.; Su, G. M.; Chabinyc, M. L.; Kramer, E. J.; Bazan, G. C., *Adv. Energy Mater.* **2014,** *4*, 1301886.

(255) Mukherjee, S.; Proctor, C. M.; Tumbleston, J. R.; Bazan, G. C.; Nguyen, T. Q.; Ade, H., *Adv. Mater.* **2015,** *27*, 1105-1111.

(256) Love, J. A.; Collins, S. D.; Nagao, I.; Mukherjee, S.; Ade, H.; Bazan, G. C.; Nguyen, T. Q., *Adv. Mater.* **2014,** *26*, 7308-7316.

(257) Coughlin, J. E.; Henson, Z. B.; Welch, G. C.; Bazan, G. C., *Acc. Chem. Res.* **2014,** *47*, 257-270.

(258) Huang, Y.; Kramer, E. J.; Heeger, A. J.; Bazan, G. C., *Chem. Rev.* **2014,** *114*, 7006-7043.

(259) Lu, L.; Chen, W.; Xu, T.; Yu, L., **2015,** *6*, 7327.

(260) Vandewal, K.; Himmelberger, S.; Salleo, A., *Macromolecules* **2013,** *46*, 6379-6387.

(261) Sirringhaus, H.; Brown, P. J.; Friend, R. H.; Nielsen, M. M.; Bechgaard, K.; Langeveld-Voss, B. M. W.; Spiering, A. J. H.; Janssen, R. A. J.; Meijer, E. W.; Herwig, P.; de Leeuw, D. M., *Nature* **1999,** *401*, 685-688.

(262) Zhang, X. R.; Bronstein, H.; Kronemeijer, A. J.; Smith, J.; Kim, Y.; Kline, R. J.; Richter, L. J.; Anthopoulos, T. D.; Sirringhaus, H.; Song, K.; Heeney, M.; Zhang, W. M.; McCulloch, I.; DeLongchamp, D. M., *Nat. Commun.* **2013,** *4*, 2238.

(263) Takacs, C. J.; Treat, N. D.; Kramer, S.; Chen, Z. H.; Facchetti, A.; Chabinyc, M. L.; Heeger, A. J., *Nano Lett.* **2013,** *13*, 2522-2527.

(264) Bassler, H., *Phys. Status Solidi B* **1993,** *175*, 15-56.

(265) Kurosawa, T.; Chiu, Y.-C.; Zhou, Y.; Gu, X.; Chen, W.-C.; Bao, Z., **2016,** *26*, 1261-1270.

(266) Liu, J.; Zhang, Y.; Phan, H.; Sharenko, A.; Moonsin, P.; Walker, B.; Promarak, V.; Nguyen, T.-Q., *Adv. Mater.* **2013,** *25*, 3645-3650.

(267) Karak, S.; Liu, F.; Russell, T. P.; Duzhko, V. V., *ACS Appl. Mater. Inter.* **2014,** *6*, 20904-20912.

(268) Takacs, C. J.; Collins, S. D.; Love, J. A.; Mikhailovsky, A. A.; Wynands, D.; Bazan, G. C.; Nguyen, T. Q.; Heeger, A. J., *ACS Nano* **2014,** *8*, 8141-8151.

(269) Schweicher, G.; Lemaur, V.; Niebel, C.; Ruzie, C.; Diao, Y.; Goto, O.; Lee, W. Y.; Kim, Y.; Arlin, J. B.; Karpinska, J.; Kennedy, A. R.; Parkin, S. R.; Olivier, Y.; Mannsfeld, S. C.; Cornil, J.; Geerts, Y. H.; Bao, Z., **2015,** *27*, 3066-72.

(270) Chen, H. P.; Peet, J.; Hu, S.; Azoulay, J.; Bazan, G.; Dadmun, M., *Adv. Funct. Mater.* **2014,** *24*, 140-150.

(271) Poelking, C.; Andrienko, D., *J. Am. Chem. Soc.* **2015,** *137*, 6320-6326.

(272) Miller, N. C.; Cho, E.; Gysel, R.; Risko, C.; Coropceanu, V.; Miller, C. E.; Sweetnam, S.; Sellinger, A.; Heeney, M.; McCulloch, I.; Bredas, J. L.; Toney, M. F.; McGehee, M. D., *Adv. Energy Mater.* **2012,** *2*, 1208-1217.

(273) Thompson, B. C.; Kim, B. J.; Kavulak, D. F.; Sivula, K.; Mauldin, C.; Fréchet, J. M. J., *Macromolecules* **2007,** *40*, 7425-7428.

(274) Gu, Y.; Wang, C.; Russell, T. P., *Adv. Energy Mater.* **2012,** *2*, 683-690.

(275) Love, J. A.; Proctor, C. M.; Liu, J. H.; Takacs, C. J.; Sharenko, A.; van der Poll, T. S.; Heeger, A. J.; Bazan, G. C.; Nguyen, T. Q., *Adv. Funct. Mater.* **2013,** *23*, 5019-5026.

(276) Aytun, T.; Barreda, L.; Ruiz-Carretero, A.; Lehrman, J. A.; Stupp, S. I., *Chem. Mater.* **2015,** *27*, 1201-1209.

(277) Ruiz-Carretero, A.; Aytun, T.; Bruns, C. J.; Newcomb, C. J.; Tsai, W. W.; Stupp, S. I., *J. Mater. Chem. A* **2013,** *1*, 11674-11681.

(278) Lai, L. F.; Love, J. A.; Sharenko, A.; Coughlin, J. E.; Gupta, V.; Tretiak, S.; Nguyen, T. Q.; Wong, W. Y.; Bazan, G. C., *J. Am. Chem. Soc.* **2014,** *136*, 5591-5594.

(279) Tang, A. L.; Zhan, C. L.; Yao, J. N., *Adv. Energy Mater.* **2015,** *5*, 1500059.

(280) Welch, G. C.; Bakus, R. C.; Teat, S. J.; Bazan, G. C., *J. Am. Chem. Soc.* **2013,** *135*, 2298-2305.

(281) Feng, H. R.; Li, M. M.; Ni, W.; Liu, F.; Wan, X. J.; Kan, B.; Wang, Y. C.; Zhang, Y. M.; Zhang, Q.; Zuo, Y.; Yang, X.; Chen, Y. S., *J. Mater. Chem. A* **2015,** *3*, 16679-16687.

(282) Kumar, C. V.; Cabau, L.; Koukaras, E. N.; Siddiqui, S. A.; Sharma, G. D.; Palomares, E., *Nanoscale* **2015,** *7*, 7692-7703.

(283) Takacs, C. J.; Sun, Y. M.; Welch, G. C.; Perez, L. A.; Liu, X. F.; Wen, W.; Bazan, G. C.; Heeger, A. J., *J. Am. Chem. Soc.* **2012,** *134*, 16597-16606.

(284) Lin, Y. Z.; Li, Y. F.; Zhan, X. W., *Chem. Soc. Rev.* **2012,** *41*, 4245-4272.

(285) Marrocchi, A.; Tomasi, I.; Vaccaro, L., *Isr. J. Chem.* **2012,** *52*, 41-52.

(286) Yu, Q. C.; Fu, W. F.; Wan, J. H.; Wu, X. F.; Shi, M. M.; Chen, H. Z., *ACS Appl. Mater. Inter.* **2014,** *6*, 5798-5809.

(287) Zhang, L.; Cao, Y.; Colella, N. S.; Liang, Y.; Bredas, J. L.; Houk, K. N.; Briseno, A. L., *Acc. Chem. Res.* **2015,** *48*, 500-509.

(288) Zhu, X. W.; Xia, B. Z.; Lu, K.; Li, H.; Zhou, R. M.; Zhang, J. Q.; Zhang, Y. J.; Shuai, Z. G.; Wei, Z. X., *Chem. Mater.* **2016,** *28*, 943-950.

(289) Aytun, T.; Santos, P. J.; Bruns, C. J.; Huang, D.; Koltonow, A. R.; Olvera de la Cruz, M.; Stupp, S. I., *J. Phys. Chem. C* **2016,** *120*, 3602-3611.

(290) Shinamura, S.; Osaka, I.; Miyazaki, E.; Nakao, A.; Yamagishi, M.; Takeya, J.; Takimiya, K., *J. Am. Chem. Soc.* **2011,** *133*, 5024-5035.

(291) Bronstein, H.; Hurhangee, M.; Fregoso, E. C.; Beatrup, D.; Soon, Y. W.; Huang, Z.; Hadipour, A.; Tuladhar, P. S.; Rossbauer, S.; Sohn, E.-H.; Shoaee, S.; Dimitrov, S. D.; Frost, J. M.; Ashraf, R. S.; Kirchartz, T.; Watkins, S. E.; Song, K.; Anthopoulos, T.; Nelson, J.; Rand, B. P.; Durrant, J. R.; McCulloch, I., **2013,** *25*, 4239-4249.

(292) Huo, L.; Huang, Y.; Fan, B.; Guo, X.; Jing, Y.; Zhang, M.; Li, Y.; Hou, J., *Chem. Commun.* **2012,** *48*, 3318-3320.

(293) Liu, J. H.; Walker, B.; Tamayo, A.; Zhang, Y.; Nguyen, T. Q., *Adv. Funct. Mater.* **2013,** *23*, 47-56.

(294) Eisenmenger, N. D.; Su, G. M.; Welch, G. C.; Takacs, C. J.; Bazan, G. C.; Kramer, E. J.; Chabinyc, M. L., *Chem. Mater.* **2013,** *25*, 1688-1698.

(295) Mitsui, C.; Soeda, J.; Miwa, K.; Tsuji, H.; Takeya, J.; Nakamura, E., *J. Am. Chem. Soc.* **2012,** *134*, 5448-5451.

(296) Bunz, U. H. F., *Angew. Chem., Int. Ed.* **2010,** *49*, 5037-5040.

(297) Ni, W.; Li, M. M.; Liu, F.; Wan, X. J.; Feng, H. R.; Kan, B.; Zhang, Q.; Zhang, H. T.; Chen, Y. S., *Chem. Mater.* **2015,** *27*, 6077-6084.

(298) Zhou, N. J.; Vegiraju, S.; Yu, X. G.; Manley, E. F.; Butler, M. R.; Leonardi, M. J.; Guo, P. J.; Zhao, W.; Hu, Y.; Prabakaran, K.; Chang, R. P. H.; Ratner, M. A.; Chen, L. X.; Facchetti, A.; Chen, M. C.; Marks, T. J., *J. Mater. Chem. C* **2015,** *3*, 8932-8941.

(299) Fitzner, R.; Elschner, C.; Weil, M.; Uhrich, C.; Korner, C.; Riede, M.; Leo, K.; Pfeiffer, M.; Reinold, E.; Mena-Osteritz, E.; Bauerle, P., *Adv. Mater.* **2012,** *24*, 675-680.

(300) Kim, C.; Liu, J. H.; Lin, J. S.; Tamayo, A. B.; Walker, B.; Wu, G.; Nguyen, T. Q., *Chem. Mater.* **2012,** *24*, 1699-1709.

(301) Min, J.; Luponosov, Y. N.; Gasparini, N.; Richter, M.; Bakirov, A. V.; Shcherbina, M. A.; Chvalun, S. N.; Grodd, L.; Grigorian, S.; Ameri, T.; Ponomarenko, S. A.; Brabec, C. J., *Adv. Energy Mater.* **2015,** *5*, 1500386.

(302) Tang, A. L.; Zhan, C. L.; Yao, J. N., *Chem. Mater.* **2015,** *27*, 4719-4730.

(303) Zerdan, R. B.; Shewmon, N. T.; Zhu, Y.; Mudrick, J. P.; Chesney, K. J.; Xue, J. G.; Castellano, R. K., *Adv. Funct. Mater.* **2014,** *24*, 5993-6004.

(304) Kline, R. J.; DeLongchamp, D. M.; Fischer, D. A.; Lin, E. K.; Richter, L. J.; Chabinyc, M. L.; Toney, M. F.; Heeney, M.; McCulloch, I., *Macromolecules* **2007,** *40*, 7960-7965.

(305) Fitzner, R.; Mena-Osteritz, E.; Mishra, A.; Schulz, G.; Reinold, E.; Weil, M.; Körner, C.; Ziehlke, H.; Elschner, C.; Leo, K.; Riede, M.; Pfeiffer, M.; Uhrich, C.; Bäuerle, P., *J. Am. Chem. Soc.* **2012,** *134*, 11064-11067.

(306) Mei, J.; Wu, H.-C.; Diao, Y.; Appleton, A.; Wang, H.; Zhou, Y.; Lee, W.-Y.; Kurosawa, T.; Chen, W.-C.; Bao, Z., **2015,** *25*, 3455-3462.

(307) Yang, L. Q.; Zhou, H. X.; You, W., *J. Phys. Chem. C* **2010,** *114*, 16793-16800.

(308) Piliego, C.; Holcombe, T. W.; Douglas, J. D.; Woo, C. H.; Beaujuge, P. M.; Frechet, J. M. J., *J. Am. Chem. Soc.* **2010,** *132*, 7595-7597.

(309) Yiu, A. T.; Beaujuge, P. M.; Lee, O. P.; Woo, C. H.; Toney, M. F.; Fréchet, J. M. J., *J. Am. Chem. Soc.* **2011,** *134*, 2180-2185.

(310) Mcculloch, I.; Heeney, M.; Bailey, C.; Genevicius, K.; I, M.; Shkunov, M.; Sparrowe, D.; Tierney, S.; Wagner, R.; Zhang, W. M.; Chabinyc, M. L.; Kline, R. J.; Mcgehee, M. D.; Toney, M. F., *Nature Mater.* **2006,** *5*, 328-333.

(311) Zhou, N.; Guo, X.; Ortiz, R. P.; Harschneck, T.; Manley, E. F.; Lou, S. J.; Hartnett, P. E.; Yu, X.; Horwitz, N. E.; Burrezo, P. M.; Aldrich, T. J.; López Navarrete, J. T.; Wasielewski, M. R.; Chen, L. X.; Chang, R. P. H.; Facchetti, A.; Marks, T. J., *J. Am. Chem. Soc.* **2015,** *137*, 12565-12579.

(312) Oberhumer, P. M.; Huang, Y. S.; Massip, S.; James, D. T.; Tu, G. L.; Albert-Seifried, S.; Beljonne, D.; Cornil, J.; Kim, J. S.; Huck, W. T. S.; Greenham, N. C.; Hodgkiss, J. M.; Friend, R. H., *J. Chem. Phys.* **2011,** *134*, 114901.

(313) Tang, F. C.; Wu, F. C.; Yen, C. T.; Chang, J.; Chou, W. Y.; Chang, S. H. G.; Cheng, H. L., *Nanoscale* **2015,** *7*, 104-112.

(314) Loser, S.; Bruns, C. J.; Miyauchi, H.; Ortiz, R. P.; Facchetti, A.; Stupp, S. I.; Marks, T. J., *J. Am. Chem. Soc.* **2011,** *133*, 8142-8145.

(315) Loser, S.; Miyauchi, H.; Hennek, J. W.; Smith, J.; Huang, C.; Facchetti, A.; Marks, T. J., *Chem. Commun.* **2012,** *48*, 8511-8513.

(316) Guerrero, A.; Loser, S.; Garcia-Belmonte, G.; Bruns, C. J.; Smith, J.; Miyauchi, H.; Stupp, S. I.; Bisquert, J.; Marks, T. J., *Phys. Chem. Chem. Phys.* **2013,** *15*, 16456-16462.

(317) Tan, W.-Y.; Gao, K.; Zhang, J.; Chen, L.-L.; Wu, S.-P.; Jiang, X.-F.; Peng, X.-B.; Hu, Q.; Liu, F.; Wu, H.-B.; Cao, Y.; Zhu, X.-H., *Solar RLL* **2016**, 1600003.

(318) Tang, A.; Zhan, C.; Yao, J.; Zhou, E., *Adv. Mater.* **2016,** *29*, 1600013.

(319) Min, J.; Cui, C.; Heumueller, T.; Fladischer, S.; Cheng, X.; Spiecker, E.; Li, Y.; Brabec, C. J., *Adv. Energy Mater.* **2016,** *6*, 1600515.

(320) Wolf, J.; Babics, M.; Wang, K.; Saleem, Q.; Liang, R.-Z.; Hansen, M. R.; Beaujuge, P. M., *Chem. Mater.* **2016,** *28*, 2058-2066.

(321) Zhu, X.; Xia, B.; Lu, K.; Li, H.; Zhou, R.; Zhang, J.; Zhang, Y.; Shuai, Z.; Wei, Z., *Chem. Mater.* **2016,** *28*, 943-950.

(322) Li, M.; Ni, W.; Wan, X.; Zhang, Q.; Kan, B.; Chen, Y., *J. Mater. Chem.* **2015,** *3*, 4765-4776.

(323) Marcus, R. A., *Rev. Mod. Phys.* **1993,** *65*, 599-610.

(324) Bredas, J. L.; Beljonne, D.; Coropceanu, V.; Cornil, J., *Chem. Rev.* **2004,** *104*, 4971-5003.

(325) Shao, Y.; Molnar, L. F.; Jung, Y.; Kussmann, J.; Ochsenfeld, C.; Brown, S. T.; Gilbert, A. T. B.; Slipchenko, L. V.; Levchenko, S. V.; O'Neill, D. P.; DiStasio, R. A.; Lochan, R. C.; Wang, T.; Beran, G. J. O.; Besley, N. A.; Herbert, J. M.; Lin, C. Y.; Van Voorhis, T.; Chien, S. H.; Sodt, A.; Steele, R. P.; Rassolov, V. A.; Maslen, P. E.; Korambath, P. P.; Adamson, R. D.; Austin, B.; Baker, J.; Byrd, E. F. C.; Dachsel, H.; Doerksen, R. J.; Dreuw, A.; Dunietz, B. D.; Dutoi, A. D.; Furlani, T. R.; Gwaltney, S. R.; Heyden, A.; Hirata, S.; Hsu, C. P.; Kedziora, G.; Khalliulin, R. Z.; Klunzinger, P.; Lee, A. M.; Lee, M. S.; Liang, W.; Lotan, I.; Nair, N.; Peters, B.; Proynov, E. I.; Pieniazek, P. A.; Rhee, Y. M.; Ritchie, J.; Rosta, E.; Sherrill, C. D.; Simmonett, A. C.; Subotnik, J. E.; Woodcock, H. L.; Zhang, W.; Bell, A. T.; Chakraborty, A. K.; Chipman, D. M.; Keil, F. J.; Warshel, A.; Hehre, W. J.; Schaefer, H. F.; Kong, J.; Krylov, A. I.; Gill, P. M. W.; Head-Gordon, M., *Phys. Chem. Chem. Phys.* **2006,** *8*, 3172-3191.

(326) Halkyard, C. E.; Rampey, M. E.; Kloppenburg, L.; Studer-Martinez, S. L.; Bunz, U. H. F., *Macromolecules* **1998,** *31*, 8655-8659.

(327) Hablot, D.; Retailleau, P.; Ziessel, R., *Chem.-Eur. J.* **2010,** *16*, 13346-13351.

(328) Roncali, J., *Macromol. Rapid Comm.* **2007,** *28*, 1761-1775.

(329) Szarko, J. M.; Guo, J. C.; Liang, Y. Y.; Lee, B.; Rolczynski, B. S.; Strzalka, J.; Xu, T.; Loser, S.; Marks, T. J.; Yu, L. P.; Chen, L. X., *Adv. Mater.* **2010,** *22*, 5468-5472.

(330) Youn, J.; Huang, P.-Y.; Huang, Y.-W.; Chen, M.-C.; Lin, Y.-J.; Huang, H.; Ortiz, R. P.; Stern, C.; Chung, M.-C.; Feng, C.-Y.; Chen, L.-H.; Facchetti, A.; Marks, T. J., *Adv. Funct. Mater.* **2012,** *22*, 48-60.

(331) Barbara, P. F.; Meyer, T. J.; Ratner, M. A., *J .Phys. Chem.* **1996,** *100*, 13148-13168.

(332) Feng, X. L.; Marcon, V.; Pisula, W.; Hansen, M. R.; Kirkpatrick, J.; Grozema, F.; Andrienko, D.; Kremer, K.; Mullen, K., *Nature Mater.* **2009,** *8*, 421-426.

(333) Devos, A.; Lannoo, M., *Phys. Rev. B* **1998,** *58*, 8236-8239.

(334) Vohra, V.; Kawashima, K.; Kakara, T.; Koganezawa, T.; Osaka, I.; Takimiya, K.; Murata, H., *Nat. Photon.* **2015,** *9*, 403-408.

(335) Loser, S.; Miyauchi, H.; Hennek, J. W.; Smith, J.; Huang, C.; Facchetti, A.; Marks, T. J., *Chem. Commun.* **2012,** *48*, 8511-8513.

(336) Arredondo, B.; Romero, B.; Del Pozo, G.; Sessler, M.; Veit, C.; Wurfel, U., *Sol. Energ. Mat. Sol. C* **2014,** *128*, 351-356.

(337) Credgington, D.; Jamieson, F. C.; Walker, B.; Nguyen, T. Q.; Durrant, J. R., *Adv. Mater.* **2012,** *24*, 2135-2141.

(338) Ray, B.; Baradwaj, A. G.; Khan, M. R.; Boudouris, B. W.; Alam, M. A., *Proc. Natl. Acad. Sci. USA* **2015,** *112*, 11193-11198.

(339) Osaka, I.; Abe, T.; Shinamura, S.; Takimiya, K., *J. Am. Chem. Soc.* **2011,** *133*, 6852-6860.

(340) Graham, K. R.; Erwin, P.; Nordlund, D.; Vandewal, K.; Li, R. P.; Ndjawa, G. O. N.; Hoke, E. T.; Salleo, A.; Thompson, M. E.; McGehee, M. D.; Amassian, A., *Adv. Mater.* **2013,** *25*, 6076-6082.

(341) Roncali, J., *Acc. Chem. Res.* **2009,** *42*, 1719.

(342) Liu, Y. S.; Wan, X. J.; Wang, F.; Zhou, J. Y.; Long, G. K.; Tian, J. G.; You, J. B.; Yang, Y.; Chen, Y. S., *Adv. Energy Mater.* **2011,** *1*, 771-775.

(343) Risko, C.; Bredas, J. L., *Top. Curr. Chem.* **2014,** *352*, 1-38.

(344) Leong, W. L.; Welch, G. C.; Seifter, J.; Seo, J. H.; Bazan, G. C.; Heeger, A. J., *Adv. Energy Mater.* **2013,** *3*, 356-363.

(345) Mihailetchi, V. D.; Wildeman, J.; Blom, P. W. M., *Phys. Rev. Lett.* **2005,** *94*, 126602.

(346) Mihailetchi, V. D.; Xie, H. X.; de Boer, B.; Koster, L. J. A.; Blom, P. W. M., *Adv. Funct. Mater.* **2006,** *16*, 699-708.

(347) Proctor, C. M.; Love, J. A.; Nguyen, T. Q., *Adv. Mater.* **2014,** *26*, 5957.